MULTISCALE MATERIAL MODELING OF ADDITIVELY MANUFACTURED COMPOSITE LAMINATES

MADHUKAR SOMIREDDY

A DISSERTATION SUBMITTED TO THE FACULTY OF
GRADUATE STUDIES IN PARTIAL FULFILLMENT OF THE
REQUIREMENTS FOR THE DEGREE OF
DOCTOR OF PHILOSOPHY

GRADUATE PROGRAM IN MECHANICAL ENGINEERING
YORK UNIVERSITY
TORONTO, ONTARIO

July 2019

ABSTRACT

Additive manufacturing (AM) technology has revolutionized the production of structural parts for many industries. AM methods enable freedom in design of a part and furthermore, make it easier to fabricate a part with tailored microstructure to yield desired mechanical properties. Despite many other benefits, anisotropy in the material properties of 3D printed parts remains of primary concern. Anisotropy is introduced into parts during the printing process. This calls for the need to investigate the material behaviour of printed parts at different scales to enable the effective design and analysis of models for 3D printing. The present work therefore focuses on addressing the material behaviour of 3D printed parts via fused filament fabrication (FFF), a material extrusion AM process. Four aspects of the problem are accordingly examined. First, the material behaviour of printed parts with different materials is assessed by conducting mechanical testing. Second, the mechanical behaviour of printed parts is characterized using laminate mechanics. Furthermore, the microstructure of printed parts is characterized, and its influence on the final properties is investigated. Third, computational micromechanical models are employed to estimate the final material properties of printed parts based on the underlying mesostructure. Finally, the computational models are employed to perform damage analysis of printed parts.

The research work revealed that the final material behavior of printed parts was governed by their mesostructure, which was produced during 3D printing process. The behavior of printed parts resembled that of traditional laminates and therefore, the laminate mechanics can be employed in preliminary design and analysis. Computational models predicted accurate final properties of parts by considering their mesostructure, and also their nonlinear behavior under loads. The computational damage model that employed bulk material properties provided ideal material behavior and the other damage model that used results of unidirectional laminates provided actual material behavior of printed parts. In summary, this work presents a process–structure–property relationship for 3D printed parts, and also outlines the mechanics of the material to characterize the mechanical behaviour of the printed parts. Finally, computational models are developed for the effective design and analysis of models for 3D printing.

ACKNOWLEDGEMENTS

I would like to thank my supervisor Dr. Aleksander Czekanski for everything throughout the course of my research. I wish to acknowledge my thesis supervisory committee members, Dr. Zheng Hong (George) Zhu and Dr. Roger Kempers, for their constructive feedback on the present work. A special thank you to the examiners, Dr. Mohamed Elbestawi, of McMaster University, and Dr. Rashid Bashir, of York University for their time and feedback on the research. Together, their feedback helped improve the quality of work in various aspects. I also wish to convey a special thanks to Dr. C.V. Singh, from University of Toronto for his technical advice and moral support during the course of my research.

I am grateful to my family and friends for their moral support, patience, and confidence in me throughout the process of my PhD work and research. A special thanks to all members of IDEA-Lab at York University from September 2015- June 2019 for their support, constant feedback and comradery during the course of present work.

Finally, I would like to thank Lassonde School of Engineering and the Natural Sciences and Engineering Research Council (NSERC) for providing financial support.

TABLE OF CONTENTS

LIST OF TABLES

LIST OF FIGURES

NOMENCLATURE

Symbols	**Description**
L	Length of specimen
W	Width of specimen
T	Thickness of specimen
TL	Tab length
l	Span length of specimen
$\theta°$	Printing direction (fiber angle, raster angle)
t	Thickness(t_1 or t_2) of layers (laminae) of printed parts
a_0	Initial crack length
a	Delamination length
δ	Crack opening displacement
P	Load
G_I	Fracture toughness
E_i	Young's modulus of lamina in direction i (for i = 1 to 3)
G_{ij}	Shear modulus of lamina in a plane i-j (for i, j = 1 to 3)
v_{ij}	Poisson's ratio of lamina
X_t	Longitudinal strength of lamina in tension
Y_t	Transverse strength of lamina in tension
S	Inplane shear strength of lamina
E_x	Young's modulus of laminate in direction x
U_t	Ultimate tensile strength of laminate
ε_t	Strain to failure of laminate
σ_ply	Principal stress of lamina
ε_ply	Elastic strain of lamina
E^f_x	Flexural stiffness of laminate in direction x
U^f_x	Flexural strength of laminate in direction x
P_ult	Ultimate load
A	Cross sectional area
$\boldsymbol{C}$	Constitutive matrix of material

$\boldsymbol{S}$	Compliance matrix of material
C_{ij}	Elements of constitutive matrix
S_{ij}	Elements of compliance matrix
$\boldsymbol{Q}$	Reduced stiffness matrix for lamina
$\boldsymbol{A}$, $\boldsymbol{B}$, $\boldsymbol{D}$	Stiffness matrices of lamina
u, v, w	Displacements in x, y and z, respectively

LIST OF ACRONYMS

2D	Two dimensional
3D	Three dimensional
ABS	Acrylonitrile butadiene styrene
AM	Additive manufacturing
ASTM	American society for testing and materials
CAD	Computer aided design
CAE	Computer aided engineering
CF	Carbon fiber
CLT	Classical laminate theory
CT	Computed tomography
DIC	Digital image correlation
DM-Bulk	Damage modeling with properties of bulk material
DM-UDL	Damage modeling with properties of unidirectional laminates
FE	Finite element
FFF	Fused filament fabrication
RVE	Representative volume element
SCF	Short carbon fiber
.STL	Stereolithography format

Chapter 1 Introduction and Justification

1.1 Additive manufacturing

Additive manufacturing (AM) is a fabrication process used to build three-dimensional (3D) parts through the layer-by-layer deposition of material. AM technologies, commonly referred to as 3D printing, can manufacture a complex 3D part through a 3D computer-aided design (CAD) model that instructs the 3D printing machine how to "print," or deposit, a given material. AM technologies can be broadly categorized as follows [ASTM F2792]: binder jetting, directed energy deposition, material extrusion, material jetting, powder bed fusion, sheet lamination, and vat photopolymerization. These advanced fabrication techniques manufacture parts in the same way, but the differences between them lie in the source of heat (laser, thermal, electron beam, plasma arc), the manner of dispensing material (build chamber characteristics), the number of printing axes, and the state of the material (liquid, powder, or filament wire) [1].

The fabrication process used in AM technologies is contrary to conventional machining processes, whereby material is cut away — or subtracted — to obtain the final product. The primary advantage of AM technology is the ability to make 3D parts with complex geometry in less time and with less effort than that required in conventional machining processes. Other benefits of AM technology include rapid prototyping, minimal or no material wastage, no extra tooling, efficient design of materials, and the capability of tailoring functionally graded materials. Furthermore, emerging AM technologies make it far easier to design a material to tailor the properties of the final 3D printed part. These processes allow the design of the microstructure of a material to yield a part with the desired mechanical properties. Design of the microstructure, and hence formation of the fabricated part, is achieved through systematic deposition of a material layer upon layer.

The many benefits of AM technologies have led to its increasing popularity in recent years [2], especially in the fields of mechanical, aerospace, and biomedical engineering [3]. AM processes will be responsible for nothing short of a major transformation in how materials and components are designed and fabricated in the near future. However, despite the considerable benefits of fabricating components using AM technologies, several challenges remain. For one, the material properties of the final 3D printed part differ from those of the initial material [4]. As a result, anisotropy is introduced as a factor influencing the properties of the final 3D printed part. Furthermore, AM is a material-dependent process, meaning that a particular AM technique can only use certain materials. For instance, vat photopolymerization (i.e., stereolithography) can only produce 3D parts using photopolymers. Limited build volume is another concern, meaning that 3D printers can print small parts only. Other fundamental challenges associated with 3D printing are the limits on production size, quality of the prints, accuracy of the printers, and the high cost of the materials and the printers [5].

More recently, in response to some the aforementioned challenges, a material extrusion AM process known as fused filament fabrication (FFF) has risen in popularity. 3D printed parts using FFF are less expensive and possess greater durability and robustness. This has led to FFF 3D printers and the materials they use are gaining a greater share of the market than any other AM process. The increasingly widespread use of FFF in the 3D printing of functional parts for industrial applications requires that special attention be paid to enhancing the reliability of these parts. Therefore, parts printed via the FFF process are considered in this work for investigating theirs structure–property relationship. Furthermore, the use of polymer composite materials to

3D printed parts for industry has increased dramatically because of the many benefits associated with composite materials. Therefore, the development as well as the printing of composite materials via FFF is an emergent research trend in this field [6–10]. Additionally, the FFF process enables the fabrication of sandwich core shapes with different infill patterns, enabling the user to design different infill patterns to obtain printed parts with the desired properties [11]. In addition, different 3D preforms for composites can be designed by varying the parameters of the printing process to obtain the desired mechanical properties [12]. Next-generation functional composite parts also can be fabricated using this printing method [13]. Further details of the printing process and the behavior of printed parts with this method are discussed in the following section.

1.2 Fused Filament Fabrication

FFF is a material extrusion AM process for printing 3D parts. In this process, a plastic filament is melted in a liquefier, and molten material is then extruded through a nozzle (Figure 1.1). Systematic movement of the nozzle deposits the molten material on the build platform (i.e., bed) layer by layer, leading the material to solidify and diffuse with the previously deposited material. The molten material deposited by the nozzle solidifies on the bed, which resembles a fiber and is also referred to as a "road."

The mechanical properties of printed parts are governed by their mesostructure, which is created during the fabrication of the part. The parameters of the printing process, namely layer thickness (t), deposition orientation (raster angle: θ°), and gap between adjacent fibers, are the main factors influencing the mechanical properties of the fabricated part. The standard printing practice for producing solid volume parts is shown in Figure 1.1b; such printed parts resemble laminate structures.

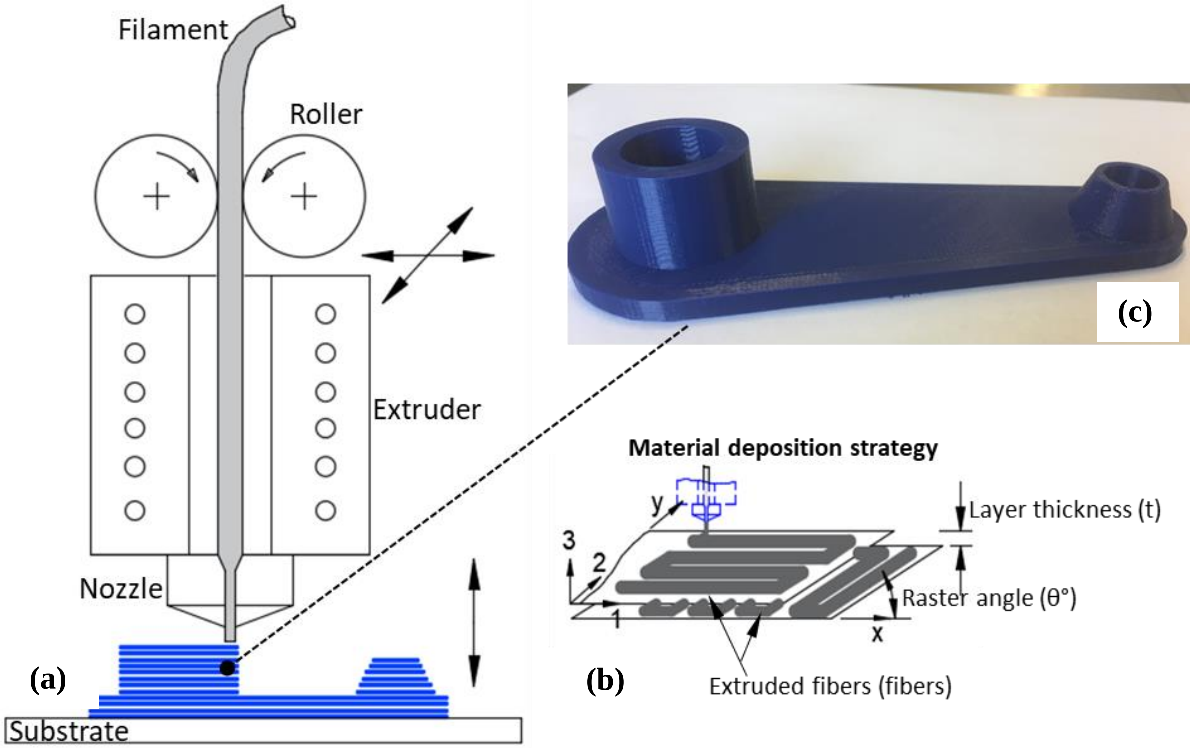

Figure 1.1. 3D printing of a part via fused filament fabrication (FFF): (a) FFF process, (b) material deposition strategy, and (c) 3D printed part.

FFF process can also accommodate the composite materials for fabricating composite parts. Traditionally, parts with composite materials have been fabricated either via injection moulding or vacuum bag molding. Injection molding can process short fibers or chopped reinforced polymeric materials for producing composite parts, while vacuum bag molding is mainly used for producing laminated composite parts with continuous fibers. Reinforcements orient randomly in the composite parts produced via injection molding, resulting in unpredictable anisotropic material behaviour. On the other hand, the composite laminate parts produced via vacuum bag molding require manual skill to lay up the laminae. Further, it is difficult to fabricate the intricate features of parts using laminae. A recent study [14] on different fabrication methods for composite parts concluded that AM technology is the most flexible method for fabricating composite parts. The AM process is superior because it requires no tooling or special skills, production is rapid, and the design of parts is efficient, with no limitations on the geometric complexity of the final printed part.

Now let us consider how parts are fabricated via FFF. The layers of the printed parts created via FFF contain not only extruded thermoplastic material — which consists of continuous thermoplastic fibers — but also other reinforcements such as carbon fibers (short or continuous fiber) embedded in the extruded thermoplastic fibers. Hence, a printed part made of polymer composite filament behaves like a laminated composite part. In the remainder of this thesis, the continuous extruded thermoplastic fibers of the printed parts are referred to as “extruded fibers” or simply “fibers,” and any other reinforcement material (short or continuous carbon fiber) is referred to as “reinforcements.” Occasionally, the 3D printed parts are also referred to as “printed laminates.”

The behaviour of the composite laminate is the result of the orientation of the extruded fibers; the extruded fibers also have other reinforcements. The orientation of reinforcements, such as short carbon fibers, in the extruded fibers aligns with the printing direction of the layers of the part [15–17]. The printing technique basically combines two traditional fabrication methods for composite parts: injection molding and the vacuum bag method for laminates. The fabrication process for the three methods is shown in Figure 1.2. The layer-by-layer fabrication of a part via FFF and the orientation of the extruded composite fibers of the layers of the part are shown in Figure 1.2c. The layers of the printed part are each only one fiber thick, whereas traditional laminae consist of more than one continuous reinforcement across their thickness. Furthermore, the orientation of the reinforcements in the printed composite laminate part is known and aligned with the fiber direction of the layers of the part, which is not the case for injection-molded composite parts. The orientation of the reinforcements influences the mechanical behaviour of the printed parts and must be considered while estimating the material properties of the printed parts. By combining two traditional fabrication methods, the FFF process confers composite laminate mechanical behaviour to printed parts made of composite material.

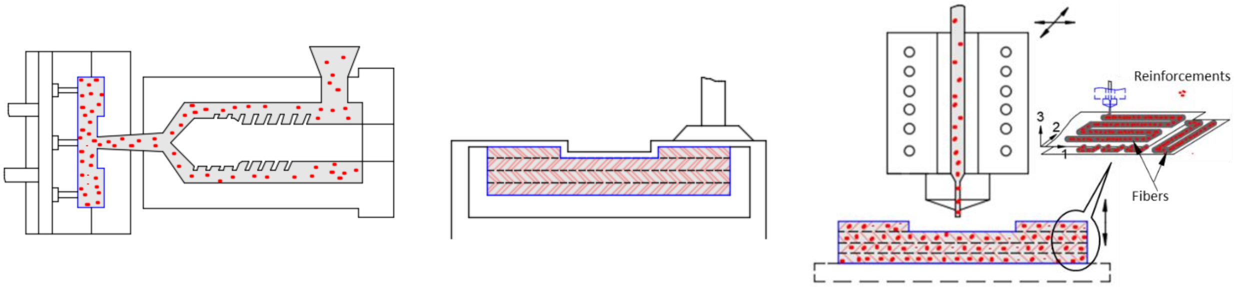

(a) **(b)** **(c)**

Figure 1.2. Fabrication of a composite part via (a) injection molding, (b) vacuum bag molding, and (c) fused filament fabrication.

1.3 Technological Gap and Justification of the Study

An important concern related to the FFF process is the variation in the material properties of the printed parts. Specifically, the material properties of the final printed part differ from those of the material used in the manufacturing of the part [18]. As a result, anisotropy is introduced during the deposition of the material. Anisotropy arises because of a change in the mesostructure of the part while it is being printed. Moreover, there is limited understanding of the process–structure–property relationship. This knowledge gap calls for the material behaviour of the final printed parts to be investigated at different scales — from the meso to the macro level. Therefore, characterization of the material behaviour of the printed parts needs further exploration. Additionally, this thesis characterizes the fundamental mechanical behaviour of the printed parts when they are subjected to mechanical loads. Finally, computational models are developed to enable the effective design and analysis of parts for 3D printing.

1.4 Research Objectives

The overall goal of this thesis is to characterize the mechanical behaviour of 3D printed parts via FFF as well as to develop computational models that can be used to analyze the 3D printed parts. The specific objectives are as follows:

i. Investigate the material behaviour of 3D printed parts.

   Material behaviour of 3D printed parts can be investigated by conducting mechanical testing. Two different materials, isotropic and composite, are used for printing the test coupons. Furthermore, printed coupons with different layer thicknesses and raster angles are used during mechanical testing.

ii. Characterize the mechanical behaviour of 3D printed parts.

   Constitutive material behaviour of 3D printed parts can be estimated from experimental results using laminate mechanics. Laminate theory is then employed to characterize the mechanical behaviour of the printed parts. Also, laminate failure criterion is used for failure analysis of the printed parts.

iii. Characterize the mesostructure of 3D printed parts and its influence on the final properties.

   3D parts printed with isotropic material as well as composite material are considered in order to quantifying mesostructural features. An optical microscope is used to quantify the mesostructural features of 3D parts printed with isotropic material; the features assessed include the size and shape of the extruded fibers. 3D parts printed with composite material are evaluated in a morphology study using a micro-CT scanner. Microstructural features such as volume percentage of reinforcements and size and shape of reinforcements are quantified in addition to size and shape of the extruded fibers.

iv. Develop computational models for linear material modeling of 3D printed parts.

Computational models can be developed to mitigate the problems associated with experimental work. The numerical homogenization technique is employed in linear material modeling. To develop this numerical model, a representative volume of material from the mesostructure of the 3D printed parts is considered.

v. Develop computational models for damage modeling of 3D printed parts.

Computational models can be extended to perform damage analysis of 3D printed parts. Continuum damage mechanics are employed in damage modeling of the material of the 3D printed parts.

1.5 Layout of the Thesis

The thesis consists of eight chapters. **Chapter 1** introduces the topic and the main objectives of the thesis. **Chapter 2** presents a detailed literature review of different aspects of 3D printed parts. Next, **chapter 3** discusses the material behaviour of the printed parts based on the results of mechanical testing on printed test coupons. In **chapter 4**, the mechanical behaviour of 3D printed parts is characterized using laminate mechanics. **Chapter 5** presents the microstructure of 3D parts made of composite materials and characterized using a micro-CT scanner. Then, **chapter 6** addresses the computational model for linear material modeling of 3D printed parts, followed by a discussion in **chapter 7** of computational models for damage modeling of 3D printed parts. Finally, **chapter 8** presents a summary of this work. **Appendix A** contains a detailed list of the computational models used to investigate the influence of build orientation on the material behaviour of 3D printed parts.

Chapter 2 Literature Review

Fused filament fabrication (FFF), an AM material extrusion method, is evolving rapidly in terms of process, applications, and materials [19–21]. A major focus of the FFF technique is printing next-generation multifunctional parts using responsive materials [22]. Such materials have broad industrial application and have been used in electronic devices [23], biomedical devices [24], biomaterials [25], and biomimetic structures [26]. Sensor parts used for monitoring structural health can also be fabricated via FFF [27–29]. Furthermore, the FFF process allows the tailoring of a material's microstructure. In recent studies [6,12], this printing method was used to develop composite materials with different multidirectional preforms. AM techniques can be used to develop and fabricate biological composites [30–32] as well as to design and fabricate biomaterial for prostheses [33,34].

The AM material extrusion method has thus far been limited to using only thermoplastics in manufacturing 3D printed parts because of the lower melting temperature; however, the properties of thermoplastics are inferior compared with those of metals. Consequently, a new extrusion AM process [35] was recently developed for printing metal parts. However, the FFF process can only accommodate the fabrication of smaller parts, meaning that the build volume is limited. 3D printing of larger structural parts [36] — through the deposition of larger beads — results in the formation of voids and improper fusion between the layers of the printed parts. Researchers have investigated the fabrication of polymer composite parts via AM techniques and the resulting issues in the 3D printed parts, such as homogeneity of the material, porosity, fiber alignment, and interlayer bonding [37]. It was found that modeling and simulation work for predicting the performance of the printed composite parts is limited, and further exploration in that direction is needed. The following literature review emphasizes four aspects of 3D printed parts: the influence of process parameters on the final mechanical properties of the printed parts; the materials used for 3D printing and their effect on the final mechanical properties of 3D printed part; the characterization of the material behaviour of 3D printed parts; and finally, the material failure behaviour of 3D printed parts.

2.1 Influence of printing parameters on the performance of 3D printed parts

The quality of 3D printed parts depends on the process parameters used for printing [38]. The right printing strategy and optimal process parameters improve the mechanical properties of the final part. In addition, the filling strategy influences the mechanical behaviour of the parts. Researchers [39–51] have investigated the effect of various process parameters, such as raster angle, layer thickness, infill pattern and density, printing speed, air gap, and temperature, on the mechanical properties of the final fabricated part. It was revealed that the properties of the parts are significantly influenced by raster angle and layer thickness. Furthermore, several recent studies have examined the dependence of the mechanical properties of printed parts on raster angle for different load cases [52–55]. The aforementioned studies were limited to tensile testing of 3D printed parts. Fracture mechanical tests [56] revealed that the final properties are influenced by bonding strength between adjacent roads as well as between adjacent layers. Bond formation among the roads is driven by the thermal energy of the extruded material [57,58]. Bonding between the layers as well as between adjacent fibers governs the performance of the printed part [59], and the strength of bonding can also be affected by process parameters [60]. However, interlaminar bonding strength can be improved by thermal annealing [61]. Surface quality of the printed parts can be improved by vapor smoothing [62]. The strength and stiffness of printed parts can also be improved by using an optimization algorithm to select the optimal process parameters [63]. These experimental works reveal that the mechanical behaviour of 3D printed parts is anisotropic and governed by process parameters.

Experimental studies reveal that build orientation and raster angle have a significant impact on the properties of 3D printed parts [64,65]. Parts can be 3D printed in any orientation, and users choose the build orientation of a model for printing while generating the G-code. Investigations [66–68] on the influence of building strategy on the quality of printed parts have revealed that it has a pronounced effect on the properties and ultimately performance of printed parts. Orthotropic material behaviour was assessed by conducting experiments on parts that were built in different orientations [69,70]. Build time for printing and surface quality also depend on the build orientation of the parts [71,72]. In summary, variation in build strategy of a model affects the mechanical behaviour of a printed part, resulting in the part having an anisotropic nature. Computational studies [73–75] of the material behaviour of printed parts are limited and thus further exploration using multiscale models is required.

Mesostructure plays an important role in determining the mechanical behaviour of a part. 3D printing a part via layer-by-layer deposition of material creates a new mesostructure in 3D printed parts [76]. The mesostructure of parts printed via FFF is in turn governed by process parameters such as raster angle, layer thickness, air gap between the adjacent roads, and infill pattern and density. The presence of voids in the mesostructure of the part negatively affect the mechanical properties of the part [77]. The properties of the part can be improved by minimizing the presence of these voids and improving the quality of bonding between the fibers. The presence of voids in the printed parts can also be minimized by adding thermally expandable microspheres into the base material used to fabricate the parts [78]. Experimental investigations [79] of the influence of mesostructure on the mechanical properties of printed parts has revealed that the overlap between the adjacent roads provides better mechanical properties by improving bonding strength between the roads and minimizing void density. Microstructural features, such as void shape, void density, shape and size of the fiber, and bonding between the fibers, are also governed by process parameters. In turn, these process parameters govern the properties and thus the mechanical behaviour of printed parts. These experimental observations confirm that, even though the virgin material is isotropic, printed parts fabricated via FFF develop anisotropic behaviour in their mechanical properties, mainly due to the process parameters selected [80].

Extensive efforts have been made to understand the relationship between process parameters and the mechanical properties of printed parts. Anisotropy in the mechanical behaviour of printed parts is due to alteration in the mesostructure of the parts by the process parameters as well as the choice of building strategy. Building strategies are also able to improve the mechanical properties of printed parts. Estimation of the final properties of a material is important to ensure effective analysis of printed parts. Experimental work has sought to determine the elastic moduli of the material of the printed part [39,69], but such work is tedious and time consuming. An alternative approach to determining the elastic moduli of printed parts is by employing computational or analytical methods. The numerical homogenization method and strength of material approach to finding the elastic moduli of a material have been discussed in [81]. A novel approach to finding the elastic moduli of printed parts by considering the mesostructure for homogenization at a macro scale using Green's function was discussed in [82]. Material behaviour of printed cellular structures can be investigated using representative volume element models [83].

2.2 Materials for 3D printing

The materials used in the fabrication of 3D printed parts influence the final properties of the parts. AM techniques can only process certain types of materials; the materials available for AM and their applications are addressed in [84–86]. Thermoplastics are the filament materials commonly used for printing parts via FFF, and the different applications of these materials and printing process are discussed in [87,88]. The material properties of printed parts can be improved by employing composite filament materials during fabrication. Composite filaments are made of thermoplastic material containing other particulates such as carbon fiber and metal. Composite materials for 3D printing have already been developed by researchers [89–95] and are widely used in industry. Furthermore, such composite materials provide better thermal, mechanical, and electrical properties [96–101] compared with parts made using pure thermoplastics. 3D printed parts made of polymeric material reinforced with continuous fibers exhibit better material properties [102–106]. Composite materials are already used to fabricate 3D printed parts, and comprehensive work on the fabrication of composite parts and the composite materials available for printing have been reviewed [7–9]. The importance of carbon fiber reinforcements in the materials for improving the properties of 3D printed parts has been addressed in [107]. Furthermore, the properties of parts can be tailored by altering the mesostructure (developing cellular structures) while the parts are being printed [108–110]. Unlike conventional techniques used to fabricate laminates, FFF can deposit continuous fibers in the desired direction according to numerical analysis of the 3D model output, allowing the final printed part to adequately withstand applied loads [111,112].

Another factor governing the material behaviour of the final printed parts is the type of reinforcements used in the composite material [113]. The reinforcements can be continuous fibers, short fibers, or particulates. Parts printed with continuous fibers have better mechanical properties [103–105] than parts with no additional reinforcements. Design considerations for improving the properties of 3D printed parts using continuous fibers are discussed in [114]. Investigations [115] on the performance of the interface between the continuous fibres and the matrix of printed parts reveals that layer thickness affects bonding strength. Parts printed with short carbon fiber reinforcements have better material properties compared with parts printed using only polymeric material [116–119]. In addition, the reinforcements in the polymeric material minimize shrinkage issues in the printed parts. Post-heat treatment of the printed composite parts can further improve their mechanical properties [120]. Bonding between fiber reinforcements and the matrix of the printed parts influences the final properties; the strength of bonding can be improved by inducing heat to the parts [121,122]. The orientation of reinforcements in the printed parts governs the properties of the final part, and their orientation aligns with the printing direction [123]. The composite materials used to fabricate printed parts also tends to promote anisotropic behaviour [124–126].

2.3 Material behaviour of printed parts

The material behaviour of 3D printed parts resembles that of laminate structures [127–129]. Such behaviour is mainly due to the orientation of fibers and the deposition of layers as the part is printed. The material behaviour of printed parts can be characterized using laminate mechanics and classical laminate theories. Thus, laminate theory is useful in the behavioural characterization of printed parts subjected to different loads during stress analysis. The layers of a printed part behave like an orthotropic material even though the initial filament material is isotropic, and these layers can therefore be treated as a unidirectional fiber-reinforced lamina. This means that the roads in a layer act as fibers in a lamina, and several layers together with the different printing direction behave like laminated composite structures. Therefore, printed parts can be considered laminated composites for the purpose of characterizing their mechanical behaviour.

Laminate mechanics can be employed to characterize the mechanical behaviour of parts printed with only thermoplastic filament material and no additional reinforcements [127–130]. Kulkarni and Dutta [128] were the first to apply classical laminate theory for the analysis of printed parts. Ahn et al. [131] employed analytical models of classical laminate theory, and Tsai-Wu used the failure criterion for laminates to investigate the failure of printed parts. Li et al. [129] presented a theory based on void density to calculate elastic moduli of a layer. The results were validated experimentally, and the mechanical behaviour of the parts was also characterized using laminate theory. Researchers[132,133] employed analytical and numerical methods for estimating the final properties of printed parts. The elastic moduli for the layers (orthotropic material) of printed part were determined experimentally by Casavola et al. [130], and classical laminate theory was then employed to characterize the mechanical behaviour of the printed parts. Alaimo et al. [134] studied the influence of extruded fiber size and material composition of a filament on the mechanical properties of parts fabricated via fused deposition modelling. Mechanical behaviour characterization of printed parts was also conducted by adopting classical laminate theory and using the Tsai–Hill yield criterion.

As is the case for printed parts made without reinforcements, laminate mechanics can be used to characterize the mechanical behaviour of parts that do contain continuous fiber reinforcements [102–105,135,136]. The layers of parts printed with short carbon fibers can be treated as orthotropic lamina material, and the mechanical behaviour of such parts has been successfully characterized using laminate mechanics [137]. To date, researchers have carried out experimental characterization of composite parts printed with material containing continuous fiber [102–105,135,136] and discontinuous fiber [113,116,117,120,123,137] reinforcements, but material modeling has not yet been attempted. Limited literature exists on the use of laminate mechanics and laminate theories to characterize the mechanical behaviour of printed composite parts.

The material behaviour of printed part depends on fiber orientation in the layers, stacking sequence of layers, and build orientation [124,138]. The effects of fiber orientation and stacking sequence of layers in a 3D printed part can be considered in laminate modeling. However, the effect of build orientation on a part's material behaviour cannot be accounted for using laminate theory, and therefore the influence of built orientation on the material properties of printed parts needs further exploration. So far, most of the aforementioned studies involve experimental work, as there has been relatively little work on numerical modeling to determine the elastic moduli of 3D printed parts.

Previous work to determine the constitutive matrix of the material of 3D printed parts has been entirely experimental. Another limitation is that the shape of voids in the mesostructure of printed parts has not been considered. Moreover, the work available only considers the calculation of elastic moduli for a constitutive matrix in the plane stress case. The effect of build orientation on the calculation of the stiffness matrix and the characterization of the mechanical behaviour of 3D printed parts using laminate theory was also not considered. From previous studies, it is evident that build orientation influences the material properties of printed parts. Therefore, variation in material behaviour owing to build orientation should be considered when using laminate theory to characterize the mechanical behaviour of printed parts. A related, unexplored research area is computation of the stiffness matrix of the material of a printed part using numerical multiscale models to account for the impact of different build orientations.

2.4 Failure behaviour of printed parts

The failure behaviour of 3D printed parts is not consistently exhibited because of the presence of anisotropy in the properties of the materials. Moreover, no single failure phenomenon is responsible for the ultimate failure of the part [139]. The failure behaviour of parts printed with reinforced materials is complex and depends on the reinforcements used [140]. The complex failure behaviour and anisotropic properties of the final printed material complicate the design of parts for 3D printing. Therefore, understanding the final material properties of the printed parts and their failure phenomena will allow for effective design and analysis of parts for 3D printing.

The failure phenomenon of printed parts is complex and due to the anisotropic behaviour of the material used for fabrication. Studies of the performance of printed parts that are subjected to mechanical loads reveal that deposition strategy influences the mesostructure of the final parts [138,141,142], and this in turn affects the fatigue life of the parts. The performance of printed parts and analysis of their damage under fatigue loads has been investigated. Failure analysis of printed parts by Rankouhi et al. [143] has shown that printed parts consisting of thin layers are stronger than parts made with thick layers. The authors also found that raster angle has a significant effect on the properties of printed parts. Failure behaviour of printed parts is influenced by their build orientation [144,145]. The orientation of extruded fibers with respect to the loading axis determines the failure behaviour. Fracture development and mechanical behaviour of the printed composite laminates is addressed in [146]. The presence of carbon fiber reinforcements in a polymer filament affects the mechanical failure behaviour of printed parts [147]. Damage evolution of multidirectional 3D printed preforms subjected to compressive loads was assessed in [148] to characterize the microstructure of the parts. Progressive damage modeling of printed parts is presented in [131,134]. Further exploration of the various mesostructural aspects of printed parts made of different materials is needed to characterize their mechanical behaviour.

Chapter 3 Investigation of Mechanical Behaviour of 3D Printed Parts: Mechanical Testing

Summary: A comprehensive understanding of the process–structure–property relationship of 3D printed parts is currently limited. In this work, parts synthesized via fused filament fabrication (FFF) using two different materials, ABS plastic and ABS with reinforced short carbon fibers (SCF), are subjected to mechanical testing. Test coupons of thick- and thin-layered unidirectional laminates as well as bidirectional laminates are printed for tensile and bending tests. The printed parts are treated as printed laminates. Anisotropy in the material properties of the 3D printed parts is investigated. Specifically, anisotropic behaviour is characterized by performing mechanical testing on the 3D printed parts. Finally, the influence of mesostructure on the overall mechanical behaviour of the parts is investigated, and the effect of printing process parameters on the mechanical properties of the parts is explored.

3.1 Introduction

The mechanical behaviour of the printed parts depends on the loads as well as on the type of material used to fabricate the parts. The behaviour of a material is dependent on its properties, and the properties are governed by its mesostructure. The mesostructure of a part is produced while the part is 3D printed and is governed by the printing process parameters. Therefore, to characterize the behaviour of the printed parts, it is important to account for the materials, the underlying mesostructure, and the loads that are applied. Understanding the influence of these factors on the final behaviour of the 3D printed parts allows for effective design and analysis of models for 3D printing.

Printing process parameters influence the mechanical properties of 3D printed parts [38,44,46,99,143,149]. Further, the build orientation of the parts affects their mechanical behaviour [66,67,80,150]. The influence of such parameters results in anisotropy in the printed part. The bonding between the layers as well as adjacent fibers governs the performance of the part [59,151]. The printed composite parts [137,146] have a complex failure phenomenon, and the presence of short carbon fiber (SCF) reinforcements in a polymer affects the mechanical failure behaviour of the printed parts [147]. Investigation of the failure behaviour of unidirectionally printed parts [127] confirms the presence of direction-dependent fracture behaviour. However, the aforementioned works focus only on the overall mechanical behaviour of the printed parts as well as the influence of printing parameters on the parts. Furthermore, the printed parts are not treated as laminate structures in most earlier work. A detailed study to understand the relationship between the printing process and the printed parts as well as emergent properties has not yet ben explored. Therefore, further exploration of various mesostructural aspects of the printed parts is needed to accurately characterize their mechanical behaviour.

The mesostructure of the printed laminates is mainly defined by the materials used for printing, the size of the fibers, the thickness of the layers, and the orientation of the fibers. These elements determine the mesostructure of the printed part and in turn govern the mechanical properties of the part. Therefore, a detailed investigation of different aspects of the mesostructure of a printed part can help to characterize its mechanical behaviour. Test results reveal the mechanical properties of the printed laminates and the behaviour of the laminates under tensile and flexural loads. Furthermore, test results are useful for studying the influence of mesostructure on mechanical properties, which in turn are governed by the printing process.

The mechanical properties of a lamina can be calculated from the tensile test results; this topic is discussed in the following chapter. The flexural properties as well as the behaviour of the printed laminates can be determined from the results of the flexural tests.

In this chapter, experimental test coupons were 3D printed with either an isotropic polymer (ABS) or a composite polymer (ABS+SCF). The test coupons were considered for tensile tests, bending tests and interlaminar fracture toughness tests. Parts with different raster orientations and two different layer thicknesses were printed to investigate the resulting mechanical behaviour of the parts. The printed parts were treated as printed laminates. The mechanical behaviour of the printed test coupons under uniaxial tensile and bending loads was examined. The influence of printing direction in each layer, i.e., the effect of lamina layup on the mechanical behaviour of the printed laminates subjected to loads was investigated. Furthermore, interlaminar fracture strength of the printed laminates was investigated under crack opening mode (Mode-I). Also, factography analysis was carried out to understand the failure behaviour of the parts; a digital image correlation setup was used to conduct this failure analysis. Finally, the influence of the composite material on the mechanical behaviour of the printed parts was studied.

3.2 Methodology

3.2.1 Materials used in test coupons

Two different commercially available filament materials were used to fabricate the 3D printed parts (purchased from 3DXTech, Byron Center, Michigan, USA). Parts printed using isotropic thermoplastic material (ABS) are termed printed laminates with isotropic material, or simply isotropic laminates. Parts consisting of SCF-reinforced thermoplastic material (ABS-SCF) are termed printed laminates with composite material, or simply composite laminates.

Stiffness of filament wires from tensile tests found to be ~ 2130 MPa for ABS and ~ 4430 MPa for ABS-SCF filament.

3.2.2 Fabrication of test coupons

The dimensions of the test coupons for the tensile, flexural and fracture toughness cases are presented in Figure 3.1 and Table 3.1. The laminate test coupons were printed for mechanical testing. The coupons were printed with different lamina layups, materials, and process parameters, and these are presented in Table 3.2. The x, y, and z coordinates represent the global system for a laminate, while the local system for a laminate is indicated by *1*, *2*, and *3*, where *1* denotes the fiber direction, and *2* and *3* are transverse to the orientation of the fibers, as shown in Figure 3.1a.

Two significant process parameters governing the mesostructure of the printed laminates are layer thickness and raster angle. The raster angle (θ, °) defines the fiber orientation for the laminate layup, and the layer thickness (t) represents the thickness of the lamina of the printed laminates and also the cross-sectional size of the fibers (Figure 3.1a). Different types of unidirectional and bidirectional laminates can be printed by varying these process parameters. The lamina layup in the printed bidirectional laminates is balanced and symmetric. Laminates of two different layer thicknesses are printed, and the thickness of lamina (t_1) of the thick-layered laminate is double the thickness of lamina (t_2) of the thin-layered laminate. However, the thickness of all layers within a laminate is the same.

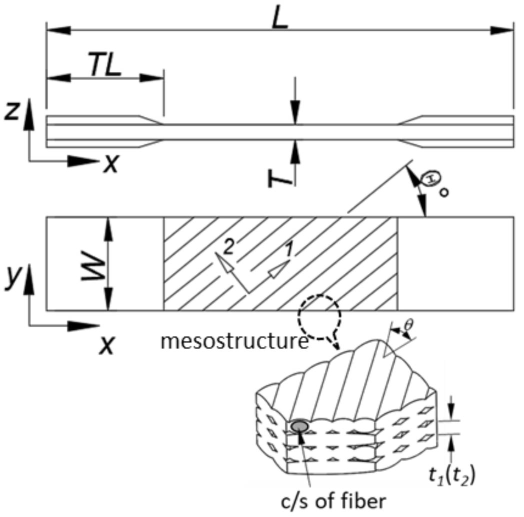

(a) *L*-Total length, *TS*- Tab size, *W*-Width, *T*-Thickness, *θ*-Fiber direction to *x*-axis (°)

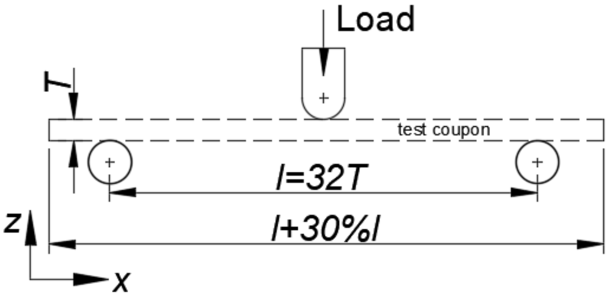

(b) *l*-Span distance, *l*+30%*l*- Total length, *T*-thickness, *W*-width

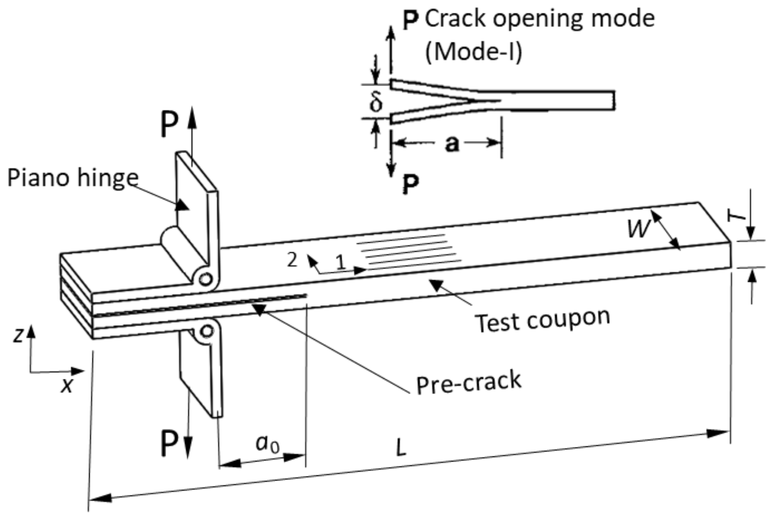

(c)

Figure 3.1. Dimensions (in mm) of test coupons: (a) tensile test coupon; (b) flexural test coupon; (c) interlaminar fracture toughness (Mode-I) test coupon.

Table 3.1. Dimensions of test coupons subjected to uniaxial tensile, bending tests and mode-I fracture tests.

	Coupon dimensions (mm)				
Laminate type	Layup No.	*L*	*W*	*T*	*TL*
Tensile test coupons					
Unidirectional	1–4	190	12.7	2.54	38
	5	127	25.4	2.54	19
Bidirectional	6, 7	200	25.4	2.54	30
Flexural test coupons					
Bidirectional	8, 9	$T = 3.17$, $W = 13$, $l = 32\text{T}$, $L = l + 30\%l$			
Fracture toughness test coupons					
Unidirectional	10	$T = 5.08, W = 25, L = 125, a_0=17$			

Table 3.2. Laminate layup, layer thickness, and materials used for printing laminate test coupons.

			Layer thickness (t)		Filament material	
Laminate type	Layup No.	Raster angle (θ)	$t_1 =$ 0.317	$t_2 =$ 0.158	ABS	ABS-SCF
Tensile test coupons						
Unidirectional	1	0°	×	×	×	×
	2	30°	×	×	×	×
	3	45°	×	×	×	×
	4	60°	×	×	×	×
	5	90°	×	×	×	×
Bidirectional	6a	$[0^\circ/90^\circ]_{2S}$	×	—	×	×
	6b	$[0^\circ/90^\circ]_{4S}$	—	×	×	×
	7a	$[45^\circ/-45^\circ]_{2S}$	×	—	×	×
	7b	$[45^\circ/-45^\circ]_{4S}$	—	×	×	×
Flexural test coupons						
Bidirectional	8a	$[0^\circ/90^\circ/0^\circ/90^\circ/0^\circ]_{S}$	×	—	×	×
	8b	$[0^\circ/90^\circ/0^\circ/90^\circ/0^\circ]_{2S}$	—	×	×	×
	9a	$[45^\circ/-45^\circ/45^\circ/-45^\circ/45^\circ]_{S}$	×	—	×	×
	9b	$[45^\circ/-45^\circ/45^\circ/-45^\circ/45^\circ]_{2S}$	—	×	×	×
Mode-I test coupons						
Unidirectional	10	0°	×	—	×	×

(where, × denotes printed coupons, *S* represents symmetry layup order)

For each test case, five coupons were printed. For instance, the layup 1 laminate can be one of two different layer thicknesses (t_1 and t_2) and one of two different materials (ABS or ABS-SCF), resulting in a total of 20 coupons being printed for this case alone, as presented in Table 3.2. The raster angle represents the orientation of fibers in the layers of the laminate along the *x*-axis of the test coupon. This means that the fibers in unidirectional laminate layup 1 are oriented only along the axis of loading, and in the other cases the fibers are oriented off-axis to the axis of loading. The difference in the bidirectional laminates of the same layup order is in the thickness of their layers. For example, bidirectional laminate layups 6a and 6b have the same layup order but consist of different layer thicknesses. Table 3.2 shows that the layers of laminate 6a are thicker than those of laminate layup 6b. Two different layup types of bidirectional laminates — cross-ply $[0°/90°]_n$ and angle ply $[45°/–45°]_n$ — were considered for investigation. Laminate test coupons for layups 1–7 were subjected to a uniaxial tensile load along the *x*-axis (Figure 3.1a), and layups 8 and 9 were subjected to a transverse load (Figure 3.1b), and layup 10 were subjected to crack opening load (Figure 3.1c).

The other process parameters used for printing were as follows: an extruder temperature of 235 °C, a substrate temperature of 80 °C, a printing speed of 50 mm/s, 1 shell, an overlap between adjacent fibers of 15%, and an infill density of 100%. The material is extruded through 400 µm diameter nozzle, and the desired thickness of layers can be obtained by governing the flow rate of material through nozzle and speed of nozzle head. A total of 140 coupons were printed for tensile testing, 40 coupons for flexural testing and 10 coupons for interlaminar fracture toughness testing on an Ultimaker printer.

3.2.3 Mechanical testing

Tests were conducted on an MTS testing machine equipped with a 10 kN load cell for measuring load. The displacements of the test coupons during deformation were recorded using a laser extensometer. A digital image correlation setup (LaVision GmbH) was employed during tensile testing of the coupons to measure strain in a multiaxial direction. Tests were carried out at a quasi-static loading rate of 1 mm/min. The mechanical behaviour of the printed laminates under two different load cases — uniaxial tensile test and bending test — was investigated. The printed parts resemble laminate structures, and therefore test standards follow the ASTM standards for traditional composite laminates. The test coupons were printed as per ASTM D3039 for tensile testing, ASTM D7264 for flexural testing and ASTM D5528 for Mode-I loading.

3.3 Results and Discussion

3.3.1 Tensile test results of unidirectionally printed parts

Tensile testing of a printed test coupon is shown in Figure 3.2. The variation in the mechanical properties of thick-layered and thin-layered unidirectional printed laminates with ABS and ABS-SCF is shown in Figures 3.3 and 3.4, respectively. The *x*-axis of the graphs indicates the fiber orientation of the unidirectional laminates with respect to the *x*-axis of the laminate. The *y*-axis indicates property of laminates, and the standard deviation error bar of corresponding values also can be seen in figures. The stiffness (E_x) and tensile strength (X_t) of the thin-layered laminates is higher than that of the thick-layered unidirectional laminates. The laminates with fibers oriented along the loading axis have higher stiffness and strength than the laminates whose fibers are off-angle to the loading axis. Layup 1 laminates have higher stiffness and strength than layup 5 laminates, whose fibers are not oriented along the loading axis. This means that the printed parts will have directional properties and their fibers are the main load-taking members of the part. The SCF reinforcements influenced the material properties of the printed parts. The stiffness of layup 1 laminates printed with composite material (ABS-SCF) is improved greatly, but not that of other unidirectional laminates. The effect of the reinforcements on the strength of the printed composite laminates is negative, especially for thick-layered composite laminates. The anisotropy in the properties of the printed composite parts is significant and mainly due to the presence of reinforcements.

Figure 3.2. Tensile testing of a printed test coupon.

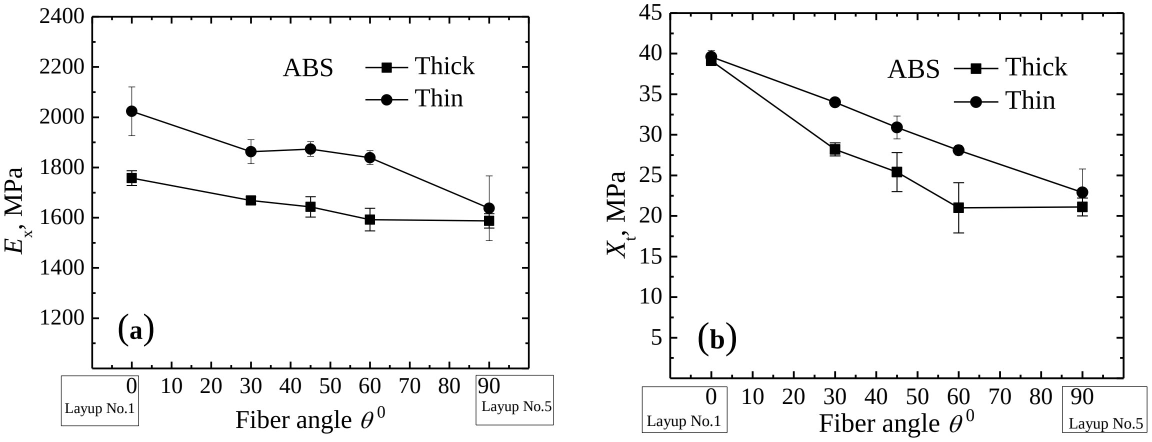

Figure 3.3. Mechanical properties of unidirectionally printed parts with ABS material: (a) E_x and (b) X_t for thick-layered (t_1) laminates and thin-layered (t_2) laminates.

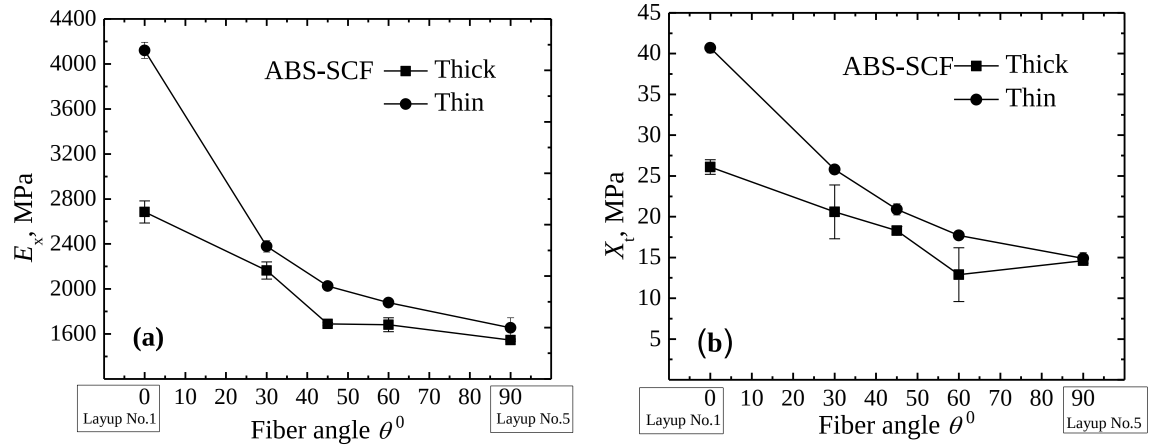

Figure 3.4. Mechanical properties of unidirectionally printed parts with ABS-SCF material: (a) E_x and (b) X_t for thick-layered (t_1) and thin-layered (t_2) laminates.

Next, the effect of lamina layup and layer thickness on the failure behaviour of printed laminates with ABS material is discussed. The stress–strain curves of the unidirectional laminates made of two different layer thicknesses are shown in Figure 3.5. Two types of failure modes, namely fiber breakage and fiber debonding, were seen in the laminates under tensile loads. Layup 1 laminates experienced two failure modes, and the other unidirectional laminate layups exhibited only the debonding failure mode under tensile loads. This difference is due to the orientation of the fibers in the other unidirectional laminates being off-axis to loading, and therefore a significant amount of load was shared by the interface between the fibers of the layers. The interface has a lower bonding strength than the fibers, and therefore the interface experiences early failure before breakage of the fibers. This can be observed in the stress–strain curves for the laminates, with layups 2–5 showing more early failure compared with layup 1. Furthermore, the strain to fracture is higher in thin-layered laminates than in thick-layered laminates. The mesostructures of the unidirectional laminates captured using microscope BX41M-LED from Olympus Corporation, are shown in Figure 3.6. The higher fracture strain in the thin-layered parts is the result of stronger bonding strength due to more bonding area between the adjacent fibers compared with that in the thick-layered parts.

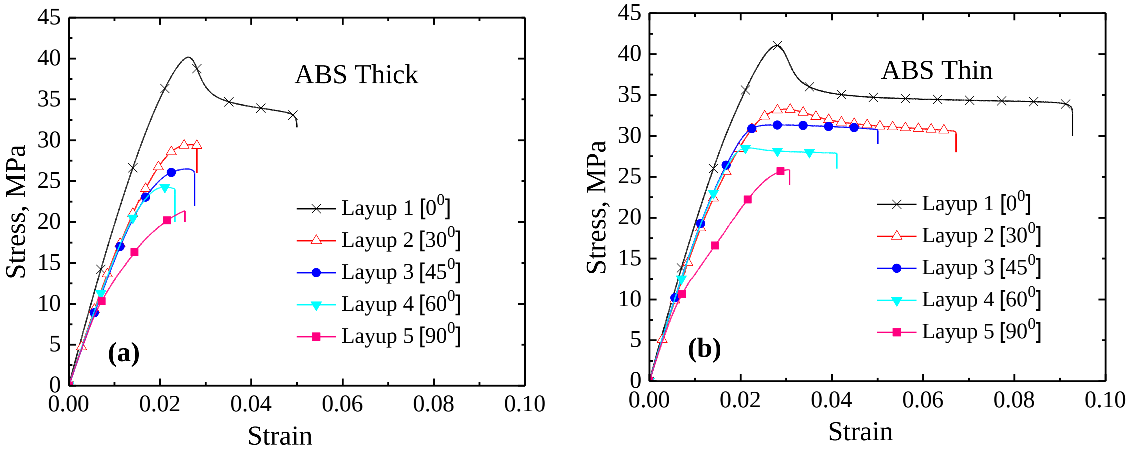

Figure 3.5. Stress–strain curves of unidirectional laminates for (a) thick-layered laminates and (b) thin-layered laminates.

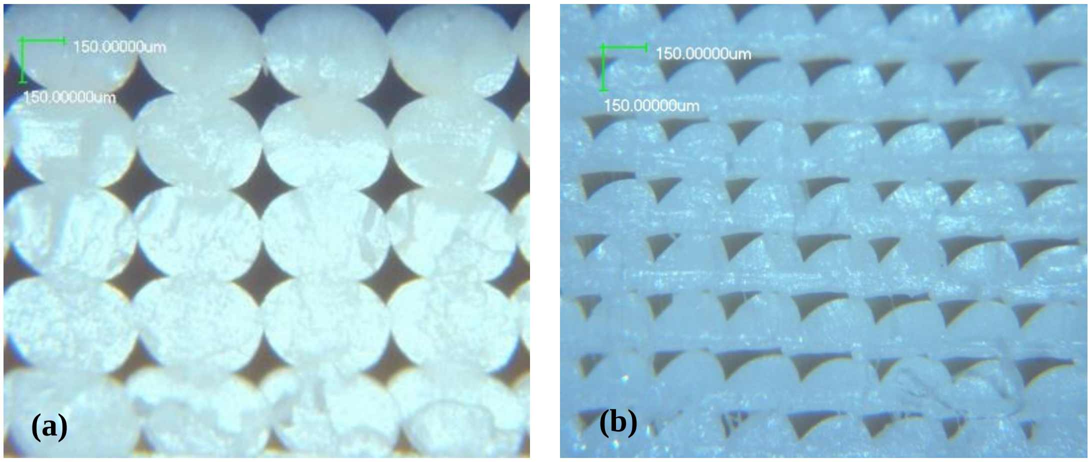

Figure 3.6. Mesostructure of unidirectionally printed laminates, (a) thick layered parts, (b) thin layered parts.

The mesostructure of the printed parts will contain voids inherited from the printing process. The difference in the results for certain thick and thin-layered laminate lay-ups is due to variation in the size of the voids in the printed laminates' mesostructure. The size of the voids in the thin-layered laminate is smaller than those in the thick-layered laminate, and the bonding is stronger between the fibers for laminates with a smaller void size and density. Void size affects the mechanical behaviour of unidirectional laminates more than that of bidirectional laminates. This effect could explain the difference in the stress–strain curves of the thick- and thin-layered unidirectional laminates as well as the bidirectional laminates. Though the parts were printed with 100 percent infill material, but in reality that the printed parts have voids. The percentage of voids in a layer is around 7.6 % of its volume in case of thicker layer (t_1), and 6.1% percent in case of thinner layer (t_2), but total void volume in thick and thin layered parts is nearly same in a printed part. The fracture lines of the five different layups of printed parts with ABS material then subjected to uniaxial tensile loads are shown in Figure 3.7.

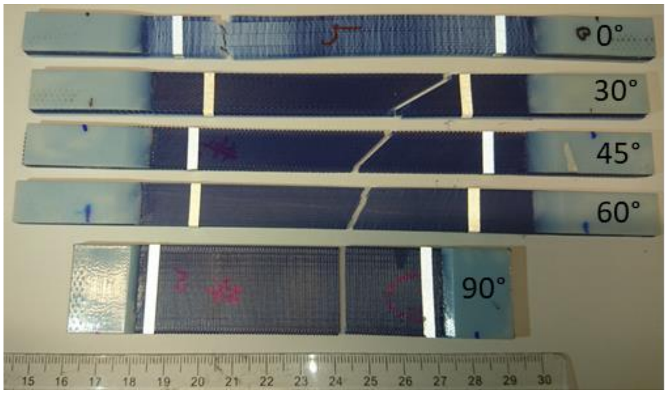

Figure 3.7. Fracture lines of ABS printed parts subjected to uniaxial tensile loads.

Next, the influence of lamina layup and layer thickness on the failure behaviour of the printed laminates with ABS-SCF material is discussed. The stress–strain curves of unidirectional laminates made of two different layer thicknesses are shown in Figure 3.8. The thin-layered unidirectional laminates are stiffer and stronger than the thick-layered laminates. The fracture strength and fracture strain of layup 1 laminates is greater than that of the other unidirectional laminates owing to the orientation of fibers in the other laminates being off-axis to loading. Also, the interface of the fibers in a layer shares a significant amount of load, and the bonding strength of the interface is lower than the strength of the fibers. This led to the fracture occurring at the interface of the fibers in laminate layups 2–5. The presence of SCF reinforcements in the composite laminates resulted in lower fracture strength as well as fracture strain compared with the laminates printed with only isotropic material. Figure 3.9 shows the fracture lines of the different unidirectional laminate layups 1–5. The angle of the fracture lines of the laminate follows the orientation of fibers in that laminate.

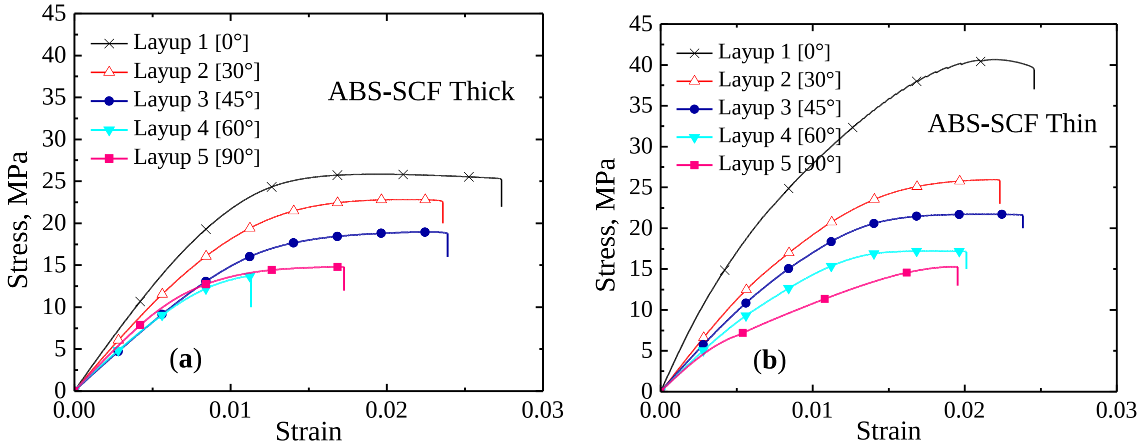

Figure 3.8. Stress–strain curves for (a) thick-layered and (b) thin-layered composite laminates.

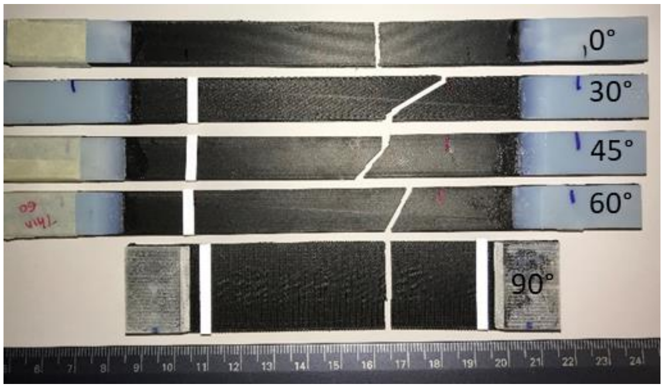

Figure 3.9. Fracture lines of the five different layups of ABS-SCF printed parts subjected to uniaxial tensile loads.

The mesostructures of the thick- and thin-layered composite laminates are shown in Figure 3.10. The size of the voids in the thin-layered laminate is smaller than those in the thick-layered laminate. In addition, the bonding strength is greater between the fibers for laminates with a smaller void size, leading to more contact area between adjacent fibers. Void size affects the mechanical behaviour of the unidirectional laminates more than that of the bidirectional laminates. Also, the effect is more significant in the composite laminates than in the isotropic laminates. This effect could explain the difference in the stress–strain curves of the thick- and thin-layered laminates fabricated with ABS and ABS-SCF materials. The size of the voids can be minimized with a lower layer thickness and greater overlap between the fibers. The variation in the results for different laminates is mainly due to changes in various aspects of their mesostructure, including material, size of the fibers, thickness of the layers, and orientation of the fibers.

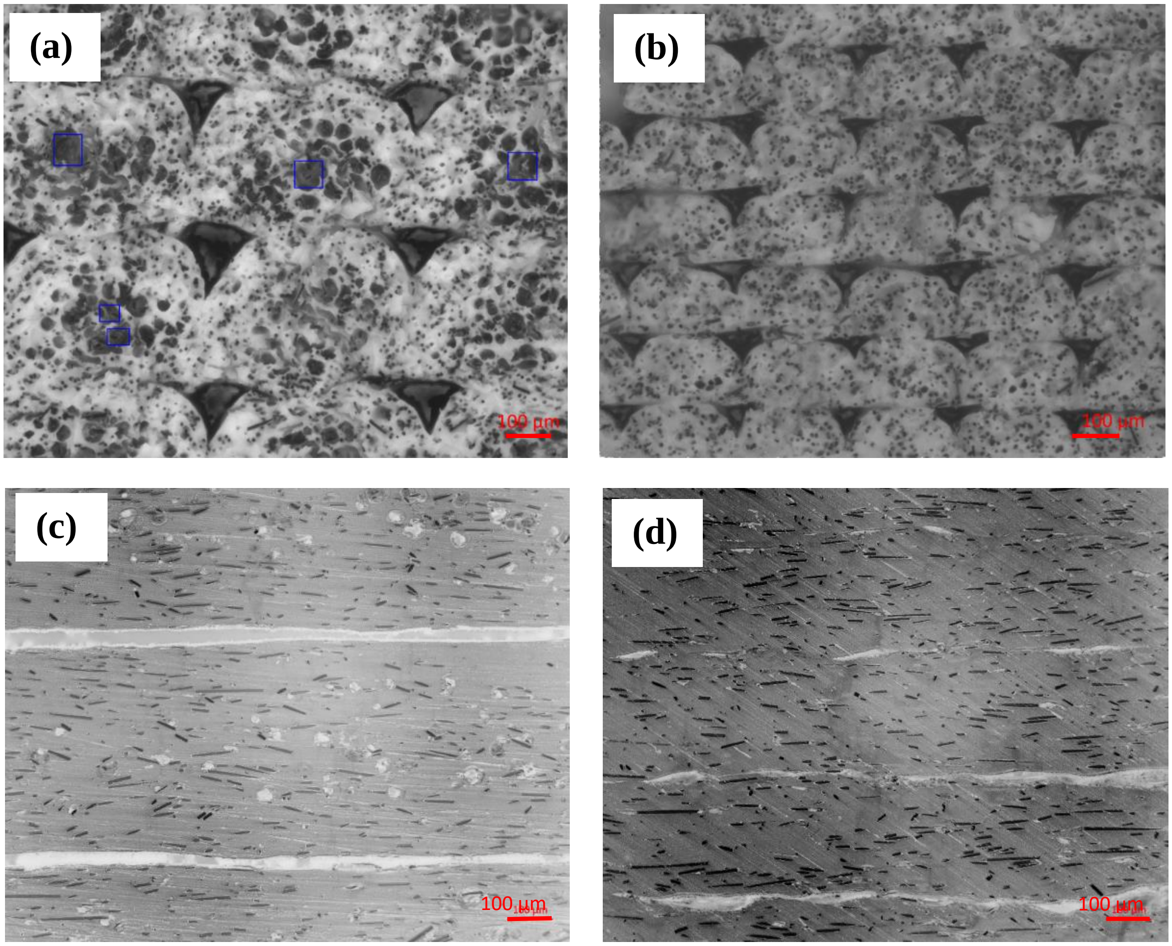

Figure 3.10. Mesostructure of the composite laminates. (a) Thick-layered laminates and (b) thin-layered laminates. Orientation of short carbon fiber reinforcements in the fibers of (c) thick-layered laminates and (d) thin-layered laminates.

In addition to the presence of voids, the composite laminates also contain SCF reinforcements in the fibers. The SCF reinforcements make the fiber brittle and therefore the composite laminate brittle. The bonding strength between the fibers as well as between the layers becomes weaker because of the presence of reinforcements at the interfaces, and this contributes to the brittleness of the composite laminate. Furthermore, layer thickness has a more significant effect on the properties of the composite laminates than on the properties of isotropic laminates. This effect is due to the fibers of the thick-layered composite laminates having voids within their cross-section, as shown in Figure 3.10a and 3.10c; however, this is not the case for isotropic fibers. Figure 3.10 shows the presence of voids within the cross-section of fibers of the thick-layered composite laminates; such voids are not seen in the fibers of the thin-layered composite laminates. Furthermore, thin-layered laminates contain SCF reinforcements that are more aligned with the direction of the fiber than are the reinforcements in the thick-layered laminates. These differences result in the thick-layered composite laminates being more prone to early failure than the thin-layered composite laminates.

3.3.2 Tensile test results of bidirectionally printed parts

Bidirectionally printed laminates with two different layup orders were tested: cross-ply laminates (layup 6) and angle-ply laminates (layup 7). The laminates with layups 6a and 7a are thick-layered laminates, and those with layups 6b and 7b are thin-layered laminates. The common practice in printing the parts is to orient the fibers of the layers perpendicular to each other in the alternate layers, i.e., the fibers are laid bidirectionally in the layers of the printed parts. The behaviour of the parts printed with such a printing pattern is investigated in this section.

Now, consider the tensile test results of bidirectional laminates printed with ABS material. The stress–strain curves of the bidirectionally printed laminates are shown in Figure 3.11. Tensile testing of bidirectional laminates with a digital image correlation setup is shown in Figure 3.12. The strain distribution just before propagation of the crack in the laminates subjected to tensile loading is shown in Figure 3.13. The failure strain of the thick-layered laminates is lower than that of the thin-layered laminates. Also, failure strain is higher for angle-ply laminates than for cross-ply laminates. The angle-ply bidirectional laminates experienced fiber breakage only, whereas the cross-ply laminates saw both failure modes. This means that the interaction of fibers between adjacent layers of the laminate played a role in sharing the applied load. Also, the failure is not sudden after the material yields elastically; rather, after stress reaches a maximum, the material deforms gradually with softening behaviour. Then, sudden failure happens when the applied strain is localized in one region, which leads to propagation of the existing voids in the printed parts. The thin-layered laminates are stronger and stiffer than the thick-layered laminates, and is because of higher bonding strength between the fibers of thin-layered laminates.

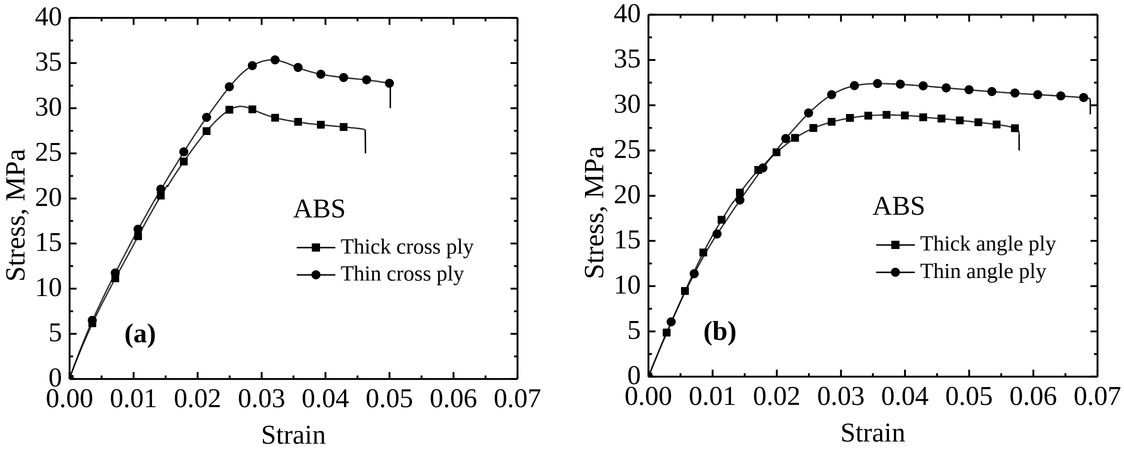

Figure 3.11. Stress–strain curves of bidirectional laminates for (*a*) cross-ply laminates and (*b*) angle-ply laminates.

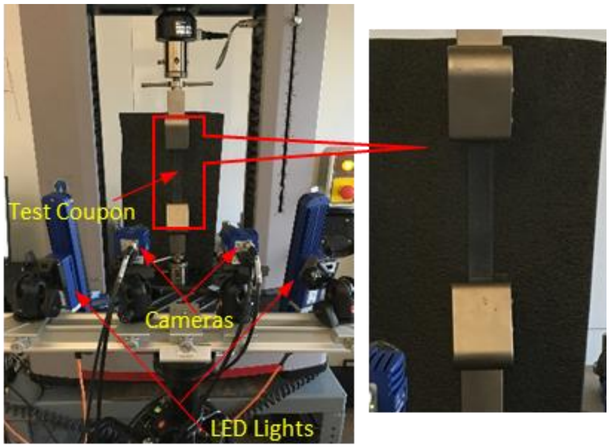

Figure 3.12. Tensile testing with a digital image correlation setup.

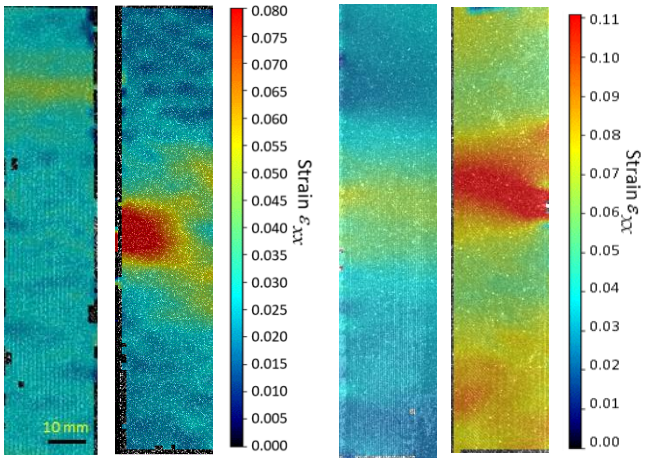

(a) **(b)** **(c)** **(d)**

Figure 3.13. Strain distribution in the laminates during tensile testing. Thick-layered laminates: (*a*) layup 6a and (*b*) layup 7a. Thin-layered laminates: (*d*) layup 6b and (*e*) layup 7b.

Let us now consider the failure behaviour of the bidirectional laminates printed with ABS-SCF material, whereby the influence of bidirectional layup order on the mechanical behaviour of printed parts is demonstrated. The stress–strain curves of the bidirectional laminates for cross-ply and angle-ply layup order are shown in Figure 3.14. The cross-ply laminates are stiffer and stronger than the angle-ply laminates, but the failure strain of angle-ply laminates is higher than that of the cross-ply laminates. The higher stiffness and strength in the cross-ply composite laminates is the result of the orientation of fibers as well as SCF reinforcements in them being aligned with the loading direction. The thin-layered bidirectional laminates have higher failure strength and failure strain than the thick-layered laminates. The strain distribution just before propagation of the crack in the cross-ply and angle-ply laminates subjected to tensile loading is shown in Figure 3.15. This strain distribution in the coupons is at a data point in the stress-strain curves just before the sudden drop in stress, and it is the strain for complete failure. The stress–strain curves of the laminates follow linear and nonlinear regions while deforming under tensile loading. This means that the matrix and SCF reinforcements deform elastically until the bonds break between them, and then the matrix deforms plastically until complete failure of the part. The softening region after the ultimate stress is smaller compared with the softening region of the laminates printed with ABS material only. Furthermore, the failure of the printed laminates does not exactly resemble the failure phenomenon of the traditional polymeric composite laminates, where sudden failure occurs immediately after the laminate yields elastically. The layup order influences bonding strength between the layers, meaning that bonding strength at the interface is not the same in unidirectional and bidirectional laminates. In the stress–strain curves of the laminates, note that the angle-ply laminates have a higher fracture strain than other layup order laminates. Also, the influence of bonding is significant in the unidirectional laminates with fibers oriented off-axis to loading. In summary, the mechanical properties — namely strength, stiffness, and fracture strain — of bidirectionally printed parts are better than those of unidirectional laminates containing fibers oriented off-axis to the loading axis. This is mainly due to the mesostructure that was produced during the printing of the parts. It means that the performance of the printed parts is governed by the mesostructure, and that in turn is governed by the printing process parameters.

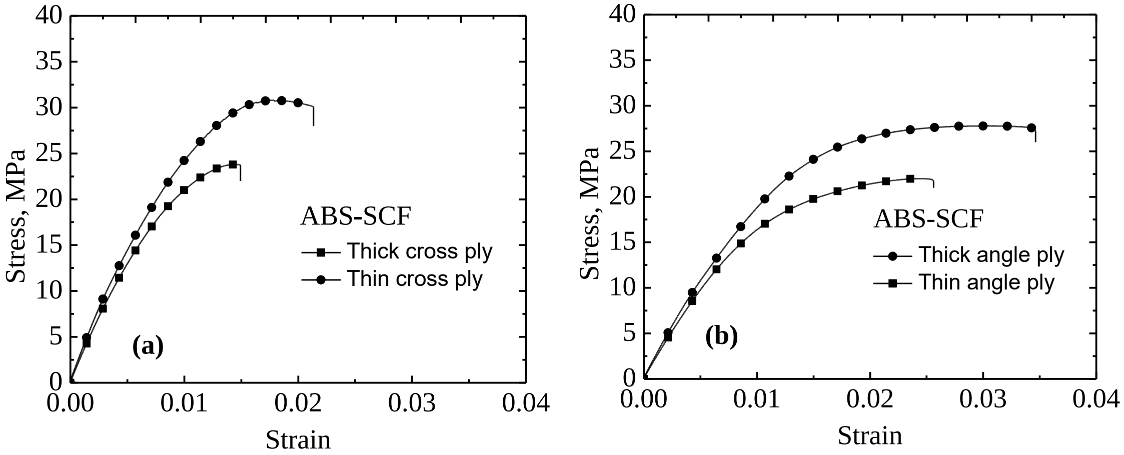

Figure 3.14. Stress–strain curve of (a) cross-ply and (b) angle-ply composite laminates.

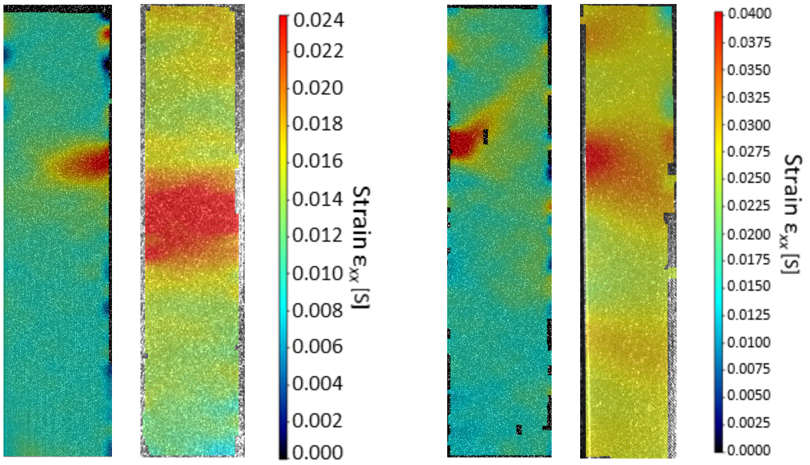

(a) **(b)** **(c)** **(d)**

Figure 3.15. Strain distribution in the printed composite laminates during uniaxial tensile testing of (a) thick-layered cross-ply laminates, (b) thin-layered cross-ply laminates, (c) thick-layered angle-ply laminates, and (d) thin-layered angle-ply laminates.

3.3.3 Flexural test results of bidirectionally printed parts

Three-point bending tests were conducted on cross-ply and angle-ply printed laminates. The bidirectionally printed laminates with layups 8a and 9a (thick-layered laminates), and those with layups 8b and 9b (thin-layered laminates) were subjected to a bending test. The layup order of the laminates is presented in Table 3.2. The influence of layer thickness, layup order, and SCF reinforcements on the mechanical behaviour of bidirectionally printed parts subjected to transverse loads is investigated in this section. A three-point bending test of printed coupon is shown in Figure 3.16. Load versus deflection curves are shown in Figure 3.17 for laminates printed with ABS material, while Figure 3.18 shows curves for laminates printed with ABS-SCF material.

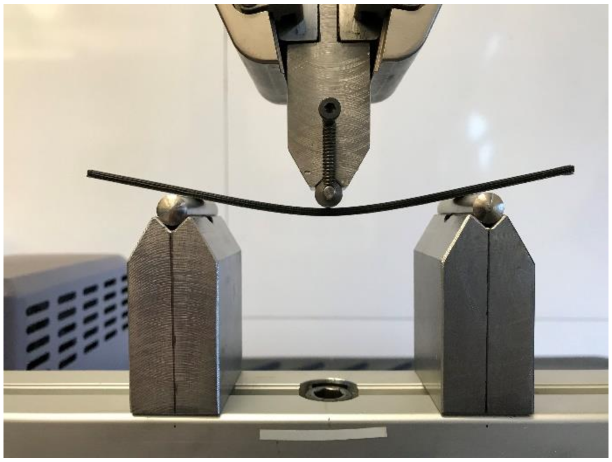

Figure 3.16. Bending test of printed test coupon.

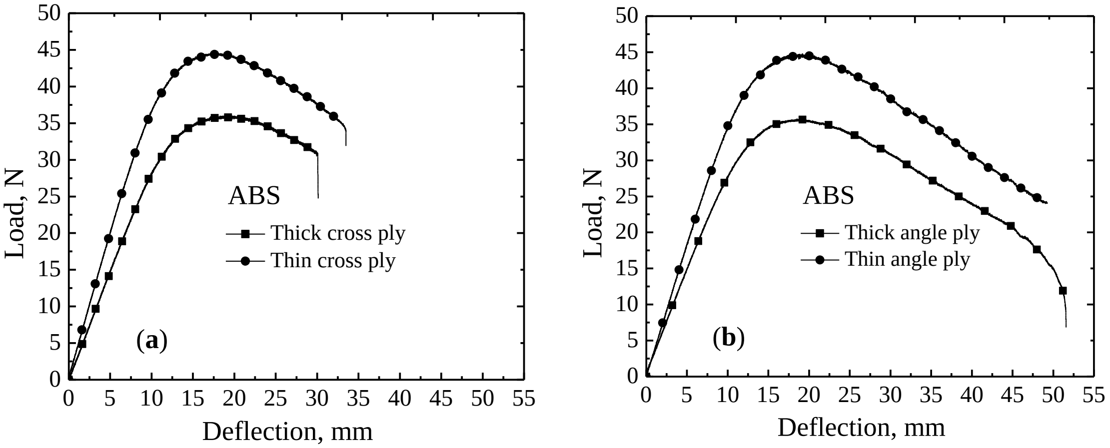

Figure 3.17. Load versus deflection curves of laminates printed with ABS material: (a) cross-ply laminates and (b) angle-ply laminates.

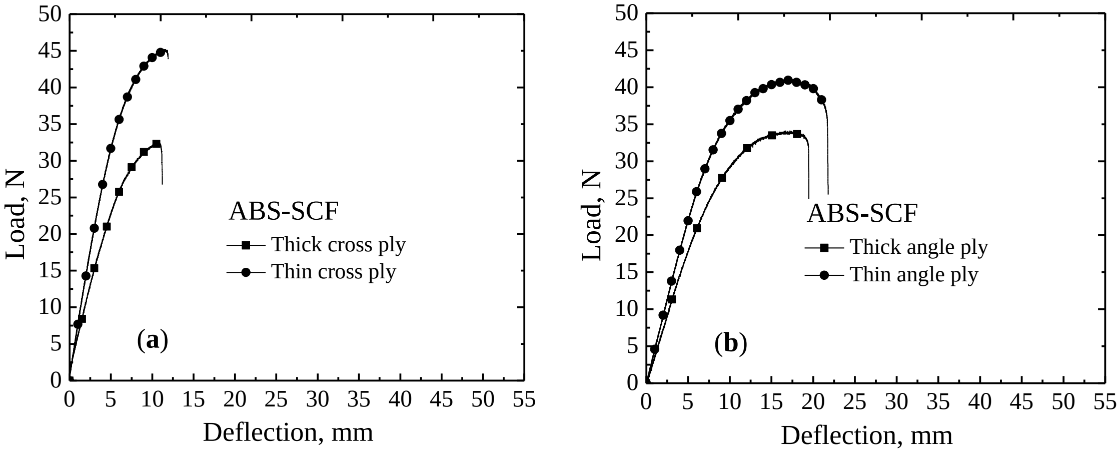

Figure 3.18. Load versus deflection curves of laminates printed with ABS-SCF material: (a) cross-ply laminates and (b) angle-ply laminates.

The load versus deflection curves illustrate that thin-layered laminates can withstand higher flexural load as well as deflection than thick-layered laminates. Further, angle-ply laminates can tolerate more deflection before the final failure than the cross-ply laminates of the same layer thickness. Also, laminates printed with ABS can sustain loads at higher deflection than composite laminates can. The presence of the SCF reinforcements in the composite laminates significantly influences the flexural properties; flexural stiffness is improved, but deflection is reduced. The failure behaviour of laminates printed with ABS material initially follows elastic behaviour until the peak load is reached, at which point there is softening behaviour before sudden failure occurs. The failure of composite laminates follows a similar trend, but the softening region is smaller than that in the laminates made only with ABS. This effect is mainly due to the presence of SCF reinforcements in these laminates, which further promotes brittleness in the laminates. Therefore, the composite laminates experience failure earlier than laminates printed with other material.

3.3.4 Interlaminar fracture toughness test results of unidirectionally printed parts

Interlaminar bonding strength of the printed laminates is assessed in this section. Interlaminar fracture toughness tests were conducted on printed test coupons of layup 10. Test results reveal the interlaminar fracture toughness of the printed laminates under crack opening mode. Interlaminar fracture toughness represents the bonding strength between the layers of the printed parts. Interlayer debonding (decohesion) of printed parts is also referred as delamination, which is one of the failure modes in traditional composite laminates. Test coupon subjecting to crack opening mode is shown in Figure 3.19. Load (P) versus crack opening displacement (δ) curves for the test coupons made of ABS as well as ABS-SCF material is shown in Figure 3.20a. Also, Figure 3.20b illustrates the fracture toughness (G_I) versus delamination length (a) of the coupons. The fracture toughness is calculated based on modified beam theory as described in the standard. Interlaminar bonding strength for the printed coupons with ABS material is higher than the coupons made of ABS-SCF material. This is because of that the SCF reinforcements influenced the inter-layer adhesion. The SCF reinforcements have higher thermal conductivity and that led to the extruded ABS-SCF material cool faster. Therefore, the extruded ABS-SCF material solidified before diffusing with the previously deposited material and this caused poor adhesion between adjacent fibers as well as layers. Thus, the interlaminar fracture toughness of the printed laminates with ABS-SCF is lower when compared to the laminates made of ABS material.

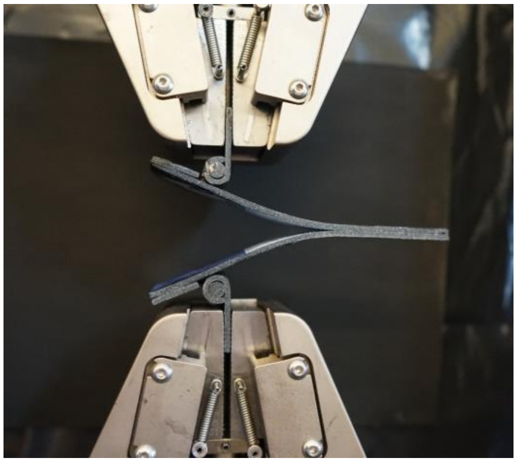

Figure 3.19. Printed test coupon under crack opening mode.

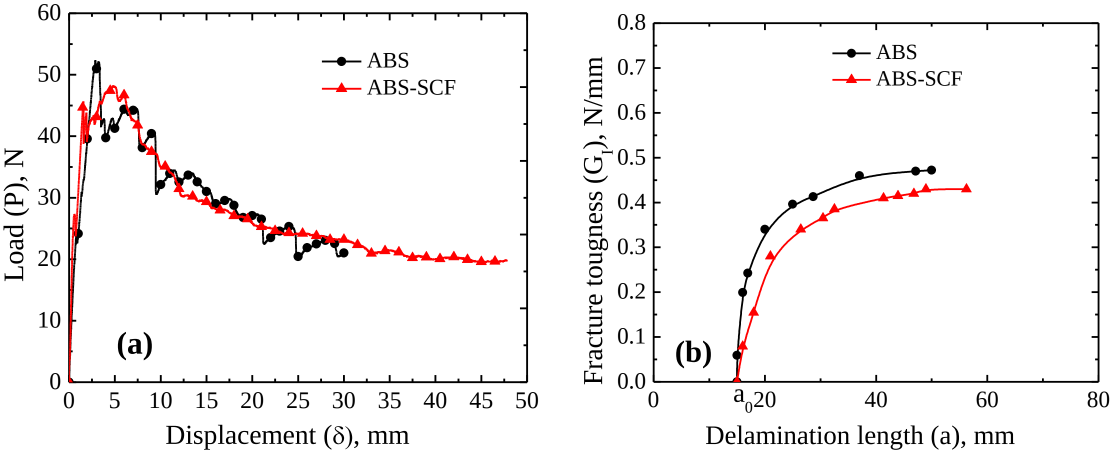

Figure 3.20. Interlaminar fracture toughness results of printed laminates under Mode-I loading (a) load versus displacement; (b) fracture toughness versus delamination length.

3.4 Conclusions

In this chapter, the mechanical behaviour of 3D printed parts subjected to tensile and flexural loads was investigated experimentally. This chapter also included a study of the impact of mesostructure on the overall mechanical properties of 3D printed parts. In particular, the influence of mesostructural features such as the orientation of fibers, layer thickness, and lamina layup on the properties of the printed parts was explored. The effect of SCF reinforcements on the properties of printed parts was also investigated. To carry out these investigations, parts were 3D printed unidirectionally as well as bidirectionally with two different layer thicknesses (thick and thin) and two different materials (ABS, ABS-SCF) for mechanical testing. The printed test coupons were subjected to uniaxial loading in tensile tests and transverse loading in flexural tests. A summary of the test results is as follows:

- Unidirectionally printed parts with fibers oriented along the tensile loading axis have higher stiffness and strength than parts whose fibers are off-angle to the loading axis. In other words, layup 1 test coupons have higher stiffness and strength than layup 5 coupons, whose fibers are not oriented along the tensile loading axis. This means that printed parts have directional properties and that their fibers are the main load-bearing members.

- Two aspects of mesostructure defined by the printing process parameters, namely raster angle (fiber orientation) and layer thickness, significantly influenced the mechanical properties of the printed parts. Thin-layered printed parts have better properties than thick-layered parts. In general, bidirectionally printed parts subjected to tensile and flexural loads perform better than unidirectionally printed parts, especially unidirectional parts with layups 2–5.

- The material and its constituents used for printing parts influence the final properties of the parts. In general, SCF reinforcements in ABS improve the stiffness of the printed parts, but strength and fracture strain in ABS-SCF parts are significantly lower than in parts printed with only ABS material. This is mainly due to the parts printed with ABS-SCF having enclosed voids within the fibers, which is not the case for parts printed with ABS material only.

- The failure behaviour of printed parts subjected to tensile and flexural loads reveals that, in general, the parts initially have an elastic region exhibiting plasticity with softening behaviour before sudden fracture occurs. Unidirectional parts whose fibers are not aligned with the tensile loading axis have a smaller softening region and are subject to early failure. This occurs because of lower bonding strength at the interface of adjacent fibers compared with bonding strength of the extruded fiber, and therefore the fracture lines in these parts follow the orientation of the fibers. The presence of SCF reinforcement in the printed parts causes the formation of enclosed voids, which results in a smaller softening region in such parts. Furthermore, the SCF reinforcements weakens the interlayer bonding of the printed parts.

- Finally, the mesostructure produced in 3D printed parts during the printing process governs the final material properties of the parts. In other words, anisotropy in the properties is mainly due to variation in the mesostructure of the printed parts. This raises an important question regarding the constitutive behaviour of the material of the printed parts and also the mechanics applicable in the effective design and analysis of structural parts for 3D printing. This question is addressed in the next chapter.

Chapter 4 Characterization of the Mechanical Behaviour of 3D Printed Parts: Laminate Mechanics

Summary: In this chapter, the mechanics of 3D printed parts with ABS (isotropic material) and ABS reinforced with short carbon fibers (ABS-SCF) (composite material) are explored. The results of mechanical testing from the previous chapter revealed that printed parts have directional properties. However, the constitutive material behaviour of the printed parts was not explored, and the structural mechanics for characterizing the behaviour of printed parts subjected to mechanical loads has yet to be defined. To address these questions, a detailed investigation of the material constitutive behaviour and mechanics of printed parts is carried out in this study.

4.1 Introduction

Constitutive relations are used to capture the behaviour of material in response to the stress testing of structural parts. In addition, the behaviour of parts subjected to mechanical loads can be characterized using structural mechanics, which facilitates the design and analysis of structural parts. The design and analysis of structural parts for 3D printing is challenging because of their anisotropic behaviour. This anisotropic nature is mainly due to a change in the material properties of the printed parts. The presence of anisotropy calls for the characterization of the constitutive behaviour of printed parts. This investigation allows for the effective design and analysis of a model for 3D printing.

The mechanical behaviour of parts consisting of continuous fibers can be characterized using laminate mechanics [102,135]. Laminate mechanics can also be employed to characterize the mechanical behaviour of parts fabricated with only thermoplastic filament material and no additional reinforcements [128–130]. The use of laminate mechanics implies that parts printed via FFF behave like laminate structures. Thus, laminate theory can be employed in the behavioural characterization of parts subjected to different loads during stress analysis. The layers of parts fabricated with short carbon fibers (SCF) can be treated as orthotropic lamina material, and the mechanical behaviour of such parts have been characterized using laminate mechanics [137]. So far, experimental characterization of composite parts fabricated with material containing continuous fiber [102–105,135,136] and discontinuous fiber [113,116,117,120,123,137] reinforcements has been explored, but their material modeling has not yet been attempted. Only limited literature exists using laminate mechanics and laminate theories to characterize the mechanical behaviour of printed composite parts, which is a gap addressed in the present work.

This chapter begins by using laminate mechanics to characterize the constitutive behaviour of parts fabricated with ABS or ABS-SCF material. Then, classical laminate theory is employed to characterize the mechanical behaviour of bidirectionally printed parts that are subjected to tensile and flexural loads. In addition, finite element (FE) failure analysis of printed parts is attempted using the first-ply failure criterion to reveal the relevance of such failure theories for printed parts.

4.2 Mechanics of 3D printed parts

4.2.1 Constitutive relation of materials

Constitutive relation of materials is considered in the analysis of 3D printed parts to account for their material behaviour. The coefficients of the constitutive matrix are functions of the elastic moduli of the material. The mechanical properties depend on the microstructure of the material. The number of independent coefficients in the constitutive matrix depends on the symmetry of the microstructure in the material planes. 3D printed parts behave like a laminate structure, with each layer acting as a lamina reinforced by unidirectional polymeric fibers. Such layers (laminae) of printed parts can be treated as orthotropic material. The constitutive relation for an orthotropic material is as follows:

$$\begin{Bmatrix} \sigma_{11} \\ \sigma_{22} \\ \sigma_{33} \\ \tau_{23} \\ \tau_{13} \\ \tau_{12} \end{Bmatrix} = \begin{bmatrix} C_{11} & C_{12} & C_{13} & 0 & 0 & 0 \\ C_{12} & C_{22} & C_{23} & 0 & 0 & 0 \\ C_{13} & C_{23} & C_{33} & 0 & 0 & 0 \\ 0 & 0 & 0 & C_{44} & 0 & 0 \\ 0 & 0 & 0 & 0 & C_{55} & 0 \\ 0 & 0 & 0 & 0 & 0 & C_{66} \end{bmatrix} \begin{Bmatrix} \varepsilon_{11} \\ \varepsilon_{22} \\ \varepsilon_{33} \\ \gamma_{23} \\ \gamma_{13} \\ \gamma_{12} \end{Bmatrix}; \text{ or } \{\sigma\} = [\boldsymbol{C}]\{\varepsilon\} \tag{4.1}$$

where C_{ij} are elements of the constitutive matrix ***C***. The strain–stress relation for an orthotropic material obtained by inverting eq.4.1 can be written as

$$\begin{Bmatrix} \varepsilon_{11} \\ \varepsilon_{22} \\ \varepsilon_{33} \\ \gamma_{23} \\ \gamma_{13} \\ \gamma_{12} \end{Bmatrix} = \begin{bmatrix} S_{11} & S_{12} & S_{13} & 0 & 0 & 0 \\ S_{12} & S_{22} & S_{23} & 0 & 0 & 0 \\ S_{13} & S_{23} & S_{33} & 0 & 0 & 0 \\ 0 & 0 & 0 & S_{44} & 0 & 0 \\ 0 & 0 & 0 & 0 & S_{55} & 0 \\ 0 & 0 & 0 & 0 & 0 & S_{66} \end{bmatrix} \begin{Bmatrix} \sigma_{11} \\ \sigma_{22} \\ \sigma_{33} \\ \tau_{23} \\ \tau_{13} \\ \tau_{12} \end{Bmatrix}; \text{ or } \{\varepsilon\} = [\boldsymbol{S}]\{\sigma\} \tag{4.2}$$

where ***S*** is the compliance matrix and the coefficients of the matrix are

$$S_{11} = \frac{1}{E_1}, S_{12} = -\frac{\nu_{12}}{E_2}, S_{13} = -\frac{\nu_{13}}{E_1}, S_{22} = \frac{1}{E_2}, S_{23} = -\frac{\nu_{23}}{E_2}, S_{33} = \frac{1}{E_3}, S_{44} = \frac{1}{G_{23}}, S_{55} = \frac{1}{G_{13}}, S_{66} = \frac{1}{G_{12}} \tag{4.3}$$

The coordinate system *1*, *2*, and *3* is a lamina (local) coordinate system; axis *1* is along the fiber, axis *2* is transverse to the fiber, and axis *3* is normal to the *1–2* plane, i.e., along the thickness of the layer. The coefficients C_{ij} of the ***C*** matrix for an orthotropic material are obtained by inverting the ***S*** matrix. The constitutive matrix for an orthotropic material contains nine independent coefficients. The elastic constants required to describe the material are as follows: Young's moduli of a layer along axes *1*, *2*, and *3*, respectively E_1, E_2, E_3; the shear moduli G_{12}, G_{13}, G_{23}; and Poisson's ratios $\nu_{12}, \nu_{13}, \nu_{23}$. Also, the relation $E_i \nu_{ji} = E_j \nu_{ij}$ (no sum on *i* and *j*) for *i*,*j* = 1, 2, 3 and $i \neq j$ holds for orthotropic materials.

For an isotropic material, $E_1 = E_2 = E_3 = E$, $G_{12} = G_{13} = G_{23} = G$, and $\nu_{12} = \nu_{13} = \nu_{23} = \nu$. Then, the coefficients in the constitutive matrix of eq. 4.1 become

$$C_{11} = C_{22} = C_{33} = \frac{E(1-\nu)}{(1-2\nu)(1+\nu)}, C_{12} = C_{13} = C_{23} = \frac{E\,\nu}{(1-2\nu)(1+\nu)}, C_{44} = C_{55} = C_{66} = G \quad (4.4)$$

and the strain–stress relation for an isotropic material is obtained by replacing the elastic constants in eq. 4.3 with elastic constants of the isotropic material.

The strain–stress relation for lamina in a plane stress case is obtained from eq. 4.2 by setting $\sigma_{33} = 0, \tau_{23} = 0, \tau_{13} = 0$ and is written as

$$\begin{Bmatrix} \varepsilon_{11} \\ \varepsilon_{22} \\ \gamma_{12} \end{Bmatrix} = \begin{bmatrix} S_{11} & S_{12} & 0 \\ S_{12} & S_{22} & 0 \\ 0 & 0 & S_{66} \end{bmatrix} \begin{Bmatrix} \sigma_{11} \\ \sigma_{22} \\ \tau_{12} \end{Bmatrix}, \text{ or } \quad \{\varepsilon\} = [\boldsymbol{S}]\{\sigma\} \qquad (4.5)$$

The coefficients of the compliance matrix ***S*** are available in eq. 4.3. The reduced constitutive relation of plane stress for an orthotropic material is obtained by inverting eq. 4.5 as follows:

$$\begin{Bmatrix} \sigma_{11} \\ \sigma_{22} \\ \tau_{12} \end{Bmatrix} = \begin{bmatrix} Q_{11} & Q_{12} & 0 \\ Q_{12} & Q_{22} & 0 \\ 0 & 0 & Q_{66} \end{bmatrix} \begin{Bmatrix} \varepsilon_{11} \\ \varepsilon_{22} \\ \gamma_{12} \end{Bmatrix}, \text{ or } \quad \{\sigma\} = [\boldsymbol{Q}]\{\varepsilon\} \qquad (4.6)$$

where Q_{ij} are the coefficients of the reduced stiffness matrix $\boldsymbol{Q}$ for plane stress, given by

$$Q_{11}=\frac{S_{22}}{S_{11}S_{22}-S_{12}^2}=\frac{E_1}{1-\nu_{12}\nu_{21}},Q_{12}=\frac{S_{12}}{S_{11}S_{22}-S_{12}^2}=\frac{\nu_{12}E_1}{1-\nu_{12}\nu_{21}},Q_{22}=\frac{S_{11}}{S_{11}S_{22}-S_{12}^2}=\frac{E_2}{1-\nu_{12}\nu_{21}},Q_{66}=\frac{1}{S_{66}}=G_{12} \quad (4.7)$$

Note that the reduced stiffness matrix's components involve only four independent material constants, E_1, E_2, ν_{12}, and G_{12}. This results in the number of elastic constants for an orthotropic material in a plane stress case being reduced to four. These elastic constants are required to characterize the mechanical behaviour of printed parts via FFF, as these parts resemble laminates. These unknown constants can be calculated using tensile test results for three different specimens, as explained next.

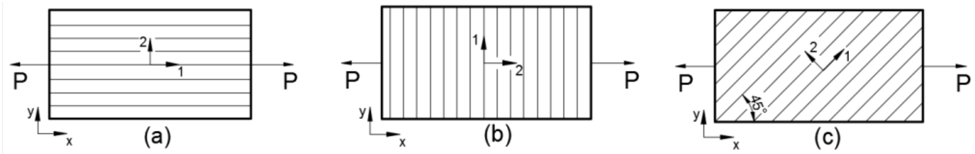

Figure 4.1. Uniaxial tensile loading of parts printed unidirectionally with fiber oriented (a) along the axis of loading, (b) normal to the axis of loading, and (c) off-axis to the axis of loading.

Initially, let us consider a tensile testing scenario in which a test coupon is printed unidirectionally with the fibers aligned along the axis of loading. The test specimen is subjected to uniaxial tensile loading, as shown in Figure 4.1a. The properties of the lamina (E_1, ν_{12} and X_t) can be calculated from the tensile test results for this case:

$$E_1=\frac{\Delta\sigma_{11}}{\Delta\varepsilon_{11}}, \qquad \nu_{12}=\frac{-\varepsilon_{22}}{\varepsilon_{11}}, \qquad X_t=\frac{P_{\text{ult}}}{A} \qquad (4.8)$$

where ε_{11} and ε_{22} are the longitudinal strain and lateral strain, respectively; P_{ult} is the ultimate tensile load; and A is the cross-sectional area of the test specimen.

Now, consider a tensile testing scenario in which a tensile test coupon is printed unidirectionally with the fiber oriented normal to the axis of loading. The test coupon is subjected to a uniaxial tensile load (Figure 4.1b). The properties E_2 and Y_t are calculated using the following equations from the test results for this case:

$$E_2 = \frac{\Delta\sigma_{22}}{\Delta\varepsilon_{22}}, \quad Y_t = \frac{P_{\text{ult}}}{A} \tag{4.9}$$

The stiffness properties should satisfy the reciprocal relation $\nu_{12}/E_1 = \nu_{21}/E_2$, where ν_{12} is obtained from the earlier case and $\nu_{21} = -\varepsilon_{11}/\varepsilon_{22}$ is calculated from this case.

Let us now consider a tensile testing scenario in which a tensile test coupon is printed unidirectionally with the fiber oriented off-angle to the axis of loading. In this case, the fibers are oriented off-axis at 45° to the axis of loading (Figure 4.1c). These test results are useful to calculate the in-plane shear properties G_{12} and S of the lamina using the modulus (E_x) in the x-direction:

$$E_x = \frac{\Delta\sigma_x}{\Delta\varepsilon_x} \tag{4.10}$$

The relation between the principal *1–2* coordinates and the non-principal *x–y* coordinates is established through the transformation matrix, which is useful in this case to calculate the shear modulus G_{12}. The results are given by

$$G_{12} = \frac{1}{\dfrac{4}{E_x} - \dfrac{1}{E_1} - \dfrac{1}{E_2} + \dfrac{2\nu_{12}}{E_1}} \tag{4.11}$$

The calculation of in-plane shear strength *S* is explained in the latter part of the next section. For further details about the procedure for calculating the elastic constants of lamina reinforced with unidirectional fibers, refer to [152] .

4.2.2 Classical laminate theory for characterizing the mechanical behaviour of printed parts

Figure 4.2 shows a two-layer plate 3D printed via FFF, with the fibers oriented in layers 1 and 2 at 0° and 90°, respectively, to the *x*-axis of the plate.

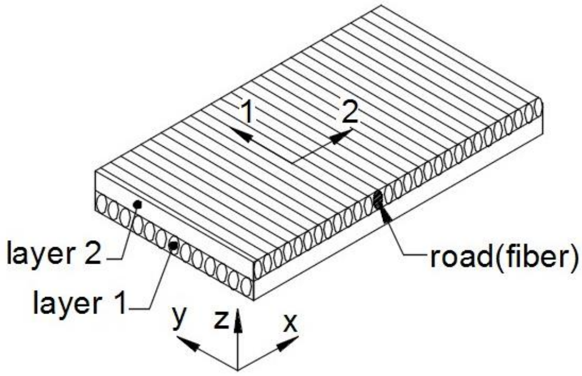

Figure 4.2. Plate fabricated with fused deposition modeling in 0° and 90° raster orientation.

The experimental work in the previous chapter revealed that printed parts with ABS or ABS-SCF material have directional properties. Further, the extruded fibers of a printed part are the load-bearing members, meaning that parts behave like traditional laminate structures. The main difference between traditional laminates and 3D printed parts is that the laminae of the traditional laminate have more than one high-strength continuous fiber across their thickness, but the layers of the printed parts have only one low-strength polymeric (or composite) fiber across their thickness. In general, the internal architecture of a part fabricated via FFF is similar to that of a traditional fiber-reinforced laminate structure. Therefore, laminate mechanics and laminate theories are employed here to characterize the mechanical behaviour of 3D printed parts. The constitutive relation for a lamina was defined in eq. 4.6 and is rewritten here:

$$\begin{Bmatrix}\sigma_{11}\\ \sigma_{22}\\ \tau_{12}\end{Bmatrix}=\begin{bmatrix}Q_{11} & Q_{12} & 0\\ Q_{12} & Q_{22} & 0\\ 0 & 0 & Q_{66}\end{bmatrix}\begin{Bmatrix}\varepsilon_{11}\\ \varepsilon_{22}\\ \gamma_{12}\end{Bmatrix} \tag{4.12}$$

Refer to Figure 4.2 for the global coordinate system (*x*, *y*, *z*) for a laminate plate and the local coordinate system (*1*, *2*, *3*) for a lamina.

The displacements for a lamina from classical laminate theory (CLT) are given as

$$\begin{aligned} u(x,y,z) &= u_0(x,y)+z\phi_x(x,y)\\ v(x,y,z) &= v_0(x,y)+z\phi_y(x,y)\\ w(x,y,z) &= w_0(x,y)\end{aligned} \tag{4.13}$$

From the Kirchhoff–Love hypothesis for a thin plate, the rotation terms in eq. 4.13 become $\phi_x = -\partial w_0/\partial x,\ \phi_y = -\partial w_0/\partial y$. The strains of the laminate are written as

$$\begin{Bmatrix}\varepsilon_{xx}\\ \varepsilon_{yy}\\ \gamma_{xy}\end{Bmatrix}=\begin{Bmatrix}\varepsilon_{xx}^0\\ \varepsilon_{yy}^0\\ \gamma_{xy}^0\end{Bmatrix}+z\begin{Bmatrix}k_{xx}\\ k_{yy}\\ k_{xy}\end{Bmatrix}, \qquad \text{or } \{\varepsilon\}=\{\varepsilon^0\}+z\{k\} \tag{4.14}$$

where ε_{xx}^0 and ε_{yy}^0 are mid-plane strains in the laminate; γ_{xy}^0 is the mid-plane shear strain in the laminate; k_{xx} and k_{yy} are bending curvatures in the laminate; k_{xy} is the twisting curvature in the laminate; and *z* is the distance from the mid-plane in the thickness direction.

The constitutive relation for a lamina in laminate co-ordinate system (*x*, *y*, *z*) is written as

$$\begin{Bmatrix}\sigma_{xx}\\ \sigma_{yy}\\ \tau_{xy}\end{Bmatrix}=\begin{bmatrix}\overline{Q}_{11} & \overline{Q}_{12} & 0\\ \overline{Q}_{12} & \overline{Q}_{22} & 0\\ 0 & 0 & \overline{Q}_{66}\end{bmatrix}\begin{Bmatrix}\varepsilon_{xx}\\ \varepsilon_{yy}\\ \gamma_{xy}\end{Bmatrix}, \qquad \text{or } \{\sigma\}=\left[\overline{\mathbf{Q}}\right]\{\varepsilon\} \tag{4.15}$$

where $\overline{Q}_{ij}$ are transformed material constants and the elements of $\overline{Q}_{ij}$ are given as

$$\left[\overline{\boldsymbol{Q}}\right] = [T]^{-1}[\boldsymbol{Q}][T]^{-T} \tag{4.16}$$

where $[T]$ is a transformation matrix. $[T]$ is defined as follows:

$$[T] = \begin{bmatrix} c^2 & s^2 & 2cs \\ s^2 & c^2 & -2sc \\ -cs & cs & c^2 - s^2 \end{bmatrix} \tag{4.17}$$

where c is $\cos\theta$, s is $\sin\theta$, and θ is the fiber orientation in an anticlockwise direction to the x-axis. The resultant force and moment per unit width for a laminate with n layers are expressed as

$$\begin{Bmatrix} N_{xx} \\ N_{yy} \\ N_{xy} \end{Bmatrix} = \int_{-h/2}^{h/2} \begin{Bmatrix} \sigma_{xx} \\ \sigma_{yy} \\ \tau_{xy} \end{Bmatrix} dz = \sum_{k=1}^{n} \int_{h_k}^{h_{k+1}} \begin{Bmatrix} \sigma_{xx} \\ \sigma_{yy} \\ \tau_{xy} \end{Bmatrix}_k dz\,, \qquad \{N\} = \sum_{k=1}^{n} \int_{h_k}^{h_{k+1}} \{\sigma\}\, dz \tag{4.18}$$

$$\begin{Bmatrix} M_{xx} \\ M_{yy} \\ M_{xy} \end{Bmatrix} = \int_{-h/2}^{h/2} \begin{Bmatrix} \sigma_{xx} \\ \sigma_{yy} \\ \tau_{xy} \end{Bmatrix} z\,dz = \sum_{k=1}^{n} \int_{h_k}^{h_{k+1}} \begin{Bmatrix} \sigma_{xx} \\ \sigma_{yy} \\ \tau_{xy} \end{Bmatrix}_k z\,dz\,, \ \{M\} = \sum_{k=1}^{n} \int_{h_k}^{h_{k+1}} \{\sigma\}\, z\,dz \tag{4.19}$$

Using eq. 4.14 and 4.15, eq. 4.18 and 4.19 become

$$\{N\} = \sum_{k=1}^{n} \left[\overline{\boldsymbol{Q}}\right] \left[\int_{h_k}^{h_{k+1}} \{\varepsilon^0\}\, dz + \int_{h_k}^{h_{k+1}} \{k\}\, z\,dz \right] \tag{4.20}$$

$$\{N\} = [\boldsymbol{A}]\{\varepsilon^0\} + [\boldsymbol{B}]\{k\} \tag{4.21}$$

$$\{M\} = \sum_{k=1}^{n} \left[\overline{\boldsymbol{Q}}\right] \left[\int_{h_k}^{h_{k+1}} \{\varepsilon^0\}\, z\,dz + \int_{h_k}^{h_{k+1}} \{k\}\, z^2 dz \right] \tag{4.22}$$

$$\{M\} = [\boldsymbol{B}]\{\varepsilon^0\} + [\boldsymbol{D}]\{k\} \tag{4.23}$$

where N_{xx} and N_{yy} represent the normal forces per unit width in the x and y directions, respectively; N_{xy} is the shear force; M_{xx} and M_{yy} denote the bending moments in the y–z and x–z planes; M_{xy} is the twisting moment; and $[\boldsymbol{A}]$, $[\boldsymbol{B}]$, and $[\boldsymbol{D}]$ are the extensional stiffness matrix, coupling stiffness matrix, and bending stiffness matrix for the laminate, respectively. The matrices $[\boldsymbol{A}]$, $[\boldsymbol{B}]$, and $[\boldsymbol{D}]$ are functions of each lamina stiffness matrix $[\overline{\boldsymbol{Q}}]$and the distance (z) from the mid-plane of the laminate to the laminas, where the stiffness matrices are written as

$$[\boldsymbol{A}]=\sum_{k=1}^{N}\left[\overline{\boldsymbol{Q}}\right]\int_{h_k}^{h_{k+1}} dz\,,\ [\boldsymbol{B}]=\sum_{k=1}^{N}\left[\overline{\boldsymbol{Q}}\right]\int_{h_k}^{h_{k+1}} z\,dz\,,\ [\boldsymbol{D}]=\sum_{k=1}^{N}\left[\overline{\boldsymbol{Q}}\right]\int_{h_k}^{h_{k+1}} z^2\,dz \tag{4.24}$$

The mid-plane strains and curvatures can be calculated from eq. 4.21 and 4.23, once we know the normal force and moment acting on a lamina. A symmetric laminate layup will have identical lamina material, thickness, and fiber orientation located at an equal distance above and below the mid-plane of the laminate. For a symmetric laminate, the coupling matrix $[\boldsymbol{B}] = [0]$, and therefore there is no extension–bending coupling. Then, the strains for a symmetric laminate subjected to in-plane forces are given from eq. 4.21 as

$$\begin{Bmatrix}\varepsilon_{xx}^{0}\\ \varepsilon_{yy}^{0}\\ \gamma_{xy}^{0}\end{Bmatrix}=[\boldsymbol{A}]^{-1}\begin{Bmatrix}N_{xx}\\ N_{yy}\\ N_{xy}\end{Bmatrix} \tag{4.25}$$

Strains for a symmetric laminate subjected to only transverse loads are given from eq. 4.23 as

$$\begin{Bmatrix}k_{xx}\\ k_{yy}\\ k_{xy}\end{Bmatrix}=[\boldsymbol{D}]^{-1}\begin{Bmatrix}M_{xx}\\ M_{yy}\\ M_{xy}\end{Bmatrix} \tag{4.26}$$

Uniaxial tensile loading along the x-axis: In the uniaxial tensile test, the load is applied in the x-axis direction. For laminate thickness h, $N_{xx}=h\sigma_{xx}$ $N_{yy} = 0$, and $N_{xy} = 0$. The stress–

strain relation for the uniaxial tensile test is $\sigma_{xx} = E_{xx}\varepsilon_{xx}^{0}$. Using the relation eq. 4.25, the modulus of elasticity along the *x*-axis direction of the laminate is calculated as follows:

$$E_{xx} = \frac{1}{[A^{-1}]_{11}h} \tag{4.27}$$

Flexural loads along the z-axis: In the three-point bending test, the load is applied in the *z*-axis direction. For laminate thickness *h*, $M_{xx} \neq 0$, $M_{yy} = 0$, and $M_{xy} = 0$. The relationship between flexural stress and stiffness is written as $E_x^f = \sigma_{xx}^f / \varepsilon_{xx}^f$. Using eq. 4.26, the flexural modulus of elasticity of the laminate along the *x*-axis direction is given as follows:

$$E_x^f = \frac{12}{[D^{-1}]_{11}h^3} \tag{4.28}$$

The elastic moduli E_1, E_2, G_{12}, and v_{12} of the lamina, which were found from the experimental tensile test results, can be used in the calculation of matrices [***A***], [***B***], and [***D***]. Then, E_{xx} and E_x^f of the laminate can be calculated using eq. 4.27 and 4.28, respectively. More details about laminate theory are available in [152].

First-ply criterion for failure analysis of printed parts: In the first-ply failure criterion, the part is said to have failed when the one of the plies (layer/lamina) of the part meets the failure criterion. Here, Tsai–Hill failure theory is employed for the preliminary failure investigation of printed parts. The failure criterion for a planar stress is written as

$$\frac{\sigma_1^2}{X_t^2} - \frac{\sigma_1\sigma_2}{X_t^2} + \frac{\sigma_2^2}{Y_t^2} + \frac{\tau_{12}^2}{S^2} = 1 \tag{4.29}$$

Failure analysis is performed using Altair Hyperworks commercial FE software. More details about FE modeling of composite laminates can be found in the Altair manual[153]. The outline of the FE method for the analysis of printed parts is presented at end of this section.

Special case: A unidirectional laminate with off-axis fibers is subjected to a tensile load. The stress in that laminate can be written as

$$\sigma_1 = \sigma_x \cos^2\theta \ , \ \sigma_2 = \sigma_x \sin^2\theta \, , \tau_{12} = -\sigma_x \sin\theta \ \cos\theta \qquad (4.30)$$

Upon substituting of the above equation in eq. 4.29, it can be written as

$$\frac{\cos^4\theta}{X^2} + \left[\frac{1}{S^2} - \frac{1}{X^2}\right]\cos^2\theta \sin^2\theta + \frac{\sin^4\theta}{Y^2} = \frac{1}{\sigma_x^2} \qquad (4.31)$$

Shear strength (S) can then be calculated from the above equation.

4.2.3 Boundary value problem for finite element analysis of printed parts

The strong form of the boundary value problem for the linear elastostatic of a thin plate can be written as

$$\sigma_{ij,x_j} + f_i = 0$$ Equilibrium equations (4.32)

$$t_i = \sigma_{ij} n_j$$ Traction conditions on boundary surface Γ_σ (4.33)

$$u_i = \hat{u}_i$$ Displacement conditions on boundary surface Γ_u (4.34)

The strain–displacement relation can be given as

$$\varepsilon_{ij} = (u_{i,x_j} + u_{j,x_i})/2 \qquad (4.35)$$

The constitutive relation for a plate with the plane stress problem is given as

$$\{\sigma\} = [\boldsymbol{Q}]\{\varepsilon\} \qquad (4.36)$$

The strong form of the above boundary value problem can be written as a weak formulation for the FE model using the principle of virtual displacement (or total potential energy principle), resulting in the following formulation:

$$0 = \int_{V^e} \left(\sigma_{ij}\, \delta\varepsilon_{ij}\right) dV - \oint_{V^e} f_i\, \delta u_i\ dV - \oint_{S^e} \hat{t}_i\, \delta u_i\ dS \tag{4.37}$$

where V^e denotes volume of element *e* and S^e is the boundary of Ω^e

The terms in eq. 4.37 can be rewritten with the *x*, *y*, and *z* co-ordinate system for a laminate; $\sigma_{11} = \sigma_{xx}, \sigma_{12} = \tau_{xy}, \sigma_{22} = \sigma_{yy}, \varepsilon_{11} = \varepsilon_{xx}, \varepsilon_{12} = \gamma_{xy}, \varepsilon_{22} = \varepsilon_{yy}, u_1 = u, u_2 = v,\ \ f_1 = f_x,\ f_2 = f_y,\ f_3 = f_z,$ and

$t_1 = t_x, t_2 = t_y, t_3 = t_z$ Then, eq. 4.37 becomes

$$0 = \int_z \int_{\Omega^e} \{\delta\varepsilon\}^T \{\sigma\}\ dx\, dy\, dz - \int_z \int_{\Omega^e} \begin{Bmatrix} \delta u \\ \delta v \\ \delta w \end{Bmatrix}^T \begin{Bmatrix} f_x \\ f_y \\ f_z \end{Bmatrix} dx\, dy\, dz - \int_z \oint_{\Omega^e} \begin{Bmatrix} \delta u \\ \delta v \\ \delta w \end{Bmatrix}^T \begin{Bmatrix} t_x \\ t_y \\ t_z \end{Bmatrix} dS \tag{4.38}$$

Finite element model: Let us write approximations for the primary variables *u₀*, *v₀*, *w₀*, ϕ_x, and ϕ_y in eq. 4.13 over Ω^e by using FE interpolations

$$u_0 = u_i N_i,\ v_0 = v_i N_i,\ w_0 = w_i N_i,\ \phi_x = \phi_{x_i} N_i,\ \phi_y = \phi_{y_i} N_i \tag{4.39}$$

The above variables can be written as $\{u_0 \quad v_0 \quad w_0 \quad \phi_x \quad \phi_y\}^T = [N]\{d\}$ (4.40)

where N_i denotes the shape functions of the FE and matrix [***N***] can be written as

$$[\boldsymbol{N}] = \begin{bmatrix} N_1 & N_2 & \dots & N_n & 0 & 0 & \dots & 0 \\ 0 & 0 & \dots & 0 & N_1 & N_2 & \dots & N_n \end{bmatrix}$$

where vector *d* represents the degrees of freedom and can be written as

$$\{d\} = \{u_1 \quad \dots \quad u_n \quad v_1 \quad \dots \quad v_n \quad w_0 \quad \dots \quad w_n \quad \phi_{x_1} \quad \dots \quad \phi_{x_n} \quad \phi_{y_1} \quad \dots \quad \phi_{y_n}\}^T$$

Strains can be rewritten as $\{\varepsilon\} = [B]\{d\}$ (4.41)

where $[B] = [1 \quad z]\begin{bmatrix} B^0 \\ B^1 \end{bmatrix}$ is a derivative of shape/interpolation functions *N*. The stress–strain relation for a laminate (refer to eq. 4.15) can be rewritten as

$$\{\sigma\} = [\bar{\boldsymbol{Q}}][B]\{d\} \tag{4.42}$$

Substituting eq. 4.40–4.42 in eq. 4.38, we then obtain

$$0 = \int_z \int_{\Omega^e} \{\delta d\}^T \left([B]^T [\bar{\boldsymbol{Q}}][B]\right)\{d\}\, dx\, dy\, dz - \int_z \int_{\Omega^e} \{\delta d\}^T [N]^T \{f\}\, dx\, dy\, dz - \int_z \oint_{\Omega^e} \{\delta d\}^T [N]^T \{t\}\, dS \tag{4.43}$$

$$0 = \{\delta d\}^T \left([K]\{d\} - \{f\} - \{q\}\right) \tag{4.44}$$

$$[K^e]\{d^e\} = \{f^e\} + \{q^e\} \tag{4.45}$$

where

$$[K^e] = \int_{\Omega^e} \left([B^0]^T [\boldsymbol{A}][B^0] + [B^0]^T [\boldsymbol{B}][B^1] + [B^1]^T [\boldsymbol{B}][B^0] + [B^1]^T [\boldsymbol{D}][B^1]\right) dx\, dy$$

For laminate stiffness matrices [***A***], [***B***], and [***D***], refer to eq. 4.24:

$$\{f^e\} = h_e \int_{\Omega^e} [N^e]^T \{f\}\, dx\, dy$$

$$\{q^e\} = h_e \oint_{\Omega^e} [N]^T \{t\}\, dS$$

The mechanical properties of lamina, including the elastic moduli (E_1, E_2, v_{12}, and G_{12}) and strength parameters (X_t, Y_t, and *S*), are calculated using the tensile test results for unidirectionally printed parts (layup 1, layup 3, and layup 5), as explained in section 4.2.1. These properties define the constitutive behaviour (eq. 4.12) of a single layer of a printed part.

The constitutive matrix of the material can then be used to characterize the mechanical behaviour of bidirectionally printed parts subjected to tensile and flexural loads using classical laminate theory, as described in section 4.2.2. Finally, the FE failure analysis of printed parts is carried out using the first-ply failure criterion for a laminate.

4.3 Results and Discussion

4.3.1 Mechanical properties of printed parts

The mechanical properties of the layers of printed parts are calculated, as explained earlier, using tensile test results of layup 1, layup 2, and layup 5. The elastic moduli and strength parameters of thick-layered and thin-layered parts fabricated with ABS material and ABS-SCF material are presented in Tables 4.1 and 4.2, respectively. Also, standard deviation (± SD) of corresponding values provided in tables. Strain data for the calculation of Poisson's ratio were measured using a digital image correlation setup. The strength parameters of the lamina, denoted X_t and Y_t, are the tensile strengths longitudinally and transversely, respectively, and S is the in-plane shear strength. The properties E_1, ν_{12}, and X_t were calculated from the results for layup 1, and E_2 and Y_t were obtained from the results for layup 5. The results for layup 3 were used for the calculation of G_{12} and S [152]. The elastic moduli of the layers listed in Tables 4.1 and 4.2 can define the plane constitutive matrix, which is useful in the stress analysis of the printed parts. Further, the strength parameters of the layers are useful for failure analysis of the printed parts. The difference in the results for the thick- and thin- layered laminates is due to changes in aspects of their mesostructure. The percent difference in the properties of thick-layered and thin-layered parts fabricated with ABS-SCF is much higher compared with those of parts made with ABS material. This difference means that anisotropy is higher in parts fabricated with ABS-SCF material than in parts fabricated with ABS only. The presence of SCF reinforcements in ABS material promotes anisotropy in these printed parts.

Table 4.1. Mechanical properties of the layers of printed parts with ABS material.

	Thick lamina (t_1)	Thin lamina (t_2)
E_1, MPa	1757.7 ± 29.5	2023.6 ± 96.8
E_2, MPa	1587.3 ± 28.7	1637.6 ± 129.1
G_{12}, MPa	612.6 ± 25.1	744.7 ± 13.9
ν_{12}	0.35 ± 0.05	0.32 ± 0.06
X_t, MPa	39.1 ± 0.33	39.6 ± 0.8
Y_t, MPa	21.1 ± 1.1	22.9 ± 2.9
S, MPa	16.1 ± 2.5	21.3 ± 1.4

Table 4.2. Mechanical properties of the layers of printed parts with ABS-SCF material.

	Thick lamina (t_1)	Thin lamina (t_2)
E_1, MPa	2684.2 ± 98.5	4120.4 ± 72.4
E_2, MPa	1545.7 ± 9.1	1654.3 ± 90.2
G_{12}, MPa	624.7 ± 7.1	770.0 ± 21.6
ν_{12}	0.34 ± 0.04	0.32 ± 0.05
X_t, MPa	26.1 ± 0.9	40.7 ± 0.6
Y_t, MPa	14.6 ± 0.3	14.9 ± 0.7
S, MPa	11.8 ± 0.6	14.6 ± 1.5

4.3.2 Mechanical behaviour characterization of bidirectionally printed parts subjected to tensile loads

Let us consider the tensile test results for bidirectionally printed parts with two different layup orders: cross-ply laminates (layup 6) and angle-ply laminates (layup 7). The laminates with layups 6a and 7a are thick-layered laminates, and those with layups 6b and 7b are thin-layered laminates. Tensile properties — namely tensile modulus (E_x), ultimate tensile strength (U_t), and strain to failure (ε_t) — of bidirectional laminates fabricated with ABS material are presented in Table 4.3 for cross-ply laminates and in Table 4.4 for angle-ply laminates. Similarly, the properties of parts fabricated with ABS-SCF material are presented in Table 4.5 for cross-ply laminates and in Table 4.6 for angle-ply laminates. The CLT was employed to characterize the mechanical behaviour of the bidirectionally printed parts subjected to tensile loading, as described in section 4.2.2. The tensile modulus was then calculated based on CLT and validated with experimental work.

In general, the CLT underestimates the elastic modulus of bidirectional laminates. This discrepancy is due to the fact that the CLT employs the properties listed in Tables 4.1 and 4.2, which were obtained from testing performed with unidirectional laminates. The properties of unidirectional laminates, unlike those of bidirectional laminates, are significantly influenced by the bonding strength at the interface of the layers, which consequently yields results that are inferior.

Table 4.3. Mechanical properties of cross-ply laminates fabricated with ABS and subjected to tensile loading.

	Thick lamina (t_1)	Thin lamina (t_2)
E_x, MPa	1783.9 ± 2.7	1953.8 ± 55.8
E_x, MPa (CLT)	1673.0	1832.4
U_t, MPa	29.7 ± 0.7	35.7 ± 0.6
σ_{ply}, MPa (FE)	25.2	30.3
ε_t	0.0367 ±0.0135	0.0498 ±0.0004
ε_{ply} (FE)	0.0135	0.0143

Table 4.4. Mechanical properties of angle-ply laminates fabricated with ABS and subjected to tensile loading.

	Thick lamina (t_1)	Thin lamina (t_2)
E_x, MPa	1790.7± 16.4	1911.1 ± 20.9
E_x, MPa (CLT)	1645.6	1885.2
U_t, MPa	28.0 ± 1.3	32.1 ± 0.7
σ_{ply}, MPa (FE)	25.5	31.8
ε_t	0.0435 ±0.0049	0.0592 ±0.0081
ε_{ply} (FE)	0.0143	0.0158

Table 4.5. Mechanical properties of cross-ply laminates printed with ABS-SCF under tensile loading.

	Thick lamina (t_1)	Thin lamina (t_2)
E_x, MPa	2863.9 ± 78.7	3311.0 ± 43.1
E_x, MPa (CLT)	2125.9	2909.9
U_t, MPa	23.5 ±0.5	31.3 ± 0.4
σ_ply, MPa (FE)	26.0	37.8
ε_t	0.0158 ± 0.0006	0.0214 ± 0.0006
ε_ply (FE)	0.0097	0.0096

Table 4.6. Mechanical properties of angle-ply laminates printed with ABS-SCF under tensile loading.

	Thick lamina (t_1)	Thin lamina (t_2)
E_x, MPa	2094.6 ± 43.5	2330.8 ± 53.6
E_x, MPa (CLT)	1733.3	2150.5
U_t, MPa	21.7 ± 0.5	27.7 ± 0.4
σ_{ply}, MPa (FE)	22.7	31.1
ε_t	0.0243 ± 0.0011	0.0336 ± 0.0013
ε_{ply}, (FE)	0.0105	0.0105

Further, FE simulations for tensile testing of bidirectional laminates were carried out for failure analysis, and for that the Tsai–Hill failure criterion was employed. The laminates were modeled with 2D PCOMPG finite elements in Hyperworks, and then the uniaxial tensile loads were applied at one end of the FE model, as shown in Figure 4.3. The FE model was then simulated for failure analysis. Numerical convergence of results was verified by simulating FE models of laminates meshed with different size finite elements. The final FE model has 294 quadrilateral linear finite elements. The principal stresses of the ply just after meeting the ply failure criterion are shown in Figure 4.4 for parts fabricated with ABS material and in Figure 4.5 for parts fabricated with ABS-SCF material. The reported stresses are non-averaged elemental stresses. The principal stress (σ_{ply}) for first ply failure of the laminate and the corresponding elastic ply strain (ε_{ply}) are provided in Tables 4.3 to 4.6. The discrepancy between the CLT results and experimental results is due to the properties used in CLT (provided in Tables 4.1 and 4.2), as explained earlier. The properties of the lamina listed in Tables 4.1 and 4.2 were calculated from the tensile test results for unidirectional laminates. The properties obtained from the test results for unidirectional laminates, especially those made with ABS-SCF material, are largely influenced by layer thickness, orientation of reinforcements, and bonding at the interface of the layers. Further, the bonding at the interface of the layers in bidirectional laminates is not the same as that in the unidirectional laminates. A detailed microscopic investigation of these parts can reveal the reasons for the discrepancy in the experimental and CLT-based results. We address this issue in the next chapter.

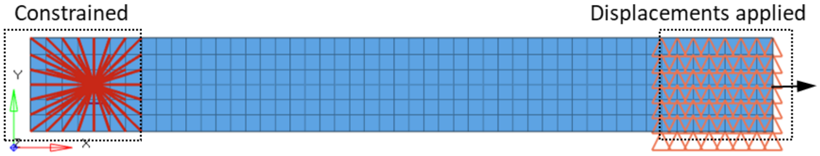

Figure 4.3. Finite element model of bidirectionally printed parts subjected to uniaxial tensile loading.

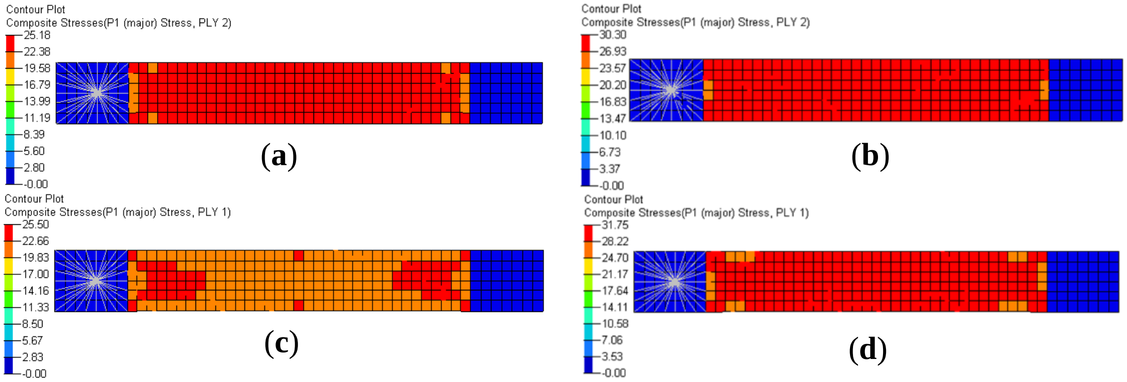

Figure 4.4. Failure stresses of a ply of bidirectional laminates fabricated with ABS and subjected to uniaxial tensile loading for: (a) thick-layered cross-ply laminate, (b) thin-layered cross-ply laminate, (c) thick-layered angle-ply laminate, and (d) thin-layered angle-ply laminate.

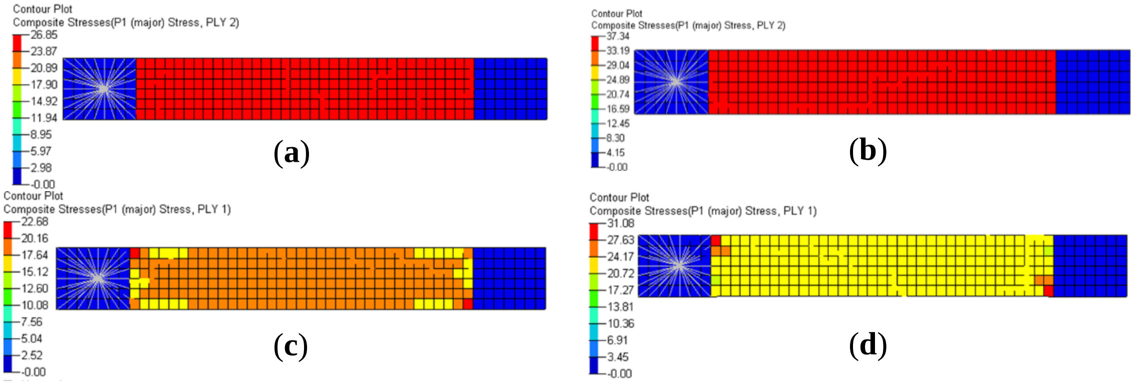

Figure 4.5. Failure stresses of a ply of bidirectional laminates fabricated with ABS-SCF and subjected to uniaxial tensile loading for: (a) thick-layered cross-ply laminate, (b) thin-layered cross-ply laminate, (c) thick-layered angle-ply laminate, and (d) thin-layered angle-ply laminate.

4.3.3 Mechanical behaviour characterization of bidirectionally printed parts subjected to flexural loads

Let us consider the three-point bending test results for cross-ply and angle-ply printed laminates. The laminates with layup 8a and layup 9a are thick-layered laminates, and those with layup 8b and layup 9b are thin-layered laminates. Flexural properties — namely flexural stiffness (E^{f}_{x}) and flexural strength (U_x^f) — of bidirectionally printed laminates are presented in Table 4.7 for ABS material and in Table 4.8 for ABS-SCF material. The CLT was employed to characterize the flexural behaviour of the bidirectional laminates, as explained in section 4.2.2. To do so, flexural stiffness of the bidirectional laminates was calculated using CLT and then validated with experimental work. The difference between the experimental and analytical results for the printed laminates indicates that the laminate theory underestimates flexural stiffness. This inaccuracy is due to the elastic moduli of the lamina from Table 4.1 and 4.2 being employed in the calculation of stiffness using CLT. The flexural stiffness (E^{f}_{x}) and flexural strength (U_x^f) of thin-layered laminate layups are higher than that of thick-layered laminates.

Table 4.7. Flexural properties of bidirectional laminates fabricated with ABS material.

	E^{f}_{x}, MPa	CLT E^{f}_{x}, MPa	U_x^f, MPa
Thick-layered laminate (t_1)			
Layup 8a	1818.1 ± 49.5	1698.2	41.4 ± 0.7
Layup 9a	1813.9 ± 17.8	1645.5	41.1 ± 1.1
Thin-layered laminate (t_2)			
Layup 8b	2382.7 ± 74.0	1875.6	50.5 ± 1.4
Layup 9b	2324.5 ± 34.3	1884.7	52.7 ± 0.8

The percent difference between the experimental and analytical (CLT) stiffness values for the isotropic laminates is smaller when compared with the percent difference for the composite laminates. This discrepancy is due to the presence of SCF reinforcements, which make the laminate stiffer. Furthermore, the flexural stiffness of composite laminates is much higher than that of laminates printed with ABS only; however, the flexural strength of the latter parts is higher. This effect is mainly due to the presence of SCF reinforcements in the composite laminates, which further promotes brittleness in the laminates. Therefore, the composite laminates experience failure earlier than laminates printed with ABS material only. To further quantify the influence of the constituents of the mesostructure of composite parts on the properties of the parts, a detailed investigation of the microstructure of parts fabricated with composite material is essential. The microstructure of composite parts is the subject of the next chapter.

Table 4.8. Flexural properties of bidirectional laminates fabricated with ABS-SCF material.

	E^f_x, MPa	CLT E^f_x, MPa	U_x^f, MPa
Thick-layered laminate (*t*1)			
Lay-up 8a	3121.6 ± 195	2294.3	38.1 ± 1.2
Lay-up 9a	2330.6 ± 32.0	1729.7	38.9 ± 0.7
Thin-layered laminate (*t*2)			
Lay-up 8b	4295.4 ± 86.6	3187.3	51.4 ± 0.9
Lay-up 9b	2864.2 ± 19.0	2144.4	47.8 ± 0.5

4.4 Conclusions

This work began by applying laminate mechanics to tensile test results to calculate the material properties of printed parts. Then, the mechanics of the printed parts were explored by characterizing their mechanical behaviour under tensile and flexural loads. The major findings of this work are as follows:

- The layers of printed parts behave like lamina reinforced with unidirectional fibers, and therefore the layers are treated as orthotropic material. Laminate mechanics were then applied to tensile test results for unidirectionally printed parts to calculate material properties — namely elastic moduli and strength parameters — of the layers of the printed parts.

- The material properties were then employed in the constitutive relation of the laminate theory to characterize the mechanical behaviour of bidirectionally printed parts subjected to tensile and flexural loads. In general, the laminate theory underestimated the material properties of bidirectionally printed parts. This is mainly due to the significant influence of bonding strength at the interface of adjacent fibers in unidirectionally printed parts, whose properties were used to estimate the material properties of a lamina in bidirectionally printed parts.
- In general, the percent difference between the experimental results and the analytically estimated results (CLT) is higher for parts fabricated with ABS-SCF than for those fabricated with ABS only. Furthermore, the difference in the properties of thick-layered and thin-layered parts fabricated with ABS-SCF is higher than the difference in the properties of parts fabricated with ABS only. It means that anisotropy in the material properties of parts fabricated with composite material (ABS-SCF) is higher than that of parts made with ABS only. The presence of more highly anisotropic properties in the composite parts could be mainly due to variation in the constituents, such as the size and orientation of SCF reinforcements and also their percentage by volume in the mesostructure of the 3D printed parts.

Chapter 5 Morphometric Analysis of Composite 3D Printed Parts

Summary: In the previous chapter, a study of the material behaviour of printed parts revealed that parts made of composite material (ABS-SCF) have greater anisotropy than those fabricated with isotropic material (ABS) only. Morphometric analysis of printed composite parts using a micro-CT scanner can uncover the reasons for this discrepancy. In this chapter, the microstructure of printed parts is characterized, and the influence of the constituents of the material on the properties of printed parts is studied.

5.1 Introduction

Microcomputed tomography (micro-CT) is a non-destructive X-ray imaging technique used to study the morphology of a material. Characterization of the microstructure of a material can be done using a micro-CT scanner, which includes quantifying a material’s microstructural features. The advantage of this technique is that, unlike other optical and scanning electron microscopes, CT scanning does not require destructive testing techniques as part of sample preparation. Moreover, other methods also require the cutting, polishing, staining, and coating of samples. This benefit of CT scanners allows us to view intricate details of the microstructure of a material in its unaltered state. In addition, higher-resolution 2D images and also 3D models can be obtained using a micro-CT scanner. 3D models of the microstructure are .stl files and can be imported using CAD tools. These 3D models are also useful in further material modeling using computer-aided engineering (CAE) tools. A micro-CT scanner is particularly useful for composite materials because of its ability to capture the heterogeneity of the material. The material properties of composites are governed by its constituents, and therefore the quantification of these constituents is important to investigate the material's behaviour.

In this work, a micro-CT scanner is used to conduct a morphometric analysis of printed composite parts. Constituents of the microstructure of thick-layered and thin-layered composite parts are quantified. Then, the scan data are used to generate a 3D model of the microstructure for both thick-layered and thin-layered composite parts. This study is the first of its kind to carry out morphometric analysis of composite 3D printed parts using a micro-CT scanner.

5.2 Micro-CT scanning

The working principle of a micro-CT scanner is shown in Figure 5.1 [154]. The object of interest is positioned to rotate while exposing it to an X-ray generator for a specific period of time. The rays penetrate the object and reach the detector, and then provide the X-ray shadow 2D images containing microstructural information about the 3D object. The images are reconstructed using an algorithm [154] to carry out image analysis and obtain the desired microstructural information.

In this study, a SKYSCAN 1272 micro-CT scanner (Bruker Corporation) was used to scan the composite parts. The scanning generates several radiographic images of the filament. Reconstruction of the images was performed using Bruker's NRecon program, which outputs grayscale images of a cross-section of the filament. The reconstruction results can be used by other Bruker programs, such as DataViewer, CT-analyser (CTAn), and CT-volume (CTVol). DataViewer is used to visualize the cross-section of the filament, CTAn to study morphometry and also build 3D models of the microstructure, and CTVol to conduct surface rendering of 3D models of the material's microstructure.

Tomography images provide information about the constituents of the composite material, such as the matrix and its reinforcements, their size and shape, and their orientation and distribution. Moreover, the scanning images are useful in the construction of the 3D geometry of the microstructure of the printed parts. Microstructural features such as reinforcements and voids — including their size, shape, orientation, and distribution in the material of the printed parts — influence the overall properties of the material. Therefore, the quantification of such parameters is important to estimate the overall properties of the printed parts.

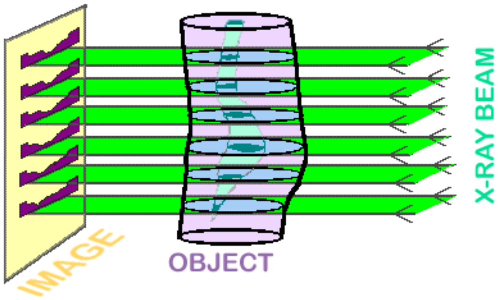

Figure 5.1. Working principle of a CT scanner [154].

5.3 Morphometric analysis using a micro-CT scanner

To characterize the microstructure of printed composite parts, the composite filament used for printing was first scanned. Then, unidirectionally printed parts consisting of two different layer thicknesses were scanned. The parameters employed for scanning are presented in Table 5.1.

Table 5.1. Parameters used for micro-CT scanning of 3D printed parts.

Parameter	Value
Filter	None
Resolution	1 μm/pixel
Image size	4904 × 3280 pixels
X-ray voltage	40 kV for filament 35 kV for thick-layered part 30 kV for thin-layered part
X-ray intensity	200 μA

Let us now consider a composite filament analyzed by micro-CT scanning. The filament (2.85 mm diameter, 20 mm length) is taken from the spool supplied by the manufacturer and then scanned. The composite filament used for scanning is shown in Figure 5.2. Morphometric analysis of the filament material reveals the size, shape, and distribution of the short carbon fiber (SCF) reinforcements and their percent volume before the parts are printed. Any variation in such data after the parts are printed can affect the material behaviour of the parts. The high-resolution (1 µm/pixel) 2D images shown in this section were obtained using DataViewer, and the 3D models were obtained using CTAn as well as CTVol.

A cross-sectional image of the filament X-ray micrographs is shown in Figure 5.3. The black areas in the radiographs are the denser material, representing carbon fiber, and the rest of the image is ABS material. The SCF reinforcements are oriented along the length of the filament. The distribution and orientation of the SCF reinforcements in the filament material is shown in Figure 5.3b. The length of CF reinforcements varies from 10 to 278 µm. The diameter of the SCF is around 7.5 µm, and its proportion in the filament material is around 10.60%. The accuracy of the results of the morphometric study was confirmed by analyzing filaments of different lengths (0.2, 0.4, and 1 mm) as well as three filament samples taken at different lengths of the filament spool.

Figure 5.2. Composite filament material used for scanning.

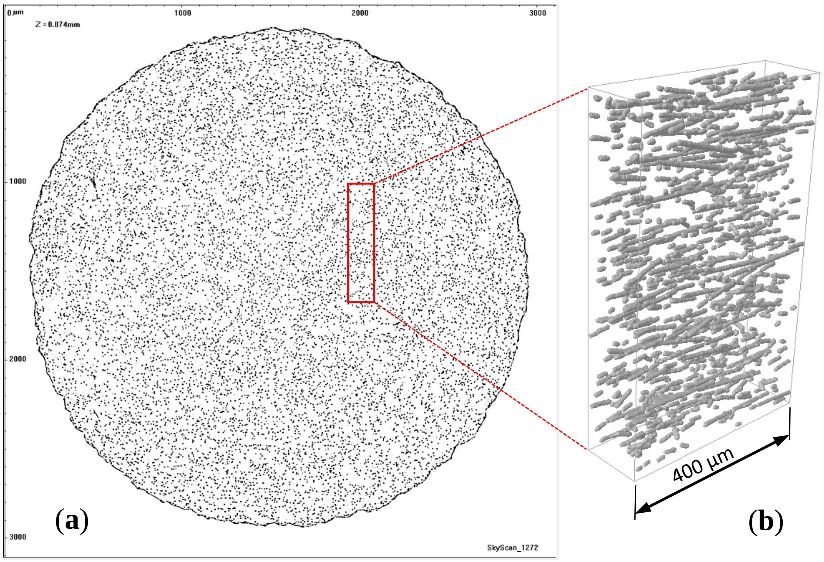

Figure 5.3. Tomographic images of a composite material filament: (a) cross-sectional image; (b) distribution and orientation of carbon fiber in the filament.

Next, let us consider a thick-layered unidirectionally printed laminate for micro-CT analysis. A small volume of the material was taken from the thick-layered unidirectionally 3D printed tensile test coupon for scanning. Then, tomographic images of the laminate were used to characterize the laminate's microstructure. The cross-section of the laminate with four layers is shown in Figure 5.4. The mesostructure of the laminate has triangular-shaped voids (black dotted lines in Fig.5.4a) between the adjacent layers. These voids are continuous and exist at the interface of all layers of the laminate; further, these voids are inherited from the printing methodology. However, the size of these voids can be minimized by increasing the overlap between the adjacent roads in a layer.

In addition, the mesostructure has irregularly shaped enclosed voids (black continuous lines in Figure 5.4a), and these are present within the fibers (extruded filament) of the laminate. The presence of these enclosed voids within the fibers is the main reason for the lower strength and stiffness of the thick-layered printed parts. Furthermore, the enclosed voids within the fibers promotes early failure of the thick-layered composite parts. The black areas in the image are

SCF material, and the gray area is ABS matrix. The orientation and distribution of the SCF reinforcements (highlighted with red continuous lines) in the thick-layered part can be seen in Figure 5.4b. Most of the SCFs are oriented in the same direction as the fiber, meaning they are aligned with the printing direction, but some SCFs are not aligned owing to the presence of enclosed voids within the fiber.

Next, individual fibers of different lengths (0.2, 0.3, 0.4 mm) were selected for morphometric analysis by CTAn. The length of SCFs is not uniform and varies from 10 to 276 µm in thick-layered parts. The length distribution of SCFs in a representative volume of material (RVE, or representative volume element model) of the microstructure of a filament (red dotted line in Figure 5.4) is shown in Figure 5.5. SCFs with a length of 10–50 µm represent around 75% of the volume, and mean length is around 40 µm. The percentage of SCFs in the selected fiber volumes is around 10.50%. A 3D model generated for the RVE is shown in Figure 5.6. Microstructural features such as size and shape of the enclosed voids, their distribution in a fiber, as well as the orientation and distribution of SCF reinforcements can be seen in Figure 5.6. The shape and size of enclosed voids are irregular. Furthermore, the distribution of enclosed voids is concentrated in the centre of the fiber, with fewer present at the interface of the fibers. This means that the interfacial bonding strength between adjacent fibers is not greatly influenced by the enclosed voids. The enclosed voids also caused a disturbance in the orientation of the SCF reinforcements in the extruded fibers. In other words, the SCF reinforcements are not well aligned with the printing direction, especially in the centre of the fiber, where the enclosed voids are more concentrated.

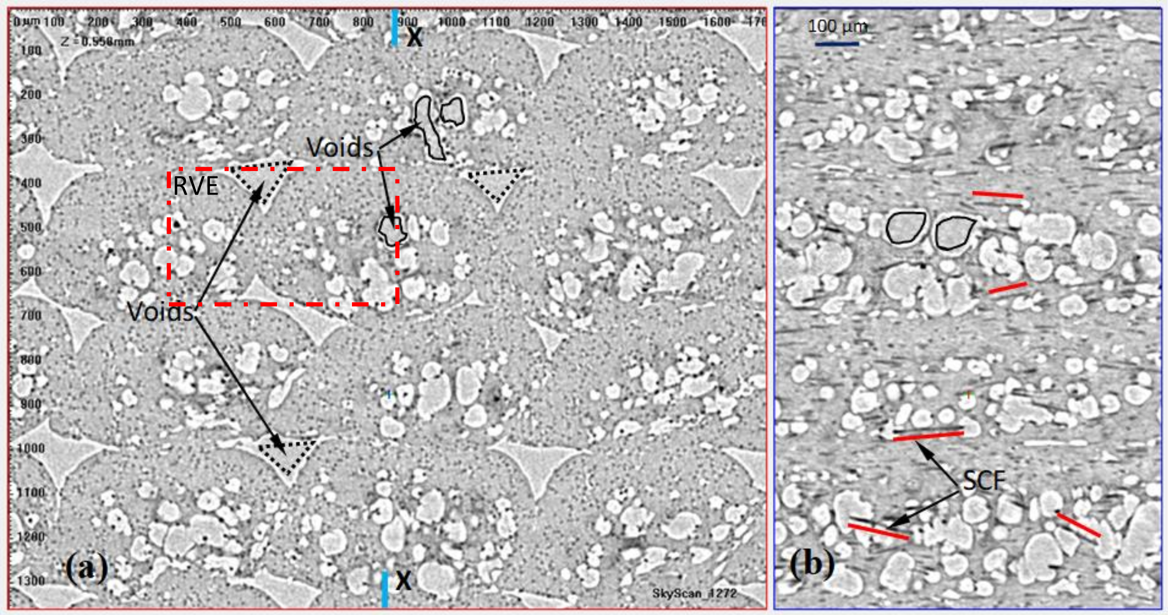

Figure 5.4. Thick-layered composite 3D printed part: (a) mesostructure; (b) cross-sectional view taken at X–X.

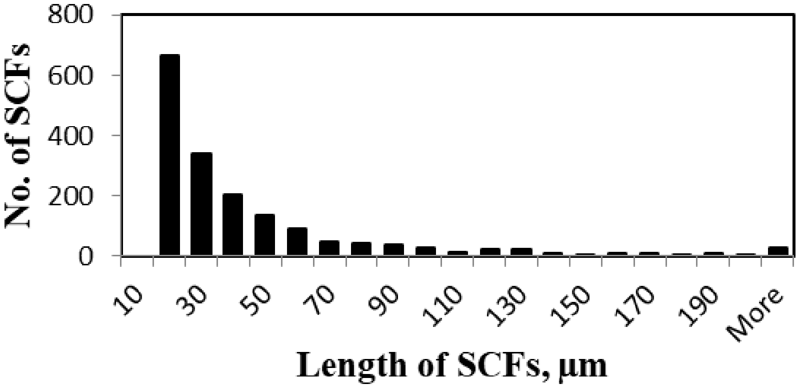

Figure 5.5. Length distribution of SCFs in an RVE volume of a thick-layered composite 3D printed part.

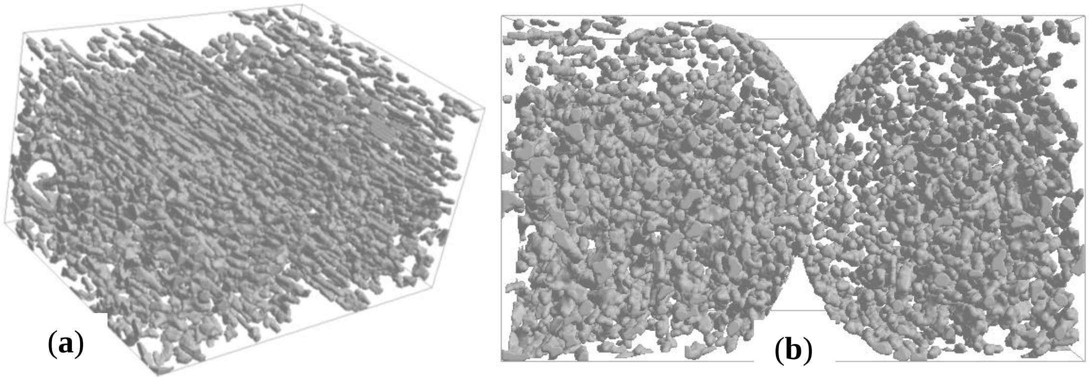

Figure 5.6. 3D models of the mesostructure of a thick-layered printed part obtained from micro-CT scanning: (a) orientation of short carbon fibers in the printed part; (b) RVE model.

Next, the same CT analysis procedure was repeated for a small volume of a thin-layered laminate. The mesostructure of the laminate obtained from the scanner is shown in Figure 5.7a. The mesostructure has voids at the interface of the layers, but the enclosed voids within the fibers are minimal compared with those present in the thick-layered laminates. The orientation and distribution of SCF reinforcements in the fiber can be seen in Figure 5.7b. The SCF reinforcements are well aligned in the printing direction when compared with their alignment in the thick-layered laminate. The length of SCF reinforcements varies from 10 to 152 µm, and the reinforcements are also spatially dispersed in the fibers. In these printed laminates, the maximum length of an SCF is approximately equal to the layer thickness, and therefore the longer SCFs above the layer thickness are subject to fracture while material is being deposited by the 3D printer. A fracture occurs because the gap between the nozzle tip and the previously deposited layer is approximately equal to the layer thickness, and therefore it cannot accommodate longer SCF reinforcements. The length of SCFs is not uniform, as shown by their length distribution in the RVE in Figure 5.8. SCFs with a length of 10–50 µm represent around 85% of the volume, and mean length is ~32 µm. The percent volume of SCF material in the selected volume of fiber is ~10.30%.

A representative volume of material (RVE; red dotted lines in Figure 5.7a) was considered for morphometric analysis by CTAn. The 3D model generated for the RVE is shown in Figure 5.9. The orientation and distribution of SCF reinforcements in the thin-layered parts can seen in Figure 5.9a. The 3D model file is an .stl file that can be imported into a commercial FE package for material modeling of the printed part using numerical homogenization.

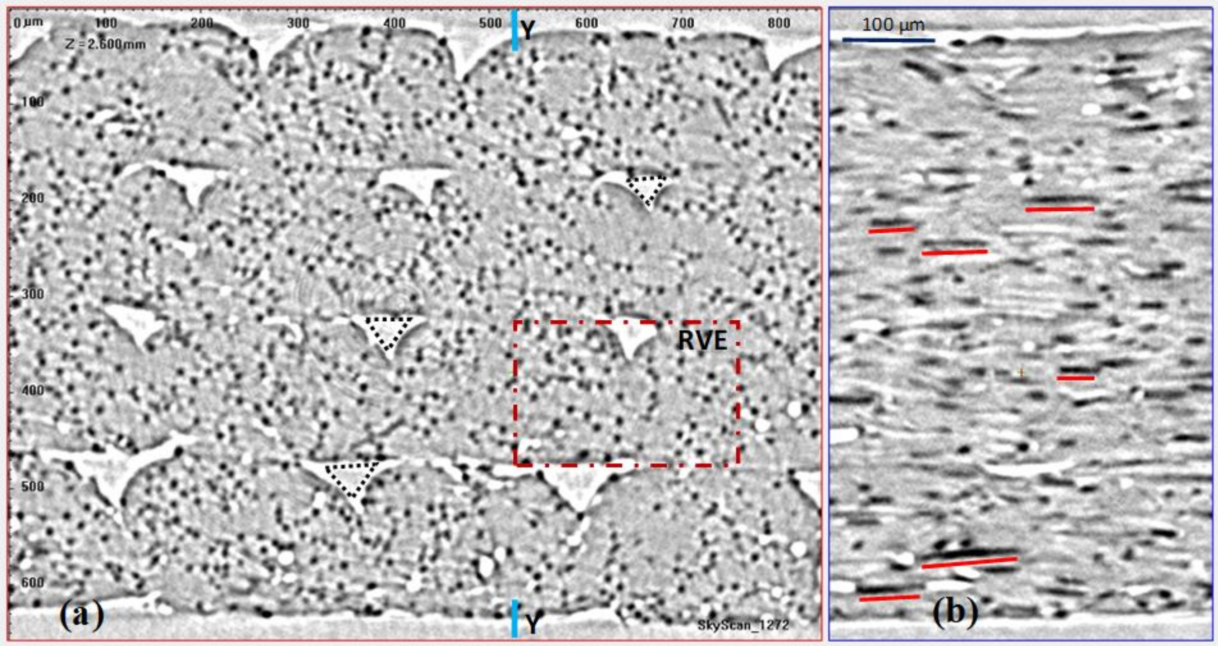

Figure 5.7. Thin-layered 3D-printed composite part: (a) mesostructure; (b) cross-sectional view taken at Y–Y.

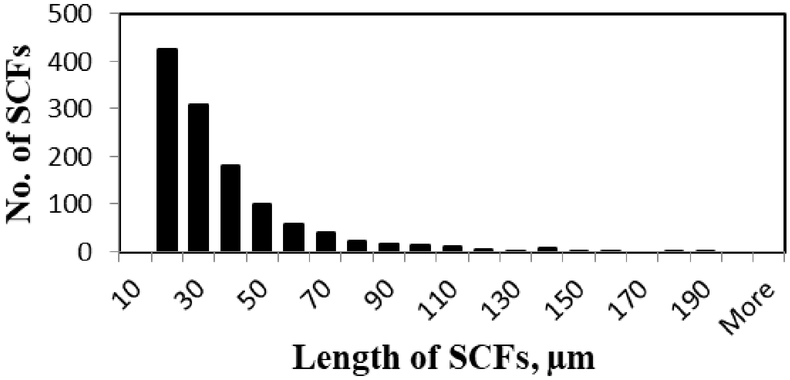

Figure 5.8. Length distribution of SCFs in an RVE volume of a thin-layered composite part.

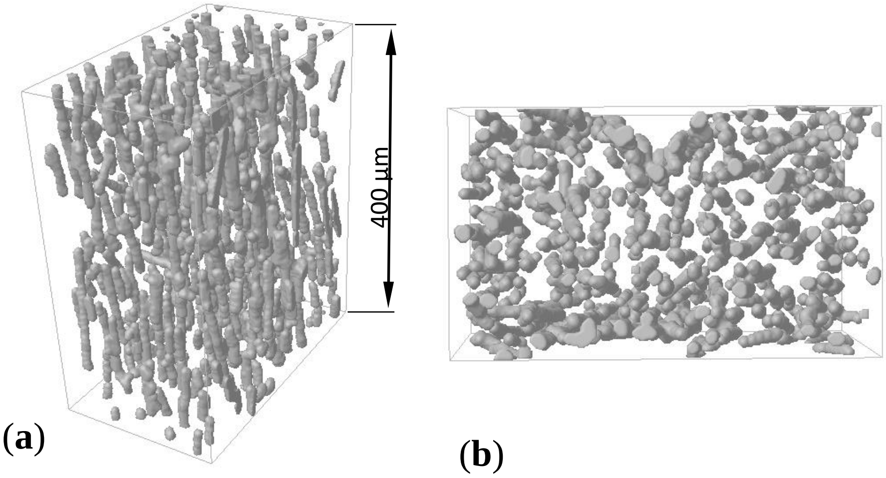

Figure 5.9. 3D models of the mesostructure of a thin-layered printed part obtained from micro-CT scanning: (a) orientation of SCFs in the printed part; (b) RVE model for homogenization.

5.4 Conclusions

In this study, a micro-CT scanner was used to carry out a morphometric analysis of the composite material of printed parts (thick-layered, thin-layered). The microstructure of the printed parts was characterized, and the influence of the constituents of the microstructure on the material's properties was revealed. The constituents of the microstructure — namely size, shape, distribution, and percentage volume of SCF reinforcements — were quantified. Further, 3D microstructural models were generated using the micro-CT scanner. The microstructural data for printed parts and 3D microstructure models obtained from the CT scanner are useful for material modeling. Finally, this study unveiled the following reasons for the difference between the material properties of thick- and thin-layered composite printed parts:

- Continuous voids are present at the interface of the layers of thick- and thin-layered printed parts. Moreover, irregularly shaped enclosed voids exist in the fibers of thick-layered parts but not that of thin-layered parts. The enclosed voids in thick-layered composites parts lead to poorer properties compared with thin-layered parts.

- The orientation of SCFs is well aligned with the printing direction (fiber orientation) in thin-layered parts, but that is not the case for thick-layered parts. The reason is that the enclosed voids in thick-layered parts cause a disturbance in the orientation of SCFs with the printing direction. Variation in the orientation of SCFs in thick-layered parts promotes anisotropy.
- The length of SCFs is not uniform in printed parts. Length varies from 10 to 276 µm in thick-layered parts and from 10 to 152 µm in thin-layered parts. The maximum length of SCFs is lower in thin-layered parts, and for that reason the lamina of thin-layered parts are subject to fracture. Furthermore, the mean length of SCFs is 40 µm in thick-layered parts and 32 µm in thin-layered parts. Moreover, the length distribution in thick-layered and thin-layered parts is not the same: the percentage of SCFs with a length of 10–50 µm is ~75% in thick-layered parts and 85% in thin-layered parts. Such differences in the length of SCFs results in anisotropic material properties. However, the SCFs are spatially dispersed and their volume percentage in ABS material is nearly the same in the printed parts.

Chapter 6 Numerical Homogenization of 3D Printed Parts

Summary: The final material properties of printed parts depend on the parts' mesostructure, which is produced through layer-by-layer deposition of material during the 3D printing process. Assessing the final properties of printed parts experimentally is tedious and time consuming. These issues can be mitigated by employing computational models instead. In this work, the homogenization computational method is used to estimate the final material properties of parts fabricated with ABS as well as ABS-SCF materials.

6.1 Introduction

Anisotropic material behaviour of printed parts is the result of variation in mesostructure, which is produced through layer-by-layer deposition of material during the 3D printing process. The mesostructure governs the overall properties of printed parts. These mesostructures consist of the size, shape, and orientation of fibers; the material (isotropic or composite) of the fibers; the shape and percent volume of reinforcements in the fibers of composite material; and the voids inherited from the printing process. Any variation in these features of the mesostructure greatly influences the final properties of printed parts. Moreover, the printing strategy can define the architecture of the parts' mesostructure for 3D printing, which means that the printing strategy also governs the material properties of printed parts. Consequently, the mesostructure of the material used in 3D printing can be tailored to obtain the desired material properties. During design and analysis of the parts for 3D printing, the final material properties and constitutive matrix must be considered to account for the final behaviour of the material. Therefore, the final constitutive matrix needs to be estimated. Experimental determination of the final properties of a 3D printed part for different mesostructures is tedious and time consuming. Multiscale methods are the more efficient alternative [155,156]. Analytical multiscale methods such as the Mori–Tanaka model are limited in their modeling of RVE (representative volume element); any such limitation can be mitigated by using computational multiscale models [157]. In this work, the computational method known as the numerical homogenization technique [158] is used to perform material modeling of 3D printed parts in order to estimate the final material properties of the parts.

When mechanical testing has been used to determine the material behaviour of printed parts [130], the results of these tests have revealed that the behaviour of the layers of the parts is orthotropic. Researchers have also attempted to experimentally characterize the mechanical behaviour of printed parts [70]. Analytical methods [49,129], such as the rule of mixtures, have been used to determine the overall material properties of the layers of 3D printed parts. However, these past efforts to define the constitutive matrix of the material of printed parts have been experimental. Moreover, the effect of the shape of voids in the mesostructure was not considered, and therefore the experimental results are applicable only to parts fabricated with isotropic material. In addition, these published works have calculated the elastic moduli for a constitutive matrix only in the plane stress case. However, computational methods for estimating the overall material properties of 3D printed parts have yet to be explored. To address this gap, computational methods are applied to material modeling — using data on the constituent properties of the microstructure of the parts — to determine the overall material properties of 3D printed parts.

This chapter describes the procedure for computationally estimating the material constitutive matrix of parts fabricated with either ABS or ABS-SCF material. To do this, the numerical homogenization technique is applied to the RVE of 3D printed parts. Then, finite element (FE) modeling of the RVE of printed parts is presented. FE modeling of the RVE of composite material employs the micro-CT data from the previous chapter. FE models of the RVE for thick-layered and thin-layered parts made with either ABS or ABS-SCF material are employed in simulations. The simulation results are then used to calculate the constitutive matrix for the layers of the 3D printed parts.

6.2 Homogenization method for 3D printed parts

Let us consider the mesostructure of 3D printed parts. The basic constituents of the mesostructure are the size, shape, and orientation of the extruded fibers; voids inherited from the printing strategy for parts fabricated with only isotropic (ABS) material; and the size, shape, and orientation of reinforcements (SCFs), as well as their percent volume, in the mesostructure of parts fabricated with composite (ABS-SCF) material. In general, for composite parts, the SCF reinforcements are transversely isotropic, and the rest of the material in the mesostructure is isotropic. The properties of a composite material depend on the constituents' material properties and their volume fraction. The mechanical performance of parts fabricated with composite material depends on many variables: the choice of constituent materials and their volume fraction, fiber orientation and ply stacking sequence, number of laminae, lamina thickness, and lamina architecture.

To produce reliable 3D printed parts, the printing strategy must be modified so that the resulting parts have the desired final properties. The desired final properties can be obtained by varying the constituents, their volume percentage, or both and by changing the printing strategy to further tailor the mesostructure. The final properties of parts fabricated with composite materials are calculated using micromechanical models based on the known properties of the material constituents. Since a printed part is considered a continuum, a small volume is taken from the mesostructure of a printed part for material modeling. This small volume is known as a representative volume element (RVE), or unit cell, and represents the periodic architecture of a printed part. The prediction of the effective stiffness matrix (elastic moduli) of the layers of the printed parts from the mesostructure of the constituents' properties is known as homogenization. There are two types of homogenization methods: analytical and numerical. Micromechanical models are also useful for damage analysis. The detailed procedure for constructing a micromechanical model is explained below.

To carry out numerical homogenization, the RVE is considered from the periodic architecture of the 3D printed part. The RVE consists of the constituents of a composite material, namely the SCFs and matrix, as well as the voids inherited during the printing process. The RVE of a printed part (Figure 6.1) is taken from a single layer of the part, as each layer is considered orthotropic material, meaning that the layers of the printed parts are treated like orthotropic laminae. The numerical homogenization technique estimates the effective constitutive matrix of the layers of the composite printed part using the properties and geometric features of the mesostructural constituents. The mechanics of homogenization for a composite material are presented below.

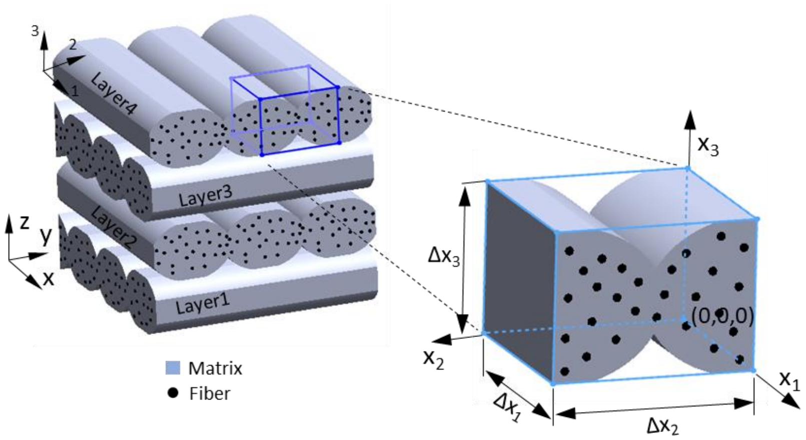

Figure 6.1. Representative volume element (RVE) of a composite 3D printed part.

In the homogenization method, the RVE is treated as a macroscopically homogeneous orthotropic material. The RVE is defined by local coordinate system x_1, x_2, and x_3, which are aligned in the direction of the length, width, and thickness, respectively, of the printed laminate. The stresses σ_{ij} and strains ε_{ij} are the local fields at a point in the RVE. In a macroscopically homogeneous RVE, the macroscopic fields — that is, the average stresses $\bar{\sigma}_{ij}$ and average strains $\bar{\varepsilon}_{ij}$ — are computed by averaging the local stresses and strains over the volume of the RVE (V_{RVE}), respectively. These are given as

$$\bar{\sigma}_{ij} = \frac{1}{V_{\mathrm{RVE}}} \int_V \sigma_{ij}(x_1, x_2, x_3)\, dV \,, \qquad \bar{\varepsilon}_{ij} = \frac{1}{V_{\mathrm{RVE}}} \int_V \varepsilon_{ij}(x_1, x_2, x_3)\, dV \qquad (6.1)$$

The average stress of a fiber and matrix are written as

$$\bar{\sigma}_{ij}^{f} = \frac{1}{V_f} \int_{V_f} \sigma_{ij}(x_1, x_2, x_3)\, dV \,, \quad \bar{\sigma}_{ij}^{m} = \frac{1}{V_m} \int_{V_m} \sigma_{ij}(x_1, x_2, x_3)\, dV \qquad (6.2)$$

Similarly, the strains are given as

$$\bar{\varepsilon}_{ij}^{f} = \frac{1}{V_f}\int_{V_f} \varepsilon_{ij}(x_1, x_2, x_3)\, dV\ , \quad \bar{\varepsilon}_{ij}^{m} = \frac{1}{V_m}\int_{V_m} \varepsilon_{ij}(x_1, x_2, x_3) dV \tag{6.3}$$

where *f* and *m* represent the fiber (SCF reinforcements) and matrix (ABS), respectively, in this model. The relationship between the fiber and matrix averages and the overall average are given as

$$\bar{\varepsilon}_{ij} = v_f \bar{\varepsilon}_{ij}^{f} + v_m \bar{\varepsilon}_{ij}^{m} \tag{6.4}$$

$$\bar{\sigma} = v_f \bar{\sigma}_{ij}^{f} + v_m \bar{\sigma}_{ij}^{m} \tag{6.5}$$

The strain energy (U^*) stored in the heterogeneous RVE of the volume V_{RVE} is

$$U^* = \frac{1}{2}\int_{V_{\mathrm{RVE}}} \sigma_{ij}\varepsilon_{ij} dV \tag{6.6}$$

The strain energy (U) calculated for the homogeneous RVE using a homogenized modulus is

$$U = \frac{1}{2}\bar{\sigma}_{ij}\bar{\varepsilon}_{ij}V_{\mathrm{RVE}} \tag{6.7}$$

The main principle of the homogenization model is to find a globally homogeneous medium equivalent to the original microscopically heterogeneous material, where the strain energy stored in both systems is approximately the same. That means

$$U^* = U \tag{6.8}$$

The elastic constitutive relation of the material for a homogenized RVE is given as

$$\{\bar{\sigma}\} = [\boldsymbol{C}]\{\bar{\varepsilon}\} \tag{6.9}$$

where [$\boldsymbol{C}$] is an effective constitutive matrix of the orthotropic material

$$[\boldsymbol{C}] = \begin{bmatrix} C_{11} & C_{12} & C_{13} & 0 & 0 & 0 \\ C_{12} & C_{22} & C_{23} & 0 & 0 & 0 \\ C_{13} & C_{23} & C_{33} & 0 & 0 & 0 \\ 0 & 0 & 0 & C_{44} & 0 & 0 \\ 0 & 0 & 0 & 0 & C_{55} & 0 \\ 0 & 0 & 0 & 0 & 0 & C_{66} \end{bmatrix} \tag{6.10}$$

and the compliance matrix [$\boldsymbol{S}$] can be written as

$$[\boldsymbol{S}] = \begin{bmatrix} 1/E_1 & -\nu_{12}/E_1 & -\nu_{13}/E_1 & 0 & 0 & 0 \\ -\nu_{12}/E_1 & 1/E_2 & -\nu_{23}/E_2 & 0 & 0 & 0 \\ -\nu_{13}/E_1 & -\nu_{23}/E_2 & 1/E_3 & 0 & 0 & 0 \\ 0 & 0 & 0 & 1/G_{23} & 0 & 0 \\ 0 & 0 & 0 & 0 & 1/G_{13} & 0 \\ 0 & 0 & 0 & 0 & 0 & 1/G_{12} \end{bmatrix} \tag{6.11}$$

where [$\boldsymbol{C}$] is equal to [$\boldsymbol{S}$]$^{-1}$, as mentioned earlier. The unknown elements in the constitutive matrix of eq. 6.9 can be calculated by solving for different load cases.

Boundary conditions: A periodic microstructure is present in the printed parts, and therefore the RVE is subject to periodic boundary conditions. These conditions represent the continuum of the physical body. The displacement field on the boundary of the RVE can be expressed as

$$u_i(x_1, x_2, x_3) = \varepsilon_{ik}^0 x_k + u_i^*(x_1, x_2, x_3) \tag{6.12}$$

where ε_{ik}^0 is a constant strain tensor. The first term on the right side of eq. 6.12 represents a linearly distributed displacement field, and the second term on the right side, $u_i^*(x_1, x_2, x_3)$, is a periodic function from one RVE to another. The periodic function *u** in eq. 6.12 is unknown, and therefore the displacement cannot be directly applied to boundaries of the RVE. These periodic boundary conditions are suitable for parallelepiped RVE models. The displacements on the pair of parallel opposite boundary surfaces is written as

$$u_i^{j+} = \varepsilon_{ik}^0 x_k^{j+} + u_i^* \tag{6.13}$$

$$u_i^{j-} = \varepsilon_{ik}^0 x_k^{j-} + u_i^* \tag{6.14}$$

where the indices *j*+ and *j*– identify a pair of two opposite parallel boundary surfaces of the RVE. The u_i^* is the same as two parallel boundaries owing to periodicity. Therefore, the difference between the above two equations is

$$u_i^{j+} - u_i^{j-} = \varepsilon_{ik}^0 (x_k^{j+} - x_k^{j-}) = \varepsilon_{ik}^0 \triangle x_k^j \tag{6.15}$$

The right side of the equation becomes constant, since $\triangle x_k^j$ are constants for each pair of the parallel boundary surfaces with specified ε_{ik}^0. Equation 6.15 is easily applicable to FE models as a nodal displacement constraint and also guarantees traction continuity along with displacement continuity for a periodic RVE model [159].

Boundary value problem: A boundary value problem is solved using the FE method. The numerical (FE) models are well suited to determining the effective stiffness of heterogeneous materials, because there is no restriction on the geometry, number of phases, or size of the phases. In FE-based micromechanical models, the prediction of effective properties is done using the RVE (i.e., unit cell). Equation 6.9 gives the relation between average stresses and strains over the RVE volume for a homogeneous composite material. From this equation, the effective stiffness tensor ***C*** is calculated. To evaluate the stiffness tensor of composite material, the RVE is subjected to six different strains ε_{ik}^{0}. The six components of strain ε_{ij}^{0} (*i*,*j* =1,…,3) are applied, enforcing the displacement boundary conditions. The strain on the boundary results in complex state of strain inside the RVE. The components of the tensor *C* are determined by solving six elastic models of an RVE subjected to the boundary conditions, where only one component of strain ε_{ij}^{0} is different from zero for each of the six problems. An FE model for an RVE subjected to unit strain is prepared for six different strain load cases for analysis. The results of the analysis enable us to compute the stress field σ_{ij} and strain field ε_{ij}, whose averages are useful for calculating the unknown values of the effective constitutive matrix, one column at time.

The strong form of the boundary value problem for linear elastostatic is written as

$\sigma_{ij,x_j} + f_i = 0$ Equilibrium equations (6.16)

$t_i = \sigma_{ij} n_j$ Traction conditions on boundary surface Γ_σ (6.17)

$u_i = \hat{u}_i$ Displacement conditions on boundary surface Γ_u (6.18)

The strain–displacement relation is given as

$$\varepsilon_{ij} = (u_{i,x_j} + u_{j,x_i})/2 \tag{6.19}$$

The constitutive relation for a fiber and matrix is given as

$$\left\{\sigma^f\right\} = \left[\boldsymbol{C}^f\right]\left\{\varepsilon^f\right\} \tag{6.20}$$

$$\left\{\sigma^m\right\} = \left[\boldsymbol{C}^m\right]\left\{\varepsilon^m\right\} \tag{6.21}$$

The strong form of the above boundary value problem can be written as a weak formulation for the FE model using the principle of virtual displacement (or total potential energy principle). We then obtain

$$0 = \int_{V^e} \left(\sigma_{ij}\, \delta\varepsilon_{ij}\right) dV - \oint_{V^e} f_i\, \delta u_i\; dV - \oint_{S^e} \hat{t}_i\, \delta u_i\; dS \tag{6.22}$$

where V^e denotes the volume of element *e* and S^e is the boundary of Ω^e. Let us now write approximations for the primary variables u_i over the Ω^e by using FE interpolations.

The variables can be written as

$$u_i = \sum_{j=1}^{n} N_i u_i^j \tag{6.23}$$

where *i* represents subscript of primary displacement variable for 1 to 3 along axis *1*, *2* and *3*. *n* denotes the number of nodes of a finite element. The primary variables in vector form can be written as

$$\{u_i\} = [N]\{d\} \tag{6.24}$$

where N_i denotes the shape functions of the FE. The matrix [***N***] for a 3D continuum finite element can be written as $[\boldsymbol{N}] = \begin{bmatrix} N_1 & N_2 & \dots & N_n & 0 & 0 & \dots & 0 & 0 & 0 & \dots & 0 \\ 0 & 0 & \dots & 0 & N_1 & N_2 & \dots & N_n & 0 & 0 & \dots & 0 \\ 0 & 0 & \dots & 0 & 0 & 0 & \dots & 0 & N_1 & N_2 & \dots & N_n \end{bmatrix}$

Vector *d*, which represents the degrees of freedom, is written as

$$\{d\} = \left\{u_1^1 \quad \dots \quad u_1^n \quad u_2^1 \quad \dots \quad u_2^n \quad u_3^1 \quad \dots \quad u_3^n\right\}^T$$

Strains can be rewritten as

$$\{\varepsilon\} = [B]\{d\} \tag{6.25}$$

The stress–strain relation of a material of an FE can be rewritten as

$$\{\sigma\} = [\boldsymbol{C}]^e [B]\{d\} \tag{6.26}$$

where superscript *e* denotes the material of an FE, fibre, or matrix.

Substituting eq. 6.24 to 6.26 in eq. 6.22, we obtain

$$0 = \int_{V^e} \{\delta d\}^T \left([B]^T [\boldsymbol{C}]^e [B]\right)\{d\}\, dV - \int_{V^e} \{\delta d\}^T [N]^T \{f\} dV - \oint_{V^e} \{\delta d\}^T [N]^T \{t\} dS \tag{6.27}$$

$$0 = \{\delta d\}^T \left([K]\{d\} - \{f\} - \{q\}\right) \tag{6.28}$$

$$\left[K^e\right]\left\{d^e\right\} = \left\{f^e\right\} + \left\{q^e\right\} \tag{6.29}$$

6.2.1 Homogenization of an RVE from a printed part with ABS material

The layers (laminae) of printed parts are treated as an orthotropic layer. Therefore, an RVE is considered from a layer of the printed parts for homogenization (Figure 6.2). Table 6.1 provides the measurements of an RVE from a layer of thick-layered printed parts as well as from a layer of thin-layered printed parts. The sizes of the RVE are obtained from microscopic images of the printed parts.

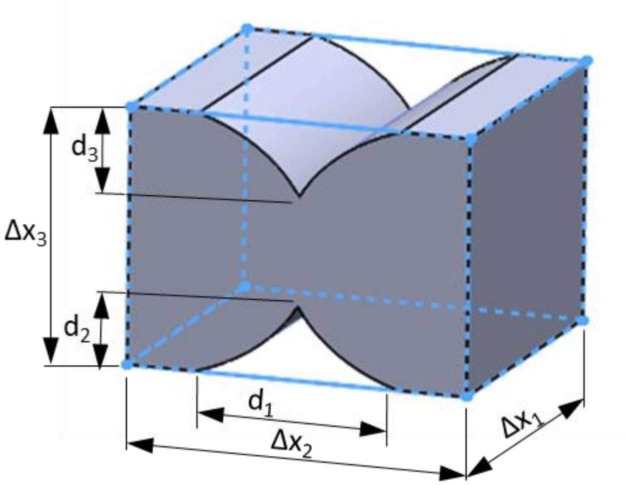

Figure 6.2. Dimensions of an RVE from the layer of a printed part.

Table 6.1. Measurements (in μm) of an RVE from thick-layered and thin-layered printed parts with ABS material.

	Δx_1	Δx_2	Δx_3	d_1	d_2	d_3
Thick-layered laminate	200	470	310	160	72	72
Thin-layered laminate	100	235	155	82	12	42

6.2.2 Homogenization of an RVE from a printed part with ABS-SCF material

In this case, the mesostructure consists of both ABS material and SCF reinforcements. Certain features of the printed part, including the size, shape, orientation, and distribution of SCF reinforcements in addition to their percent volume in the RVE, significantly influence the material properties of the printed parts. Therefore, micro-CT scanning data on the mesostructure of the composite printed parts, which was obtained from work presented in the previous chapter, is also used here. Moreover, the 3D RVE models obtained from the scanner are useful in the FE modeling of an RVE from composite parts for homogenization. The 3D models require some additional post-processing for FE modeling of an RVE for homogenization. The procedure is described here for preparing the 3D model of an RVE for homogenization.

The 3D RVE model of the mesostructure of composite parts is first imported into CAD software, after which geometry cleanup is performed (Figure 6.3a). When conducting homogenization with periodic boundary conditions, the opposite faces of the RVE should be a mirror image of one other. This periodic geometry is achieved by cutting the protruding SCF reinforcements along the boundary surfaces. Then, the SCF reinforcements are made to appear on the opposite boundary surface of the RVE (as described in [160]). The face 1–2–3–4 of the RVE has protruding SCF reinforcements (red color in Figure 6.3b); it is cut and then made to appear on the opposite face (5–6–7–8) of the RVE (Figure 6.3c). This process is repeated for faces that have protruding reinforcements. The opposite faces of the final RVE will be a mirror image of one another. The final RVE (Figure 6.3d) is used for FE meshing. The dimensions of the RVE for thick-layered and thin-layered composite printed parts are not the same, and thus the measurements are taken from the scanner. Table 6.2 provides the measurements of the RVE from thick-layered as well as thin-layered composite printed parts.

The following assumptions are made about the FE model: perfect bonding exists between adjacent fibers and also between the SCF reinforcements and ABS matrix; the fibers are uniform in shape and size in the mesostructure of the printed part; the SCF reinforcements are uniform in diameter; and finally, the SCF reinforcements are perfectly aligned in the orientation of the extruded filament, and the reinforcements are positioned without overlapping one another.

Table 6.2. Measurements (in μm) of an RVE from thick-layered and thin-layered composite printed parts with ABS-SCF material.

	Δx_1	Δx_2	Δx_3	d_1	d_2	d_3
Thick-layered laminate	80	470	310	160	72	72
Thin-layered laminate	64	235	155	82	12	42

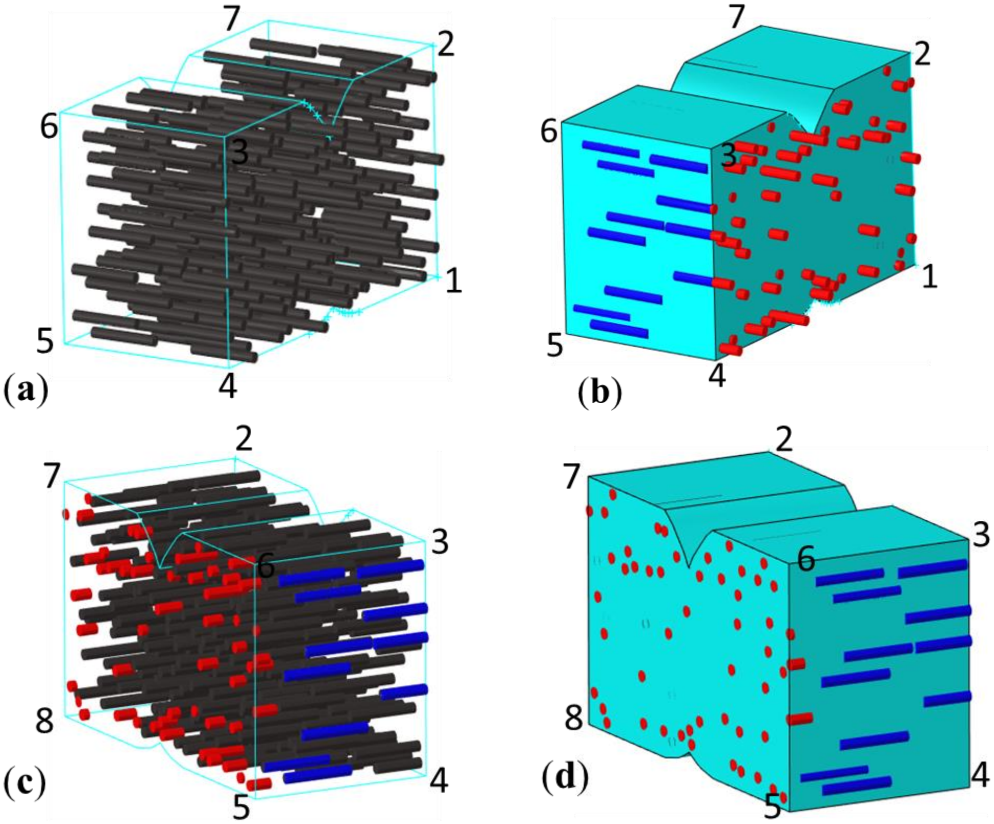

Figure 6.3. RVE of a composite part: (a) imported RVE; (b) RVE with protruding SCF reinforcements; (c) RVE with periodic geometry; (d) RVE for FE meshing.

6.3 Results and Discussion

The RVEs are modeled with linear tetrahedron FEs in Altair HyperMesh. The FE meshing is done in such a way that the nodes of elements on opposite boundary surfaces of the RVE are suitable for periodic boundary conditions. Then, homogenization is done using Altair HyperWorks commercial FE tool. The mesh dependency is avoided by modeling an RVE with smaller FEs. The RVE is subjected to six different strains, applied individually using periodic boundary conditions (eq. 6.18). That means six different load cases are prepared for six unique strains to determine the unknown elements in the constitutive matrix ***C***. The strains applied to the RVE in the present analysis are $\bar{\varepsilon}_{11}, \bar{\varepsilon}_{22}, \bar{\varepsilon}_{33}, \bar{\varepsilon}_{12}, \bar{\varepsilon}_{13}, \bar{\varepsilon}_{23} = 0.10$. The linear material properties used in the linear material modeling of the printed parts are provided in Table 6.3.

Table 6.3. Properties of materials used in FE modeling.

	Properties
Carbon fiber [161]	$E_1 = 225$ GPa, $E_2 = 15$ GPa, $G_{12} = 15$ GPa, $G_{23} = 15$ GPa, $v_{12} = 0.2$
ABS [129]	$E = 2.23$ GPa, $v = 0.34$

6.3.1 FE model of an RVE from a part fabricated with ABS material

Let us consider the RVE from the layer of a thick-layered printed part fabricated with ABS material. The FE model for this case is shown in Figure 6.4. The linear material properties of ABS material (Table 6.3) are considered in the analysis. The FE model is simulated for homogenization of the material, and unknown elements of the orthotropic constitutive matrix are calculated (see explanation of this process in section 6.2). The elements of the constitutive matrix are presented in Table 6.4.

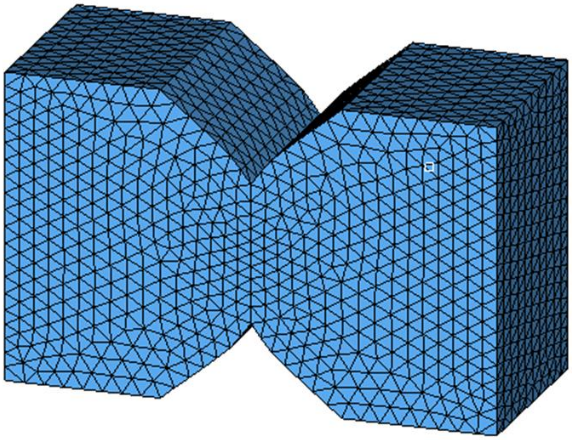

Figure 6.4. FE model of an RVE from thick-layered parts fabricated with ABS.

Table 6.4. Constitutive matrix (C_{ijkl} in MPa) for layers from thick-layered parts fabricated with ABS.

C	11	22	33	23	13	12
11	2821.5	1165.8	1176.7	0.0	0.0	0.0
22	1165.8	2355.9	1073.1	0.0	0.0	0.0
33	1176.7	1073.1	2387.8	0.0	0.0	0.0
23	0.0	0.0	0.0	644.9	0.0	0.0
13	0.0	0.0	0.0	0.0	681.7	0.0
12	0.0	0.0	0.0	0.0	0.0	679.6

The elastic moduli of the orthotropic material can be calculated from the constitutive matrix using eq. 6.11. The elastic moduli for the layers of the thick-layered printed part are provided in Table 6.5. The values obtained in the present study using numerical homogenization are compared with the elastic moduli derived from experimental work (available in the literature; Table 6.5). The elastic moduli from the experimental work can only be useful for the constitutive matrix of the plane stress case. The present numerical results are comparable to the results of the experimental work. The difference between the results of this study and the experimental results (obtained from the literature) is mainly due to the difference in the process parameters employed during the printing of the test coupons. This difference is also due to the mesostructure represented in the present FE model not being an exact replica of the mesostructure found in the test coupons from the experimental work. It is also assumed in this work that the bonding between the adjacent fibers is perfect, but in reality perfect bonding is not possible in printed coupons. However, the present analysis is an alternative to performing experimental work and provides accurate results that are highly comparable to those obtained from experimentation. Furthermore, unlike experimental work, this analysis yields all nine independent elements of the ***C*** matrix.

Six different load cases for an RVE subjected to six unique strains were simulated for analysis. The stress contours of the RVE for these different load cases are shown in Figure 6.5. The maximum stress in all deformation cases occurs at the interface of the fibers, because less material is present at the interface. Therefore, the weakest section in the mesostructure is the interface, and it is therefore more prone to the initiation of a crack during mechanical loading. In all load cases, the interface region of the fibers has higher stress. Furthermore, stress is at a maximum for the case of applied strain where $\bar{\varepsilon}_{22} \neq 0$. Therefore, debonding between the fibers can occur owing to such loading, a phenomenon that could ultimately lead to failure of the 3D printed parts.

Table 6.5. Elastic moduli (E_i and G_{ij} in MPa) for layers of thick-layered parts fabricated with ABS material.

		Experimental results				
	Homogenization (present study)	Ref. [129]	Ref. [39]	Ref. [130]	Ref. [134]	Present study
E_1	2025.1	2030.9	1972	1790	1810	1757.7
E_2	1692.6	1251.6	1762	1150	1695	1587.3
E_3	1713.3	—	—	—	—	—
G_{12}	679.6	410.0	676	808.5	617	612.6
G_{13}	681.6	—	—	—	—	—
G_{23}	644.9	—	—	—	—	—
ν_{12}	0.34	0.34	0.37	0.34	0.32	0.35
ν_{13}	0.34	—	—	—	—	—
ν_{23}	0.30	—	—	—	—	—

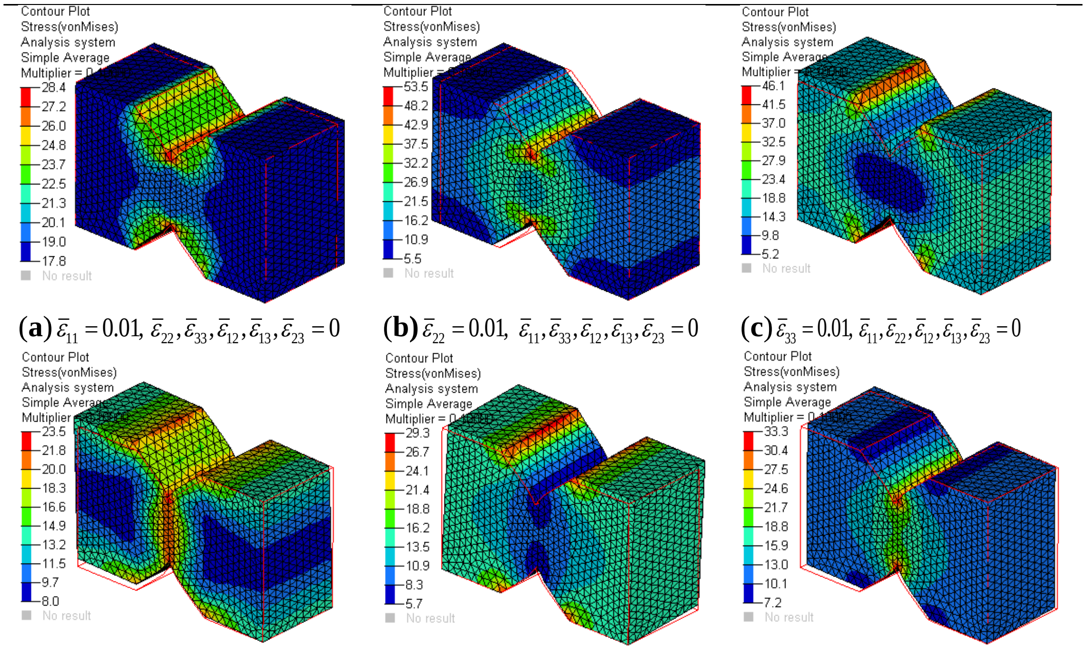

(a) $\bar{\varepsilon}_{11} = 0.01,\ \bar{\varepsilon}_{22}, \bar{\varepsilon}_{33}, \bar{\varepsilon}_{12}, \bar{\varepsilon}_{13}, \bar{\varepsilon}_{23} = 0$ **(b)** $\bar{\varepsilon}_{22} = 0.01,\ \bar{\varepsilon}_{11}, \bar{\varepsilon}_{33}, \bar{\varepsilon}_{12}, \bar{\varepsilon}_{13}, \bar{\varepsilon}_{23} = 0$ **(c)** $\bar{\varepsilon}_{33} = 0.01,\ \bar{\varepsilon}_{11}, \bar{\varepsilon}_{22}, \bar{\varepsilon}_{12}, \bar{\varepsilon}_{13}, \bar{\varepsilon}_{23} = 0$

(d) $\bar{\varepsilon}_{23} = 0.01,\ \bar{\varepsilon}_{11}, \bar{\varepsilon}_{22}, \bar{\varepsilon}_{33}, \bar{\varepsilon}_{12}, \bar{\varepsilon}_{13} = 0$ **(e)** $\bar{\varepsilon}_{13} = 0.01,\ \bar{\varepsilon}_{11}, \bar{\varepsilon}_{22}, \bar{\varepsilon}_{33}, \bar{\varepsilon}_{12}, \bar{\varepsilon}_{23} = 0$ **(f)** $\bar{\varepsilon}_{12} = 0.01,\ \bar{\varepsilon}_{11}, \bar{\varepsilon}_{22}, \bar{\varepsilon}_{33}, \bar{\varepsilon}_{13}, \bar{\varepsilon}_{23} = 0$

Figure 6.5. Stress contours for six load cases for an RVE from thick-layered parts fabricated with ABS material.

Now consider the homogenization of an RVE from thin-layered parts fabricated with ABS material. The FE model of the RVE for this case is shown in Figure 6.6. The main differences in RVEs from a thick-layered part versus a thin-layered part are the size of the fibers and the bonding area between adjacent fibers. The bonding area between adjacent fibers in the layer of a thin-layered part is larger than that of a thick-layered part, as can be seen in Figure 6.6. This minimizes void volume in an RVE and improves bonding strength between adjacent fibers in thin-layered parts, resulting in better properties. The FE model is simulated for homogenization, and the constitutive matrix is then extracted from the results of the simulation. The constitutive matrix for this case is presented in Table 6.6. Next, the elastic moduli for the thin layer are calculated, as shown in Table 6.7.

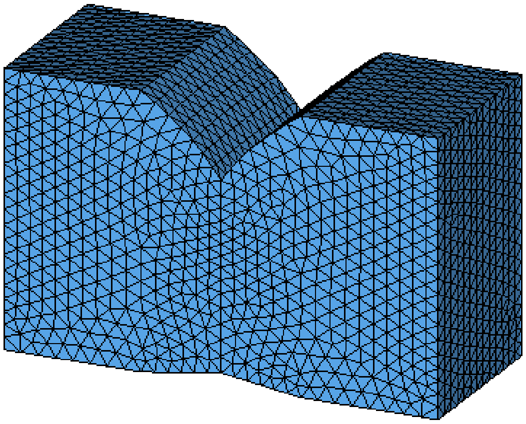

Figure 6.6. FE model of an RVE from the layer of thin-layered parts fabricated with ABS material.

Table 6.6. Constitutive matrix (C_{ijkl} in MPa) for layers of thin-layered parts fabricated with ABS material.

C	11	22	33	23	13	12
11	2989.7	1347.8	1226.8	0.0	0.0	0.0
22	1347.8	2779.8	1184.4	0.0	0.0	0.0
33	1226.8	1184.4	2423.8	0.0	0.0	0.0
23	0.0	0.0	0.0	696.6	0.0	0.0
13	0.0	0.0	0.0	0.0	699.5	0.0
12	0.0	0.0	0.0	0.0	0.0	755.7

Table 6.7. Elastic moduli (E_i and G_{ij} in MPa) for layers of thin-layered parts fabricated with ABS material.

	Numerical	Experimental
E_1	2114.4	2023.6 ± 96.8
E_2	1964.7	1637.6 ± 129.1
E_3	1737.0	—
G_{12}	755.7	744.7 ± 13.9
G_{13}	699.5	—
G_{23}	696.6	—
ν_{12}	0.34	0.34
ν_{13}	0.34	—
ν_{23}	0.33	—

The numerical results for thin-layered parts are higher than its corresponding experimental values, especially the values for direction 2. The difference between the numerical and experimental values is less than 5% overall, but for direction 2 the difference is around 16%. This is because of the perfect bonding assumption made for the FE model, which is not the case in actual printed parts. Furthermore, the numerical values for thin-layered parts are higher than those for thick-layered parts because of the differences in their RVEs, as discussed earlier.

6.3.2 FE model of an RVE from parts fabricated with ABS-SCF material

Let us now consider an RVE from thick-layered parts fabricated with ABS-SCF material. The FE RVE model is prepared according to the procedure described in section 6.2.2. The positions of the SCF reinforcements were taken from the imported file, and the SCF reinforcements were modeled with diameter of 7.5 µm and varying in length 10 to 70 µm. The percentage of SCF material in the RVE was confirmed to be ~10.60%. The dimensions of the RVE are $\Delta x_1 = 80$ µm, $\Delta x_2 = 470$ µm, and $\Delta x_3 = 310$ µm. The dimension Δx_1 is the printing direction and aligns with the orientation of the SCF reinforcements. This dimension is set to be twice the mean length of the SCF reinforcements, meaning that the RVE can accommodate at least two complete SCF reinforcements in that direction. During micro-CT scanning of the thick-layered parts, the mesostructure of the parts were found to have irregularly shaped enclosed voids within the extruded fibers. Further, the orientation of SCFs present near the enclosed voids was not perfectly aligned with the orientation of the fiber (printing direction). These features of the mesostructure were not considered in the FE model of the RVE for this case.

The final FE model of an RVE from thick-layered parts is shown in Figure 6.7. The black color represents SCFs, with their position shown in Figure 6.7a, and the blue color represents the ABS matrix. The RVE has around 2.8 million FEs and around 0.5 million nodes. FE meshing is done in such a way that the nodes of elements on opposite boundary surfaces of the RVE are suitable for periodic boundary conditions. The linear material properties (Table 6.3) are then considered for analysis. The FE RVE model is simulated for homogenization, and the simulation results are used to calculate the constitutive matrix for the layers of thick-layered parts fabricated with ABS-SCF material. The stress contours for six different deformation modes of an RVE are shown in Figure 6.8.

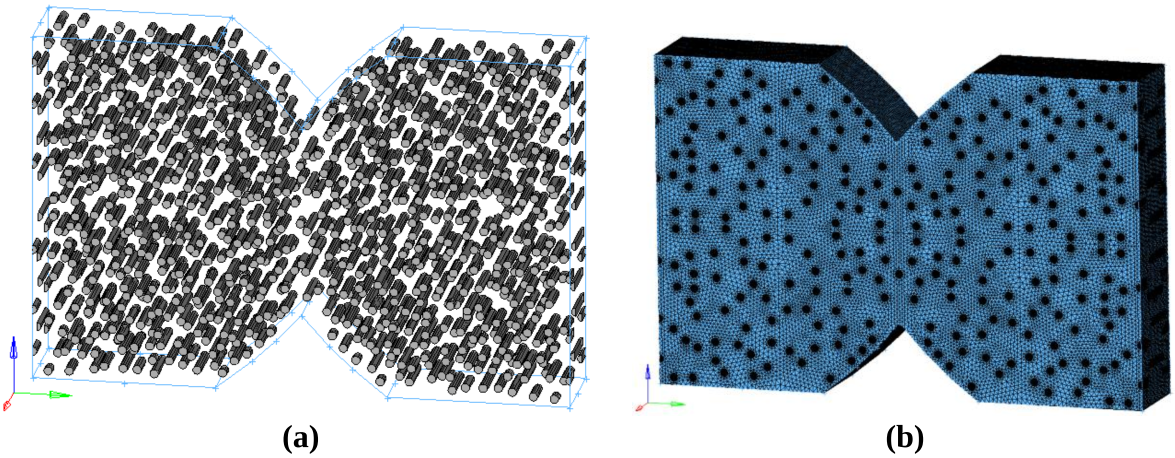

(a) **(b)**

Figure 6.7. FE model of an RVE from a thick-layered part fabricated with ABS-SCF: (a) SCFs in the RVE; (b) FE model of RVE.

The constitutive matrix for the layers of thick-layered parts fabricated with ABS-SCF material is presented in Table 6.8. The elastic moduli for layers were calculated from the constitutive matrix using eq. 6.11, and the results are presented in Table 6.9. The numerical results from the present study for thick-layered parts fabricated with ABS-SCF are comparable to the experimental results taken from chapter 4. The homogenization values are higher than the experimental values. The difference between the numerical and experimental values varies from 30% to 47%; the greatest difference is observed for direction 1 values. Ideally, the experimental values should have been close to the numerical values, but their values are almost half of the numerical values. In other words, the material properties obtained from the experiments are inferior, mainly because defects exist in the printed test coupons. Such a discrepancy in the results is caused by the presence of enclosed voids within the fibers. Moreover, misalignment of SCFs in the mesostructure of thick-layered parts is not accounted for in the FE model of an RVE. In addition, the FE model of an RVE assumes perfect bonding between SCF reinforcements and the ABS matrix, and perfect bonding between adjacent fibers. The direction 1 properties are greatly influenced by the enclosed voids that exist at the centre of the extruded fibers, leading to a greater difference between the direction 1 experimental and numerical values.

Table 6.8. Constitutive matrix of the layers of thick-layered parts fabricated with ABS-SCF material.

C	11	22	33	23	13	12
11	6033.6	1401.8	1394.9	0.0	0.1	0.0
22	1401.8	2902.0	1293.0	0.0	0.0	0.0
33	1394.9	1293.0	2917.0	0.0	0.0	0.0
12	0.0	0.0	0.0	819.5	0.0	0.0
13	0.0	0.0	0.0	0.0	905.2	0.0
23	0.0	0.0	0.0	0.0	0.0	897.3

Table 6.9. Elastic moduli (E_i and G_{ij} in MPa) of the layers of thick-layered parts fabricated with ABS-SCF material.

	Numerical	Experimental
E_1	5102.9	2684.2 ± 98.5
E_2	2214.4	1545.7 ± 9.1
E_3	2230.1	—
G_{23}	819.5	—
G_{13}	905.2	—
G_{12}	897.3	624.7 ± 7.1
v_{12}	0.34	0.34 ± 0.02
v_{13}	0.33	—
v_{23}	0.37	—

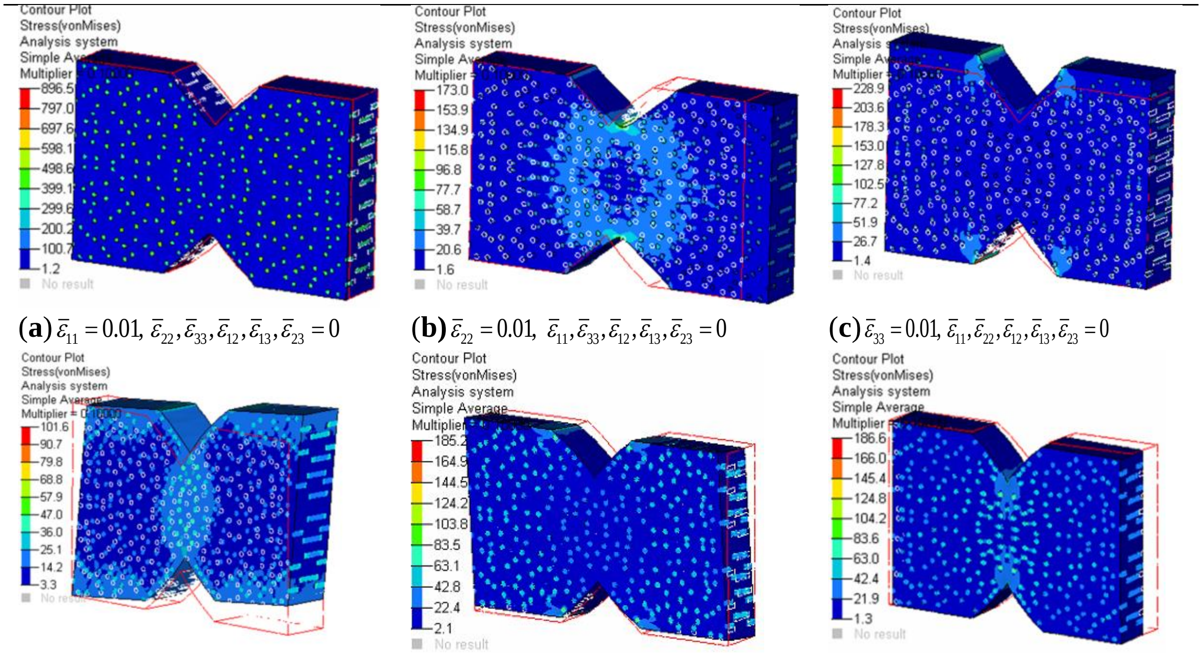

(a) $\bar{\varepsilon}_{11}=0.01,\ \bar{\varepsilon}_{22},\bar{\varepsilon}_{33},\bar{\varepsilon}_{12},\bar{\varepsilon}_{13},\bar{\varepsilon}_{23}=0$ **(b)** $\bar{\varepsilon}_{22}=0.01,\ \bar{\varepsilon}_{11},\bar{\varepsilon}_{33},\bar{\varepsilon}_{12},\bar{\varepsilon}_{13},\bar{\varepsilon}_{23}=0$ **(c)** $\bar{\varepsilon}_{33}=0.01,\ \bar{\varepsilon}_{11},\bar{\varepsilon}_{22},\bar{\varepsilon}_{12},\bar{\varepsilon}_{13},\bar{\varepsilon}_{23}=0$

(d) $\bar{\varepsilon}_{23}=0.01,\ \bar{\varepsilon}_{11},\bar{\varepsilon}_{22},\bar{\varepsilon}_{33},\bar{\varepsilon}_{12},\bar{\varepsilon}_{13}=0$ **(e)** $\bar{\varepsilon}_{13}=0.01,\ \bar{\varepsilon}_{11},\bar{\varepsilon}_{22},\bar{\varepsilon}_{33},\bar{\varepsilon}_{12},\bar{\varepsilon}_{23}=0$ **(f)** $\bar{\varepsilon}_{12}=0.01,\ \bar{\varepsilon}_{11},\bar{\varepsilon}_{22},\bar{\varepsilon}_{33},\bar{\varepsilon}_{13},\bar{\varepsilon}_{23}=0$

Figure 6.8. Stress contours for six load cases for an RVE from a thick-layered part fabricated with ABS-SCF material.

Now consider the homogenization of an RVE from the mesostructure of thin-layered parts fabricated with ABS-SCF material. The FE RVE model is prepared according to the procedure described in section 6.2.2. The data for the SCF reinforcements was obtained from the micro-CT scanner, and the SCF reinforcements were modeled with lengths of 10 to 60 µm and a diameter of 7.5 µm. The percentage of SCF material in the RVE was confirmed to be

~10.30%. The dimensions of the RVE are $\Delta x_1 = 64$ μm, $\Delta x_2 = 235$ μm, and $\Delta x_3 = 155$ μm. The dimension Δx_1 of RVE is the printing direction and aligns with the orientation of the SCF reinforcements. This dimension is set to be twice the mean length of the SCF reinforcements, meaning that the RVE can accommodate at least two complete SCF reinforcements in that direction. The fibers of thin-layered parts have smaller enclosed voids, but their percent volume is minimal compared with that of thick-layered parts, and therefore their presence can be ignored in the FE model of an RVE for this case. The RVE is then modeled with linear tetrahedron FEs in Altair HyperMesh.

The resulting FE model for an RVE is shown in Figure 6.9. The black material in the RVE is SCF material, and the blue material is ABS. The linear material properties of ABS and SCF material (Table 6.3) are then considered for analysis. The RVE has around 1 million FEs and 0.2 million nodes. FE modeling of the RVE is done in such a way that the model meets periodic boundary conditions. The FE model of the RVE is simulated for homogenization, and the constitutive matrix is then calculated using the simulation results. The constitutive matrix for the layers from thin-layered parts is presented in Table 6.10. The elastic moduli are also calculated from the constitutive matrix for the layers from thin-layered parts, and the results are presented in Table 6.11.

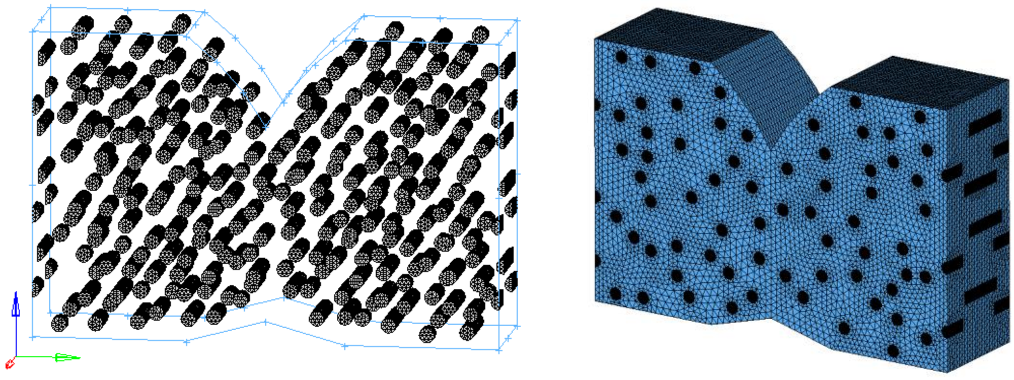
(a) (b)

Figure 6.9. FE model of an RVE from a thin-layered part fabricated with ABS-SCF: (a) SCFs in the RVE; (b) FE model of the RVE.

Table 6.10. Constitutive matrix of the layers of thin-layered parts fabricated with ABS-SCF material.

C	11	22	33	23	13	12
11	6439.2	1425.9	1355.0	0.0	0.0	0.0
22	1425.9	3054.8	1268.5	0.0	0.0	0.0
33	1355.0	1268.5	2837.8	0.0	0.0	0.0
12	0.0	0.0	0.0	823.5	0.0	0.0
13	0.0	0.0	0.0	0.0	892.9	0.0
23	0.0	0.0	0.0	0.0	0.0	930.8

Table 6.11. Elastic moduli (E_i and G_{ij} in MPa) of the layers of thin-layered parts fabricated with ABS-SCF material.

	Numerical	Experimental
E_1	5521.7	4120.4 ± 72.4
E_2	2371.7	1654.3 ± 90.2
E_3	2210.3	—
G_{23}	823.5	—
G_{13}	892.9	—
G_{12}	930.8	770.0 ± 21.6
v_{12}	0.33	0.32 ± 0.05
v_{13}	0.33	—
v_{23}	0.38	—

The difference between the numerical and experimental results for this FE model is relatively lower when compared to results of previous model. The percent difference is greater for direction 2 properties. This is contrary to the results for thick-layered parts, which have a greater difference in direction 1 properties. This discrepancy is caused by the thin-layered parts not being significantly influenced by the enclosed voids. The numerical values are higher than the experimental values because of the assumptions made in the FE model of the RVE. The perfect bonding between adjacent fibers as well as the bonding between the reinforcements and the matrix is not completely true in the actual 3D printed parts. Further, distribution of the SCF reinforcements across the cross-section of the fiber may not be uniform. Contrary to the numerical values for parts fabricated with ABS material, the values of the properties of the layers of thin-layered parts are lower than those of thick-layered parts fabricated with ABS-SCF material. This discrepancy is owing to the difference in the lengths of SCFs in the RVEs.

In summary, numerical homogenization can be used to estimate the final material properties of 3D printed parts. Further, the mesostructure, which results from the printing strategy, can be used in material modeling to estimate the final material properties. The final material properties can then be employed in the design and analysis of parts to be manufactured using 3D printing.

6.4 Conclusions

This chapter addressed the computation of the overall constitutive matrix of the material making up the layers of printed parts with either isotropic (ABS) or composite (ABS-SCF) material. The numerical homogenization method was employed to calculate the constitutive matrix from their mesostructure. The material behaviour of the layers of 3D printed parts is orthotropic. Accordingly, the orthotropic constitutive matrix for the layers is calculated and the elastic moduli for the layers are then determined. First, the numerical homogenization method was used to compute the constitutive matrix of thick-layered and thin-layered parts fabricated with ABS material based on their mesostructures. Following that, the mesostructures were used to determine the constitutive matrix of thick-layered and thin-layered parts fabricated with ABS-SCF material. A summary of the findings are as follows:

- The method used in this chapter predicted values of elastic moduli that were higher than the experimental values for the layers of parts fabricated with ABS material. This is because of the assumptions made in the FE model of the RVEs. However, the difference in the numerical and experimental values was not significant. Furthermore, maximum stress in the RVEs of parts fabricated with ABS material was at the interface of adjacent fibers in all deformation modes. This means that the interface region is the weakest part of the mesostructure and is thus more prone to the initiation of crack formation during loading.
- For composite printed parts, the estimated elastic moduli obtained using homogenization were higher than the experimental values for the layers of thick-layered parts. The experimental values were lower owing to the presence of enclosed voids inside the fibers of the layers and also misalignment of reinforcements in the fibers. Such defects were not accounted for in the FE model of the RVE for thick-layered parts. This means that the material properties of the actual thick-layered composite printed parts are inferior, and that the properties can be improved by eliminating defects that exist in the fibers of thick-layered parts. On the other hand, such defects were minimal in the mesostructure of thin-layered composite parts. Therefore, the numerical homogenization method accurately estimates the elastic moduli for thin-layered parts, yielding results that are comparable to those obtained experimentally.
- Contrary to the experimental results for composite parts, the properties of thick-layered composite parts were in the same order of thin-layered composite parts. The

experimental values for thick-layered parts are inferior because of the defects present in the parts. Furthermore, the longer SCF reinforcements in thick-layered parts resulted in better properties relative to those of thin-layered parts.

- The procedure described for linear computational material modeling of 3D printed parts fabricated with either isotropic or composite material eliminates the need for experimental work to determine the overall material properties of printed parts. This method is also useful for tailoring the material properties of printed parts.

Chapter 7 Damage Modeling of 3D Printed Parts

Summary: In this chapter, the computational models for nonlinear material modeling of 3D printed laminates made of isotropic (ABS) and composite (ABS-SCF) material are discussed. Damage modeling of printed parts subjected to mechanical loads is carried out, and the results generated are then compared with those derived from experimental work.

7.1 Introduction

The materials of printed structures fail when the load on them exceeds the design limit. Material failures vary at different scales in printed parts, especially in parts fabricated with composite material. The strength of traditional composite laminates has typically been assessed using classical first-ply failure models. However, strength- and safety-oriented design is a more difficult proposition. A more realistic approach to failure is crucial to the effective design of parts for 3D printing, since printing strategy influences the mesostructure of the parts during the printing process. Internal failures at the mesoscale lead to the ultimate failure of printed parts, and therefore material modeling at the mesoscale is needed to assess the material failure behaviour of the parts. Material modeling can be achieved using continuum multiscale damage models [162–165], a topic that has not yet been explored for 3D printed parts and is therefore addressed here.

Multiscale models [158,166,167] are useful for estimating the final properties and failure mechanism of printed parts. The micromechanical modeling of printed parts employs the mesostructure that is built during 3D printing. The main steps in micromechanical modeling are elastic homogenization, definition of the damage criteria, and damage progression law. The micromechanical model for homogenization and damage analysis of printed parts results in the following data set. First, an effective/final constitutive matrix is produced using the homogenization technique. Then, the damage limit design strain is defined — it is the strain at which the first damaged elements are found using user-defined damage initiation criteria, with the corresponding load on the part referred to as the damage limit load. Finally, the damage progression law — it is the damage development in the material of printed parts subjected to an increase in load. Damage progression reduces the load-carrying ability of the material because the global stiffness matrix components are reduced in the damaged material. The previous chapter dealt with linear material modeling, using elastic homogenization to calculate the effective constitutive matrix of the material of printed parts. This chapter focuses on nonlinear material modeling of printed parts.

In this work, 3D printed laminates subjected to uniaxial tensile loading are considered for computational damage modeling. Laminates printed with either ABS or ABS-SCF material are considered for damage analysis. First, this chapter describes the continuum damage mechanics for the materials of the printed parts. Then, an isotropic damage model with plasticity law is presented for damage analysis of the printed parts. Finally, FE models of RVEs of the printed parts are simulated for damage analysis.

7.2 Damage modeling of printed parts

In ply-level failure theories, also known as macro- or laminate failure theories, a laminate is said to have failed when the first ply fails, but this is not the case in practice. The main assumption in these failure theories is that an individual lamina is made of homogeneous, orthotropic material. Local failure within a lamina occurs before the final failure of the laminate. First-ply failure theories include the maximum stress criterion, maximum strain criterion, Tsai–Wu criterion, and Tsai–Hill criterion, among others. Ply failure criteria analyze failure in one of two ways: sudden failure and progressive failure [168–170].

In sudden ply failure theories, for a given load, the stresses in a lamina at a Gauss point are calculated using classical laminate theories, and these stresses are used to determine the maximum failure index of the laminate (the maximum failure index is obtained from the maximum stress of all Gauss points of all laminas). If the failure criterion is met in any lamina, then the laminate is said to have failed. This theory describes sudden failure without any prior intimation about failure of the laminate.

In progressive ply failure theories, for a given load, the stresses in a lamina are calculated using classical laminate theories, and the user-chosen failure criteria are verified. If a failure criterion is met, then the stiffness properties of the lamina at the failed location are degraded according to a user-defined failure degradation model. The degraded stiffness matrix is reflected in the global stiffness matrix of the laminate, and the same procedure is repeated at the same load until no further Gauss points fail (i.e., checking the equilibrium). If there are no failed Gauss points, then the model applies an increment in the load. The load is increased gradually, and the procedure is repeated until ultimate failure of the laminate occurs. The final failure is a failure of a laminate that cannot take any more load.

Although the ply failure criteria are adequate for describing failure behaviour at the macro level, they do not represent the complex failure phenomena that occur at the micro level of composite structural parts. Since the composite material of printed parts is microscopically heterogeneous, these complex failure phenomena take place at the micro level of the material. Damage occurs locally within the microstructure prior to the final failure of the laminate. These local, microscopic failures are also referred to as damage. The main damage modes in the composite materials are fiber breaking, matrix cracking, and fiber or matrix debonding. Besides these micro-level failure modes, there is also a macro failure mode in the form of delamination (opening between the layers of a laminate).

In this work, the only type of damage that printed parts fabricated with isotropic material have experienced is breakage of extruded fibers and debonding between adjacent extruded fibers. In addition, debonding between the SCF reinforcements and the matrix occurred for parts printed with composite material. Continuum damage mechanics concepts are useful for analyzing local failures in the composite materials of 3D printed parts. Continuum damage mechanics deal with damage initiation and damage accumulation in the fibers and matrix of a composite material. Damage development with an increase in load is called damage accumulation. An analysis based on these concepts reveals damage initiation and accumulation, which is useful for better understanding the behaviour of the material of printed parts for given load cases. When an applied load on a material exceeds the design load, then damage initiation and propagation occurs. Moreover, the material will start degrading progressively, which can be measured through the decrease in strength and stiffness of the material. This decrease in strength and stiffness can be measured using continuum damage mechanics concepts [171]. In this work, we consider plasticity law for accounting hardening behavior and an isotropic damage model for damage of the printed parts subjected to a load, because the base materials of the printed parts are isotropic.

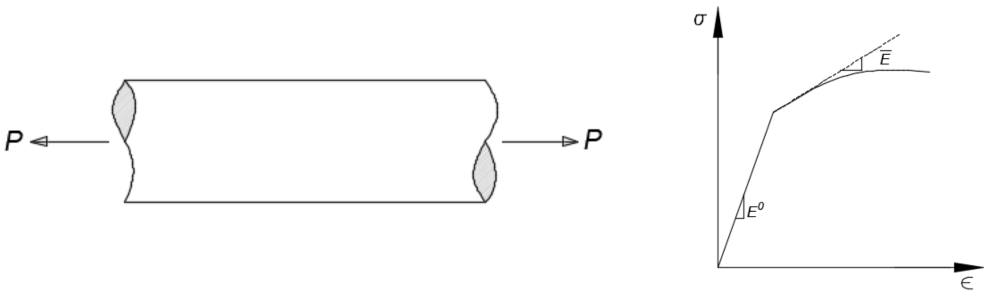

(a) **(b)**

Figure 7.1. Uniaxial loading of an isotropic material: (a) a bar subjected to tensile loading; (b) stress–strain curve of the bar.

Let us consider the classical uniaxial damage theory to introduce basic concepts and to understand the basis of damage mechanics. Consider a bar made of isotropic material with property E^0 and subjected to tensile load P, as shown in Figure 7.1. The material is damaged to a certain degree, resulting in the degradation of the material property from E^0 to $\bar{E}$. The nominal stress, σ, of that bar is defined as the force per unit initial area of the cross-section of the bar. The constitutive relation that defines this scenario in damage configuration is given as

$$\sigma = \bar{E}\varepsilon \tag{7.1}$$

The damaged part can be represented as an undamaged part using an effective stress–strain relation. The effective stress, $\bar{\sigma}$, is defined as the force per unit effective area, and the constitutive relation in nominal (initial) configuration is given as

$$\bar{\sigma} = E^0\bar{\varepsilon} \tag{7.2}$$

The nominal stress invokes the Cauchy equations of equilibrium on the macroscopic level, while the effective stress is the “actual” stress acting in the material’s microstructure. The principle of strain equivalence states that the strain $\bar{\varepsilon}$ in the undamaged part is equal to the strain ε in the damaged part, i.e., $\bar{\varepsilon} = \varepsilon$, using this that the relation between nominal stress and the stress in damaged configuration is given as

$$\bar{\sigma} = \frac{E^0}{\bar{E}} \sigma \tag{7.3}$$

$$\bar{\sigma} = \sigma / (1 - d) \tag{7.4}$$

where *d* is the damage variable, given as

$$d = 1 - \frac{\bar{E}}{E^0} \tag{7.5}$$

Then, the constitutive law for the nominal stress, σ , can be written as

$$\sigma = (1 - d) E^0 \varepsilon \tag{7.6}$$

The damage evolution for the uniaxial model can be characterized by the damage variable, which in turn is a function of the applied strain

$$d = g(\varepsilon) \ , \quad 0 \le d \le 1 \tag{7.7}$$

The evolution law function, *g*, affects the shape of the stress–strain diagram, which can be identified from a uniaxial test. To account for the previous state of the material, let us introduce the internal variable *r*, which characterizes the maximum strain level reached in the previous history of the material up to a given time *t*

$$r(t) = \max \left\{ r_0, \max_{\tau \le t} \varepsilon(\tau) \right\} \tag{7.8}$$

Equation 7.8 implies that $r(t) \ge r_0$, where r_0 is the damage threshold and a material parameter that represents the value of strain at which damage starts. Time, *t*, is a monotonically increasing parameter governing the loading process. The damage evolution law, eq. 7.7, is then rewritten in the form

$$d = g(r) \quad \text{with} \begin{cases} g(r) = 0 \;\; if \;\; r = r_0 \\ 0 < g(r) \leq 1 \;\; if \;\; r > r_0 \end{cases} \tag{7.9}$$

Equation 7.9 is not only valid for monotonic loading (*0–1*) but also during unloading and reloading (*1–2*) (see Figure 7.2). Further, this damage evolution law also considers the loading history, which is reflected by including the value of the internal state variable *r*.

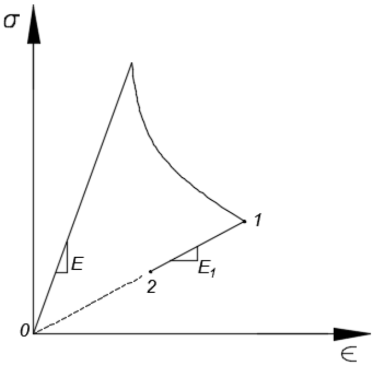

Figure 7.2. Stress–strain graph for uniaxial damage model through a non-monotonic loading process.

The constitutive law (eq. 7.6) can be rewritten in the form

$$\sigma = E_{\sec}\varepsilon \tag{7.10}$$

where $E_{\sec}$ is the damaged modulus of elasticity

$$E_{\sec} = (1-d)E^0 \tag{7.11}$$

Furthermore, instead of defining the variable *r*, as was done in eq. 7.8, we can introduce a loading function f as follows

$$f(\varepsilon, r) = \varepsilon - r \tag{7.12}$$

To ensure that the damage accumulation can take place only on the damage surface, let us postulate the loading–unloading conditions in Kuhn–Tuker form as

$$f \le 0; \quad \dot{r} \ge 0; \quad \dot{r}f = 0 \tag{7.13}$$

In the above equation, the first condition indicates that *r* can never be smaller than ε, while the second condition means that *r* cannot decrease. The final condition ensures that *r* can grow only if the current values of ε and *r* are equal.

The previous series of equations is useful for the damage modeling of material. At this point, we can summarize the three main components of the uniaxial damage theory as

- The stress–strain relation $\sigma = E_{\sec}\varepsilon$, with $E_{\sec} = (1-d)E^0$. This provides the material's stiffness degradation with damage variable *d*.
- The damage evolution law $d = g(r)$ with $\begin{cases} g(r) = 0 \ \ if \ \ r = r_0 \\ 0 < g(r) \le 1 \ \ if \ \ r > r_0 \end{cases}$. The evolution law defines the rate of damage in the material.
- The damage criterion, which defines the state of the material, and consists of
    - The loading function, $f(\varepsilon, r) = \varepsilon - r$, which specifies the elastic domain $\varepsilon_r = \{\varepsilon \mid f(\varepsilon, r) < 0\}$, the set of states for which damage does not grow.
    - The loading–unloading conditions, $f \le 0$; $\dot{r} \ge 0$; $\dot{r}f = 0$.

7.2.1 Isotropic damage and plasticity

Now let us see the extension of the uniaxial isotropic damage model to the multiaxial stress state along with plasticity law. In the isotropic damage model, stiffness degradation is isotropic. This means that the stiffness moduli corresponding to different directions decrease proportionally, independently of the direction of loading.

The damage constitutive tensor is expressed as

$$\mathbf{C}_{\sec} = (1-d)\mathbf{C} \tag{7.14}$$

where **C** is the elastic constitutive tensor of the material and *d* is the damage variable. $\mathbf{C}_{\sec}$ is the secant constitutive tensor that relates the total strain ε to the total stress σ

$$\boldsymbol{\sigma} = \mathbf{C}_{\sec} : \boldsymbol{\varepsilon} = (1-d)\mathbf{C} : (\boldsymbol{\varepsilon} - \boldsymbol{\varepsilon}^{p}) \tag{7.15}$$

Equation 7.15 can also be written in the form

$$\boldsymbol{\sigma} = (1-d)\bar{\boldsymbol{\sigma}} \tag{7.16}$$

Equation 7.16 is the multidimensional generalization of eq. 7.4, where $\bar{\sigma}$ is the effective stress tensor, defined as follows

$$\bar{\boldsymbol{\sigma}} = \mathbf{C} : \boldsymbol{\varepsilon} \tag{7.17}$$

Damage criterion: Similar to the uniaxial case, let us consider a loading function, *f*, specifying the elastic domain and the states at which damage grows. The loading function now depends on the strain tensor ε and the variable *r* controlling the evolution of the elastic domain. The term $f(\varepsilon,r) < 0$ represents the elastic domain and is below the current damage threshold. Damage can grow only if the current state reaches the boundary of the elastic domain, i.e. when $f(\varepsilon,r) = 0$. Essentially, we can postulate the damage criterion for a multiaxial isotropic damage model with the loading function

$$f(\varepsilon,r) = \varepsilon_{\mathrm{eq}}(\varepsilon) - r \tag{7.18}$$

and the loading–unloading conditions

$$f \le 0; \quad \dot{r} \ge 0; \quad \dot{r}f = 0 \tag{7.19}$$

where $\varepsilon_{\mathrm{eq}}$ is equivalent strain, i.e. a scalar measure of the strain level, and r is the largest value of the equivalent strain calculated in the previous deformation history of the material up to its current state. In this regard, the equation can now be generalized as follows

$$r(t) = \max\left\{ r_0, \max_{\tau \le t} \varepsilon_{\mathrm{eq}}(\tau) \right\} \tag{7.20}$$

In this case, the equivalent strain is as follows

$$\varepsilon_{eq} = \sqrt{\sum_{i=1}^{3} \langle \varepsilon_i \rangle^3} \tag{7.21}$$

where ε_i for i =1 to 3 are the principal strains.

Plasticity hardening law: The plasticity law for rate independent behavior during the deformation is considered. It is assumed that the material is non-viscous and follows isothermal plastic behavior. The rate independent hardening behavior can be seen in Figure 7.3a. The evolution law can be written as

$$h(\alpha) = (\bar{K}_\alpha - \bar{K}_0)\left[1 - \exp(-\delta\alpha)\right] + \bar{H}'\alpha \tag{7.22}$$

For isotropic hardening that the function can be written as

$$K(\alpha) = \bar{K}_0 + h(\alpha) \tag{7.23}$$

Damage evolution law: There are several damage governing laws, $g(r)$, that can be effectively used to model damage growth in the materials. In this work, we employed the bilinear law for evolution of damage and Figure 7.3b presents the bilinear law. The damage variable (d) for these cases is given as

$$
d = g(r) = \begin{cases} 0 & r \le \varepsilon^0 \\ \left(\dfrac{a}{r} + b\right).d_{\max} & \varepsilon^0 \le r \le \varepsilon^1 \\ d_{\max} & r > \varepsilon^1 \end{cases} \tag{7.24}
$$

where $a = \dfrac{1}{1/\varepsilon^1 - 1/\varepsilon^0}$; $b = -a/\varepsilon^0$;

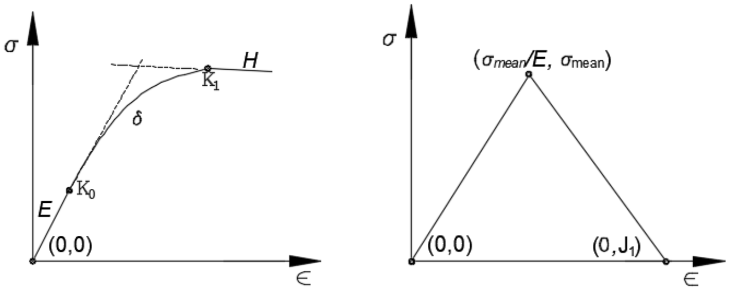

(a) **(b)**

Figure 7.3. Nonlinear material models (a) hardening model and (b) bilinear damage law.

7.3 Results and Discussion

The nonlinear material behaviour of parts fabricated with either isotropic (ABS) or composite (ABS-SCF) material was characterized using an isotropic damage and plasticity model. The damage analysis was carried out using HyperWorks, a commercial FE software. The FE models of RVEs of printed parts that were constructed in chapter 6 were employed in this section for nonlinear material modeling. However, experimental characterization revealed that it was the ABS material only that was responsible for the nonlinearity. Therefore, in this work, ABS material alone is accounted for nonlinearity in the damage modeling. The material (CF) of the reinforcements is considered to remain elastic during deformation.

Two different sets of nonlinear data were used for damage modeling of printed parts. In first case, nonlinear properties of bulk ABS material were considered for the damage modeling of RVE models and the results of damage model based on such properties are denoted with

‘DM–Bulk’. In second case, nonlinear data from the tensile test results of unidirectional laminates (UDL) was employed in the damage modeling to capture the actual nonlinear behavior of the printed parts. The results with this damage model are represented with ‘DM–UDL’. The nonlinear data of the unidirectional laminate layup-1 and layup-5 data were used for the extruded fibers and the interface of the adjacent fibers, respectively in the RVE models. For instance, nonlinear properties for damage modeling of thick-layered parts printed with ABS material are taken from the test data of thick-layered layup-1 and layup-5 laminates of the same material. This allows to accurately replicate the nonlinear behavior of the extruded fibers and the interface of the fibers in the damage modeling of the printed parts. Finite element RVE models for above two different cases are shown in Figure 7.4 for the thick-layered parts printed with ABS material. The nonlinear parameters were obtained from stress-strain data of bulk ABS material and are listed in Table 7.1. Also, the material properties of the SCF reinforcements are provided in Table 7.2.

Table 7.1. Material properties of bulk ABS for damage modeling.

Property	Value
E, in MPa	2230
v	0.34
σ_Y , in MPa	30
σ_U , in MPa	40
δ	200
H	-100
ε_{p0}	0.07
ε_{p1}	0.10
σ_{mean}	36
J_1	0.10

Table 7.2. Material properties of SCF reinforcements for damage modeling.

Property	Value
E_1, in GPa	225
E_2, in GPa	15
G_{12}, in GPa	15
G_{23}, in GPa	7
ν_{12}	0.02

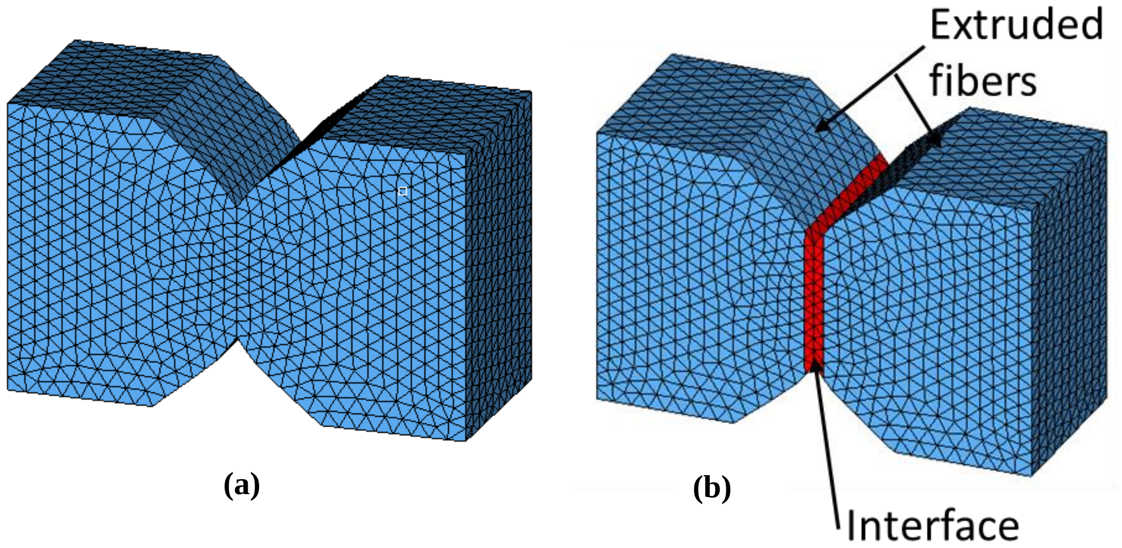

Figure 7.4. RVE models for thick-layered parts printed with ABS material, (a) FE model for damage modeling with bulk ABS material (DM-Bulk), (b) FE model for damage modeling with unidirectional laminate test data (DM-UDL).

Bidirectionally printed parts (layup 6 and layup 7) subjected to tensile loading were considered for damage modeling. Laminate layup 6 represents a cross-ply laminate, and layup 7 an angle-ply laminate. Thick-layered and thin-layered parts fabricated with ABS material were considered first. Next, thick-layered and thin-layered parts fabricated with composite material were simulated for damage modeling. The damage analysis of the printed parts follows the work flow of damage modeling described earlier.

Let us now consider the damage modeling of bidirectionally printed layup 6 and layup 7 made with ABS material. The stress–strain curve obtained from damage modeling is compared with experimental work. Figure 7.5 compares these two sets of results for a thick-layered part and a thin-layered part, respectively. Furthermore, the damage analysis results are compared with the results of the Tsai–Hill failure criterion and also with the experimental values (taken from chapter 4), as shown in Table 7.3.

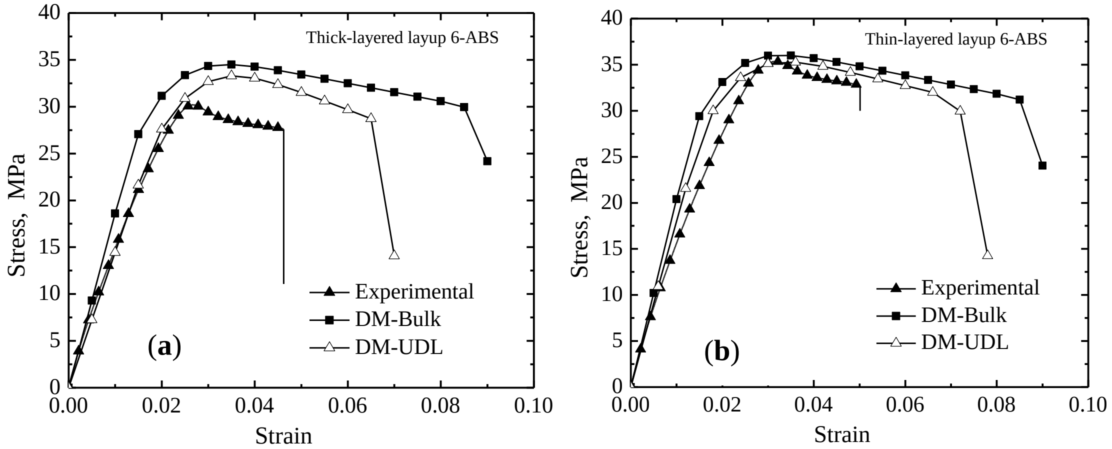

Figure 7.5. Stress–strain relation for cross-ply laminate (layup 6) fabricated with ABS material for a (a) thick-layered laminate and (b) thin-layered laminate.

Table 7.3. Comparison of damage modeling and Tsai–Hill failure criteria results with experimental work for laminate layup 6 fabricated with ABS material and subjected to uniaxial tensile loading.

	Experimental	CLT and Tsai–Hill	Multiscale modeling	
			DM-Bulk	DM-UDL
Thick-layered laminate				
E_x, in MPa	1783.9 ± 2.7	1673.0	1865.7	1751.1
U_t, in MPa	29.7 ± 0.7	25.2	34.5	33.3
ε_t	0.0367 ± 0.0135	0.0135	0.09	0.07
Thin-layered laminate				
E_x, in MPa	1953.8± 55.8	1832.4	2040.8	1922.3
U_t, in MPa	35.7 ± 0.6	30.3	37.7	36.0
ε_t	0.0498 ±0.0004	0.0143	0.09	0.075

The stress–strain curves obtained from damage modeling of thick-layered and thin-layered laminate layup 7 are shown in Figures 7.6a and 7.6b, respectively. These stress–strain curves are compared with those obtained from experimental work. Also, the properties of laminate layup 7, namely stiffness (E_x), strength (U_t), and strain to failure (ε_t), were extracted from the stress–strain curve obtained using damage modeling and then compared with both experimental values and also laminate theory results, as shown in Table 7.4.

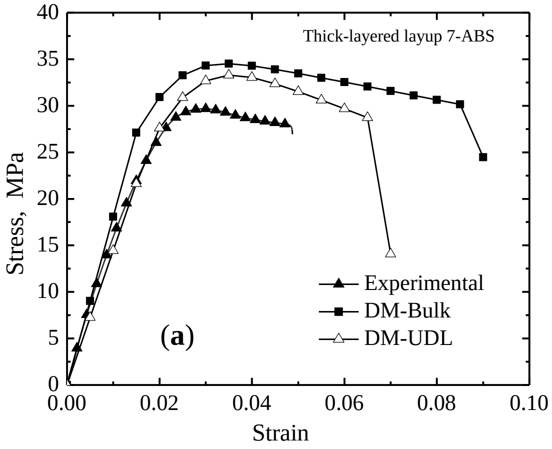

Figure 7.6. Stress–strain relation for angle-ply laminate (layup 7) fabricated with ABS material for a (a) thick-layered laminate and (b) thin-layered laminate.

Table 7.4. Comparison of damage modeling and Tsai–Hill failure criteria results with experimental work for laminate layup 7 fabricated with ABS material and subjected to uniaxial tensile loading.

	Experimental	CLT and Tsai–Hill	Multiscale modeling	
			DM-Bulk	DM-UDL
Thick-layered laminate				
E_x, in MPa	1728.7 ± 16.4	1645.6	1810.2	1720.2
U_t, in MPa	28.0 ± 1.3	25.5	35.4	33.8
ε_t	0.0435 ±0.0049	0.0143	0.09	0.069
Thin-layered laminate				
E_x, in MPa	1911.1 ± 20.9	1885.2	2018.1	1901.1
U_t, in MPa	32.1 ± 0.7	31.8	37.7	36.0
ε_t	0.0592 ±0.0081	0.0158	0.09	0.075

The damage modeling simulation values are comparable to the values obtained from experimental work for parts printed with ABS material. The results based on DM-Bulk are higher than the experimental. However, the actual nonlinear behavior of the printed parts is predicted by DM-UDL, which used tensile test data of unidirectional laminates. The phenomenological failure theory, that is first-ply failure theory (Tsai–Hill failure criterion), under predicted the values compared with the results of damage modeling. As mentioned earlier, the failure criterion employs properties that were calculated from the results of uniaxial tensile laminates. The damage model predicted higher values, because of the assumptions made in the FE models of the RVEs. Moreover, damage modeling employs the results of numerical homogenization as well as the nonlinear properties of the virgin material. Therefore, the values resulting from damage modeling are higher than those from the Tsai–Hill failure criterion and experimental work.

Now let us consider the damage modeling of bidirectional laminates fabricated with ABS-SCF material. Tensile test results of ABS-SCF parts revealed that the nonlinearity in these parts is attributable by ABS material only. Therefore, it is the nonlinear behaviour of ABS alone that is considered for damage modeling, while the material behaviour of the SCF reinforcements remains linear during deformation. Further, the previously discussed damage models were employed for the ABS-SCF printed parts. In addition, the FE models of the RVEs for thick-layered and thin-layered parts fabricated with ABS-SCF material were considered here for damage modeling. The FE models of the RVEs were simulated for damage modeling. The stress–strain curves based on the damage modeling of laminate layup 6 were then compared with the results of experimental work (Figure 7.7). Further, the damage model estimated properties of laminate layup 6 were compared with the results of both the experimental work and laminate theory results, as shown in Table 7.5. Similarly, the results of the damage analysis of laminate layup 7 are presented in Figure 7.8 and Table 7.6.

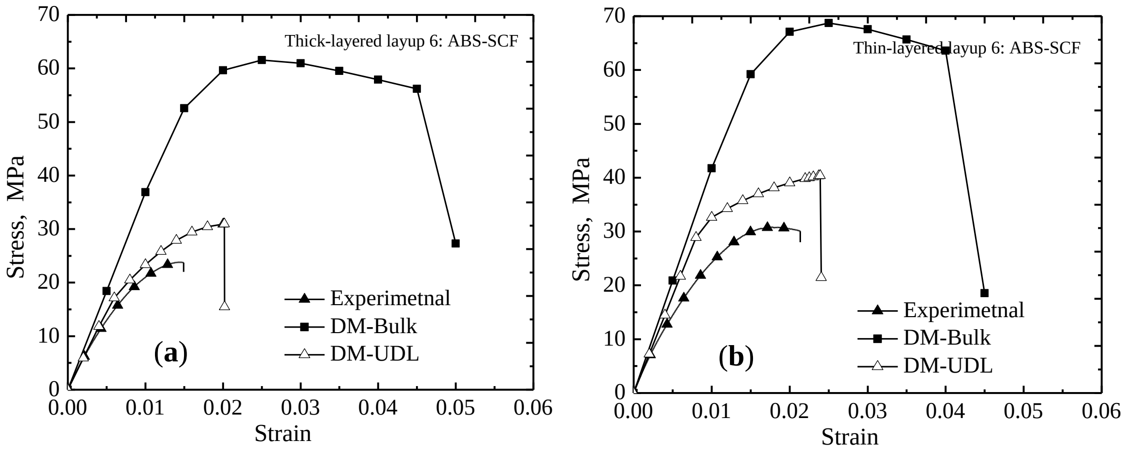

Figure 7.7. Stress–strain relation for laminate (layup 6) fabricated with ABS-SCF material for a (a) thick-layered laminate and (b) thin-layered laminate.

Table 7.5. Comparison of damage modeling and Tsai–Hill failure criteria results with experimental work for laminate layup 6 fabricated with ABS-SCF material and subjected to uniaxial tensile loading.

	Experimental	CLT and Tsai–Hill	Multiscale modeling	
			DM-Bulk	DM-UDL
Thick-layered laminate				
E_x, in MPa	2863.9 ± 78.7	2125.9	3704.2	2974.5
U_t, in MPa	23.5 ± 0.5	26.0	61.6	33.6
ε_t	0.0158 ±0.0006	0.0097	0.05	0.022
Thin-layered laminate				
E_x, in MPa	3311.0 ± 43.1	2909.9	4189.5	4101.5
U_t, in MPa	31.3 ± 0.4	37.8	68.7	40.4
ε_t	0.0214 ±0.0006	0.0096	0.045	0.024

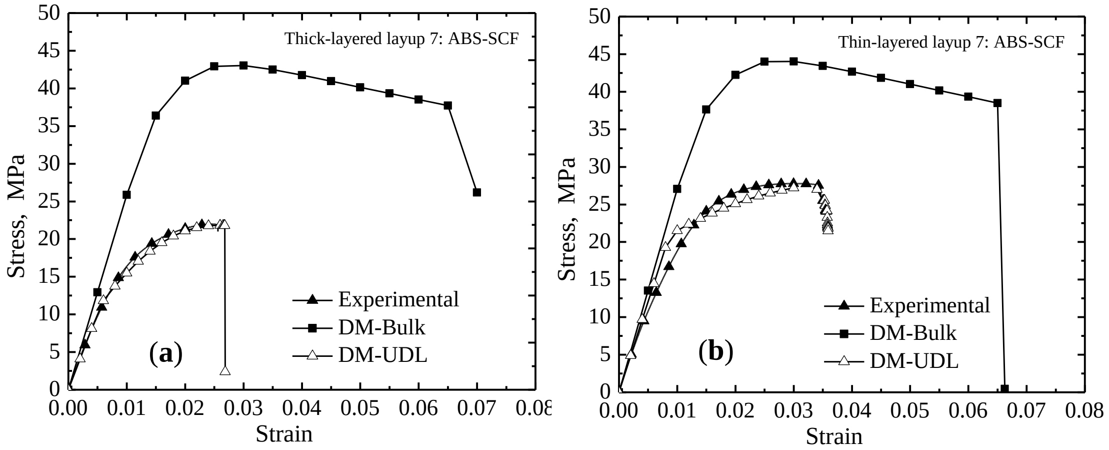

Figure 7.8. Stress–strain relation for laminate (layup 7) fabricated with ABS-SCF material for a (a) thick-layered laminate and (b) thin-layered laminate.

Table 7.6. Comparison of damage modeling and Tsai–Hill failure criteria results with experimental work for laminate layup 7 fabricated with ABS-SCF material and subjected to uniaxial tensile loading.

	Experimental	CLT and Tsai–Hill	Multiscale modeling	
			DM-Bulk	DM-UDL
Thick-layered laminate				
E_x, in MPa	2094.6 ± 43.5	1733.3	2594.0	2053.9
U_t, in MPa	21.7 ± 0.5	22.7	43.52	24.3
ε_t	0.0243 ±0.0011	0.0105	0.07	0.028
Thin-layered laminate				
E_x, in MPa	2330.6 ± 2.1	2150.5	2713.1	2453.3
U_t, in MPa	27.7 ± 0.4	31.1	44.0	29.1
ε_t	0.0373 ±0.0013	0.0105	0.063	0.036

The comparison of the stress–strain curves obtained from the experimental work and the damage modeling for parts fabricated with ABS-SCF material reveals that the damage model based on bulk material properties (DM-Bulk) predicts higher values. The difference between them for nonlinear properties such as strength and strain to failure is ~50%. This means that the selected damage model does not represent the actual damage phenomena that occurred in parts fabricated with ABS-SCF material. One of the main reasons for this discrepancy is that the debonding between the SCF reinforcements and the ABS matrix is not represented in the damage model. Other reasons are the assumptions made in the FE models of the RVEs. The FE models assume perfect bonding between the extruded fibers, uniform length and perfect orientation of SCFs, and perfect bonding between the SCF reinforcements and the matrix. The stress–strain curves from the experimental work initially show a linear region that follows hardening behaviour, and then the parts fail suddenly. Hardening behaviour in these parts is due to the presence of SCF reinforcements. Nonlinearity arises when bonding between the SCFs and the matrix starts failing during deformation. Furthermore, sudden failure follows the hardening behaviour because of the presence of enclosed voids. During deformation, the enclosed voids start to coalesce, resulting in a lager discontinuity in the material. This leads to sudden failure of the parts. The actual damage phenomena in the composite parts fabricated with ABS-SCF material can be achieved by considering tensile test data of unidirectional laminates. The damage model (DM-UDL) considered the test results of the unidirectional laminates and the results based on this damage model replicate the actual nonlinear behavior of the printed parts.

7.4 Conclusions

The present work addressed computational damage modeling of 3D printed laminates subjected to uniaxial tensile loading. Damage analysis was carried out by considering a continuum damage model for isotropic materials, as the base materials used for printing the parts were isotropic. The computational damage results were then compared with experimental work to validate the computational procedure adopted in this chapter. The main observations made in this chapter are as follows:

- The material behaviour of printed parts fabricated with only ABS material displays initial linear behaviour followed by nonlinear softening behaviour, and then the parts fail suddenly. This behaviour is modeled with an isotropic damage model with plasticity law in the present analysis. The computational damage results are comparable to the experimental results. The damage model predicted values that are higher than those obtained using both the first-ply failure criterion and experimental work. The damage model that employed test data of unidirectional laminates accurately predicted the nonlinear material behaviour of printed parts fabricated with ABS material.
- In the damage modeling of the parts fabricated with ABS-SCF material, the nonlinearity in these parts is mainly attributable to ABS material. Therefore, the nonlinear behaviour of the ABS material was considered in the damage models. However, the material of

the SCF reinforcements remains elastic during deformation. The damage model (DM-Bulk) predicted values that were higher than the experimental values. These results mean that the damage model does not represent the actual material behaviour of ABS-SCF printed parts. The actual nonlinear material behavior of the parts was achieved by considering the nonlinear test data of unidirectional laminates in the damage model (DM-UDL).

Chapter 8 Conclusions and Future Work

Summary: This chapter outlines the statement of the problem, objective of the study, and contributions of this work to the field. Furthermore, a brief description of areas that deserve further exploration in future work is presented.

8.1 Statement of the problem

Despite the many benefits of additive manufacturing (AM), anisotropy in the material properties of the resulting 3D printed parts is of primary concern. Anisotropy in the material properties is the result of variation introduced into the mesostructure of a part during the 3D printing process. Moreover, our understanding of the process–structure–property relationship is currently limited for printed parts. The effective design and analysis of models for 3D printing calls for an investigation at different scales of the material in order to better understand the behaviour of the printed parts. Composite parts fabricated via the material extrusion AM method have wide industrial applications for functional usage. Such structural parts need reliable design despite concerns about anisotropy being introduced during the 3D printing process. Therefore, computational models need to be explored to enable the reliable design of models for 3D printing.

8.2 Objectives

The investigation of the anisotropic material behaviour of 3D printed parts centred on the following four objectives:

i. Investigate the material behaviour of printed parts by conducting mechanical testing;

ii. Characterize the mechanical behaviour of printed parts using material mechanics based on experimental data, and then investigate the failure behaviour of printed parts;

iii. Characterize the mesostructure of 3D printed parts using microscopy and a micro-CT scanner, and investigate the influence of microstructural features on the final properties of printed parts; and

iv. Enable effective design and analysis of structural parts by developing computational micromechanical models for the material modeling of 3D printed parts.

8.3 General conclusions

8.3.1 Investigation of material behaviour of printed parts using mechanical testing

The results of the mechanical tests on printed test coupons revealed their material behaviour under tensile and flexural loads. The material behaviour of the parts is governed by their mesostructure, which is produced during the 3D printing process. This means that the microstructural aspects of printed parts influence the final material properties. In general, the behaviour of the printed parts resembles that of traditional composite laminates.

8.3.2 Characterization of mechanical behaviour of printed parts using laminate mechanics

Since the behaviour of printed parts is similar to that of traditional laminates, laminate mechanics can be employed to characterize the mechanical behaviour of printed parts. The orthotropic constitutive behaviour of the layers of printed parts was established using laminate mechanics. Laminate theories more accurately predict the mechanical behaviour of printed parts fabricated with only isotropic polymeric material than the behaviour of printed parts fabricated with composite material.

8.3.3 Characterization of the microstructure of printed composite parts

The microstructure of composite printed parts was characterized by conducting a morphological study using a micro-CT scanner. The constituents of the microstructure, namely the size, shape, and distribution of short carbon fiber (SCF) reinforcements as well as their percentage by volume, influenced the final material properties of the printed parts. Continuous voids were found at the interface of the layers of the printed parts. In addition, irregularly shaped enclosed voids were found in the extruded filaments of thick-layered but not thin-layered composite parts. Further, the enclosed voids disturbed the orientation of SCF reinforcements in thick-layered composite parts. Layer thickness of the printed parts also influenced the length distribution of the SCF reinforcements. Such differences between the thick-layered and thin-layered composite parts led to discrepant results.

8.3.4 Computational micromechanical model for material modeling of printed parts

The microstructure of printed parts was considered in finite element (FE) models for material modeling. The overall constitutive matrix of the printed parts was estimated using the numerical homogenization technique. Furthermore, the material nonlinear behaviour of the printed parts was investigated using damage models. The material behaviour of the printed parts based on the computational models was then validated with experimental findings. The computational models accurately predicted the behaviour of printed parts. The computational models minimize time-consuming and tedious experimental work and will be instrumental in the effective design and analysis of models for 3D printing.

8.3.5 Case study from appendix

The build orientation of a model influences the final material properties of printed parts. Investigation of an L-bracket structure using a computational model revealed that the material disposition strategy influenced the constitutive material behaviour of the members of the structural part.

8.4 Thesis contributions

The main contributions of this work are as follows:

(i) The behaviour of 3D printed parts is similar to that of laminate structures, and thus printed parts can be treated as printed laminates.

(ii) Mesostructural aspects of 3D printed parts govern the final material properties of the parts, and hence the mesostructure can be tailored to achieve the desired final properties.

(iii) Laminate mechanics can be employed in the characterization of the mechanical behaviour of 3D printed parts as well as in the preliminary design of models for 3D printing.

(iv) Computational methodology can be employed to estimate the constitutive matrix of 3D printed parts and also to conduct damage modeling of the parts. This minimizes the experimental work required and also provides freedom in the design and analysis of models for 3D printing.

(v) The process–structure–property relationship has been established for printed parts.

To account the material behavior of parts, the constitutive matrix of materials is considered during design and analysis of structures. The final constitutive matrix of materials of printed parts is different from its initial material due to change in mesostructure while 3D printing. Therefore, the final constitutive matrix need to be estimated for effective design and analysis of structures. The present multiscale computational models can estimate the effective constitutive matrix by considering mesostructure and its base material properties. Then, the estimated effective final properties can be used during design and FEA of structures subjecting to mechanical loads. Furthermore, the computational model can be used to carryout the damage analysis of structures subjecting to mechanical loads. An application of this work is discussed in Appendix A.

8.5 Future work

The following areas merit further investigation:

(i) Development of a printing process that eliminates the voids in 3D printed parts to improve their structural integrity;

(ii) Development of computational models that account for bonding between the layers of 3D printed parts; and

(iii) Exploration of a computational methodology for 3D printed parts fabricated with different materials.

References

[1] Gibson I, Rosen DW, Stucker B. Additive manufacturing technologies. New York: Springer; 2014.

[2] Bourell DL. Perspectives on additive manufacturing. Annual Review of Materials Research. 2016; 46:1-8.

[3] Guo N, Leu MC. Additive manufacturing: technology, applications and research needs. Frontiers of Mechanical Engineering. 2013; 8(3):215-43.

[4] Kotlinski J. Mechanical properties of commercial rapid prototyping materials. Rapid Prototyping Journal. 2014; 20(6):499-510.

[5] Gao W, Zhang Y, Ramanujan D, Ramani K, Chen Y, Williams CB, Wang CC, Shin YC, Zhang S, Zavattieri PD. The status, challenges, and future of additive manufacturing in engineering. Computer-Aided Design. 2015; 69:65-89.

[6] Quan Z, Wu A, Keefe M, Qin X, Yu J, Suhr J, Byun JH, Kim BS, Chou TW. Additive manufacturing of multi-directional preforms for composites: opportunities and challenges. Materials Today. 2015; 18(9):503-12.

[7] Kalsoom U, Nesterenko PN, Paull B. Recent developments in 3D printable composite materials. RSC Advances. 2016; 6(65):60355-71.

[8] Parandoush P, Lin D. A review on additive manufacturing of polymer-fiber composites. Composite Structures. 2017; 182:36-53.

[9] Kumar S, Kruth JP. Composites by rapid prototyping technology. Materials & Design. 2010 ;31(2):850-6.

[10] Yakout M, Elbestawi MA. Additive manufacturing of composite materials: an overview. In6th International Conference on Virtual Machining Process Technology (VMPT), Montréal, May 29th–June 2nd 2017.

[11] Sugiyama K, Matsuzaki R, Ueda M, Todoroki A, Hirano Y. 3D printing of composite sandwich structures using continuous carbon fiber and fiber tension. Composites Part A: Applied Science and Manufacturing. 2018; 113:114-21.

[12] Quan Z, Suhr J, Yu J, Qin X, Cotton C, Mirotznik M, Chou TW. Printing direction dependence of mechanical behavior of additively manufactured 3D preforms and composites. Composite Structures. 2018; 184:917-23.

[13] Liu Y, Zhang W, Zhang F, Lan X, Leng J, Liu S, Jia X, Cotton C, Sun B, Gu B, Chou TW. Shape memory behavior and recovery force of 4D printed laminated Miura-origami structures subjected to compressive loading. Composites Part B: Engineering. 2018; 153:233-42.

[14] Fleischer J, Teti R, Lanza G, Mativenga P, Möhring HC, Caggiano A. Composite materials parts manufacturing. CIRP Annals. 2018 ;67(2):603-26.

[15] Tekinalp HL, Kunc V, Velez-Garcia GM, Duty CE, Love LJ, Naskar AK, Blue CA, Ozcan S. Highly oriented carbon fiber–polymer composites via additive manufacturing. Composites Science and Technology. 2014; 105:144-50.

[16] Lewicki JP, Rodriguez JN, Zhu C, Worsley MA, Wu AS, Kanarska Y, Horn JD, Duoss EB, Ortega JM, Elmer W, Hensleigh R. 3D-printing of meso-structurally ordered carbon fiber/polymer composites with unprecedented orthotropic physical properties. Scientific reports. 2017; 7:43401.

[17] Brenken B, Barocio E, Favaloro A, Kunc V, Pipes RB. Fused filament fabrication of fiber-reinforced polymers: A review. Additive Manufacturing. 2018; 21:1-6.

[18] Ahn SH, Montero M, Odell D, Roundy S, Wright PK. Anisotropic material properties of fused deposition modeling ABS. Rapid prototyping journal. 2002; 8(4):248-57.

[19] Ngo TD, Kashani A, Imbalzano G, Nguyen KT, Hui D. Additive manufacturing (3D printing): A review of materials, methods, applications and challenges. Composites Part B: Engineering. 2018; 143:172-96.

[20] Turner BN, Strong R, Gold SA. A review of melt extrusion additive manufacturing processes: I. Process design and modeling. Rapid Prototyping Journal. 2014; 20(3):192-204.

[21] Cuan-Urquizo E, Barocio E, Tejada-Ortigoza V, Pipes RB, Rodriguez CA, Roman-Flores A. Characterization of the Mechanical Properties of FFF Structures and Materials: A Review on the Experimental, Computational and Theoretical Approaches. Materials. 2019; 12(6):895.

[22] Ding Z, Weeger O, Qi HJ, Dunn ML. 4D rods: 3D structures via programmable 1D composite rods. Materials & design. 2018; 137:256-65.

[23] Zarek M, Layani M, Cooperstein I, Sachyani E, Cohn D, Magdassi S. 3D printing of shape memory polymers for flexible electronic devices. Advanced Materials. 2016; 28(22):4449-54.

[24] Chen H, Yang X, Chen L, Wang Y, Sun Y. Application of FDM three-dimensional printing technology in the digital manufacture of custom edentulous mandible trays. Scientific reports. 2016; 6:19207.

[25] Miao S, Castro N, Nowicki M, Xia L, Cui H, Zhou X, Zhu W, Lee SJ, Sarkar K, Vozzi G, Tabata Y. 4D printing of polymeric materials for tissue and organ regeneration. Materials Today. 2017; 20(10):577-91.

[26] Gladman AS, Matsumoto EA, Nuzzo RG, Mahadevan L, Lewis JA. Biomimetic 4D printing. Nature materials. 2016; 15(4):413.

[27] Yao X, Luan C, Zhang D, Lan L, Fu J. Evaluation of carbon fiber-embedded 3D printed structures for strengthening and structural-health monitoring. Materials & Design. 2017; 114:424-32.

[28] Christ JF, Aliheidari N, Ameli A, Pötschke P. 3D printed highly elastic strain sensors of multiwalled carbon nanotube/thermoplastic polyurethane nanocomposites. Materials & Design. 2017; 131:394-401.

[29] Saleh MA, Kempers R, Melenka GW. 3D printed continuous wire polymer composites strain sensors for structural health monitoring. Smart Materials and Structures. 2019 Jan 11.

[30] Gu GX, Takaffoli M, Hsieh AJ, Buehler MJ. Biomimetic additive manufactured polymer composites for improved impact resistance. Extreme Mechanics Letters. 2016; 9:317-23.

[31] Su R, Campbell GM, Boyd SK. Establishment of an architecture-specific experimental validation approach for finite element modeling of bone by rapid prototyping and high resolution computed tomography. Medical engineering & physics. 2007; 29(4):480-90.

[32] Kalita SJ, Bose S, Hosick HL, Bandyopadhyay A. Development of controlled porosity polymer-ceramic composite scaffolds via fused deposition modeling. Materials Science and Engineering: C. 2003; 23(5):611-20.

[33] Türk DA, Einarsson H, Lecomte C, Meboldt M. Design and manufacturing of high-performance prostheses with additive manufacturing and fiber-reinforced polymers. Production Engineering. 2018; 12(2):203-13.

[34] Mahmoud D, Elbestawi M. Lattice structures and functionally graded materials applications in additive manufacturing of orthopedic implants: A review. Journal of Manufacturing and Materials Processing. 2017; 1(2):13.

[35] Gibson MA, Mykulowycz NM, Shim J, Fontana R, Schmitt P, Roberts A, Ketkaew J, Shao L, Chen W, Bordeenithikasem P, Myerberg JS. 3D printing metals like thermoplastics: Fused filament fabrication of metallic glasses. Materials Today. 2018; 21(7):697-702.

[36] Duty CE, Kunc V, Compton B, Post B, Erdman D, Smith R, Lind R, Lloyd P, Love L. Structure and mechanical behavior of Big Area Additive Manufacturing (BAAM) materials. Rapid Prototyping Journal. 2017; 23(1):181-9.

[37] Goh GD, Yap YL, Agarwala S, Yeong WY. Recent progress in additive manufacturing of fiber reinforced polymer composite. Advanced Materials Technologies. 2019; 4(1):1800271.

[38] Popescu D, Zapciu A, Amza C, Baciu F, Marinescu R. FDM process parameters influence over the mechanical properties of polymer specimens: A review. Polymer Testing. 2018; 69:157-66.

[39] Rodríguez JF, Thomas JP, Renaud JE. Mechanical behavior of acrylonitrile butadiene styrene (ABS) fused deposition materials. Experimental investigation. Rapid Prototyping Journal. 2001; 7(3):148-58.

[40] Koch C, Van Hulle L, Rudolph N. Investigation of mechanical anisotropy of the fused filament fabrication process via customized tool path generation. Additive Manufacturing. 2017; 16:138-45.

[41] Melenka GW, Schofield JS, Dawson MR, Carey JP. Evaluation of dimensional accuracy and material properties of the MakerBot 3D desktop printer. Rapid Prototyping Journal. 2015; 21(5):618-27.

[42] Tymrak BM, Kreiger M, Pearce JM. Mechanical properties of components fabricated with open-source 3-D printers under realistic environmental conditions. Materials & Design. 2014; 58:242-6.

[43] Kumar S, Bhushan P, Bhattacharya S. Investigation of structure-mechanical property relationship in fused filament fabrication of the polymer composites n.d. doi:10.1177/2516598419843687.

[44] Agarwala MK, Jamalabad VR, Langrana NA, Safari A, Whalen PJ, Danforth SC. Structural quality of parts processed by fused deposition. Rapid prototyping journal. 1996; 2(4):4-19.

[45] Kulkarni P, Marsan A, Dutta D. A review of process planning techniques in layered manufacturing. Rapid prototyping journal. 2000; 6(1):18-35.

[46] Durgun I, Ertan R. Experimental investigation of FDM process for improvement of mechanical properties and production cost. Rapid Prototyping Journal. 2014; 20(3):228-35.

[47] Huang B, Singamneni S. Raster angle mechanics in fused deposition modelling. Journal of Composite Materials. 2015; 49(3):363-83.

[48] Wu W, Geng P, Li G, Zhao D, Zhang H, Zhao J. Influence of layer thickness and raster angle on the mechanical properties of 3D-printed PEEK and a comparative mechanical study between PEEK and ABS. Materials. 2015; 8(9):5834-46.

[49] Ning F, Cong W, Hu Y, Wang H. Additive manufacturing of carbon fiber-reinforced plastic composites using fused deposition modeling: Effects of process parameters on tensile properties. Journal of Composite Materials. 2017; 51(4):451-62.

[50] Cantrell JT, Rohde S, Damiani D, Gurnani R, DiSandro L, Anton J, Young A, Jerez A, Steinbach D, Kroese C, Ifju PG. Experimental characterization of the mechanical properties of 3D-printed ABS and polycarbonate parts. Rapid Prototyping Journal. 2017; 23(4):811-24.

[51] Rezayat H, Zhou W, Siriruk A, Penumadu D, Babu SS. Structure–mechanical property relationship in fused deposition modelling. Materials Science and Technology. 2015; 31(8):895-903.

[52] Ziemian S, Okwara M, Ziemian CW. Tensile and fatigue behavior of layered acrylonitrile butadiene styrene. Rapid Prototyping Journal. 2015; 21(3):270-8.

[53] Ziemian C, Sharma M, Ziemian S. Anisotropic mechanical properties of ABS parts fabricated by fused deposition modelling. InMechanical engineering 2012 Apr 11. InTechOpen.

[54] Riddick JC, Haile MA, Von Wahlde R, Cole DP, Bamiduro O, Johnson TE. Fractographic analysis of tensile failure of acrylonitrile-butadiene-styrene fabricated by fused deposition modeling. Additive Manufacturing. 2016; 11:49-59.

[55] Torres J, Cotelo J, Karl J, Gordon AP. Mechanical property optimization of FDM PLA in shear with multiple objectives. Jom. 2015; 67(5):1183-93.

[56] Fonseca J, Ferreira IA, de Moura MF, Machado M, Alves JL. Study of the interlaminar fracture under mode I loading on FFF printed parts. Composite Structures. 2019; 214:316-24.

[57] Sun Q, Rizvi GM, Bellehumeur CT, Gu P. Effect of processing conditions on the bonding quality of FDM polymer filaments. Rapid Prototyping Journal. 2008; 14(2):72-80.

[58] Bellehumeur C, Li L, Sun Q, Gu P. Modeling of bond formation between polymer filaments in the fused deposition modeling process. Journal of Manufacturing Processes. 2004; 6(2):170-8.

[59] Aliheidari N, Tripuraneni R, Ameli A, Nadimpalli S. Fracture resistance measurement of fused deposition modeling 3D printed polymers. Polymer Testing. 2017; 60:94-101.

[60] Abbott AC, Tandon GP, Bradford RL, Koerner H, Baur JW. Process-structure-property effects on ABS bond strength in fused filament fabrication. Additive Manufacturing. 2018; 19:29-38.

[61] Hart KR, Dunn RM, Sietins JM, Mock CM, Mackay ME, Wetzel ED. Increased fracture toughness of additively manufactured amorphous thermoplastics via thermal annealing. Polymer. 2018; 144:192-204.

[62] Singh R, Singh S, Singh IP, Fabbrocino F, Fraternali F. Investigation for surface finish improvement of FDM parts by vapor smoothing process. Composites Part B: Engineering. 2017; 111:228-34.

[63] Rodríguez JF, Thomas JP, Renaud JE. Design of fused-deposition ABS components for stiffness and strength. Journal of Mechanical Design. 2003; 125(3):545-51.

[64] McLouth TD, Severino JV, Adams PM, Patel DN, Zaldivar RJ. The impact of print orientation and raster pattern on fracture toughness in additively manufactured ABS. Additive Manufacturing. 2017; 18:103-9.

[65] Martínez J, Diéguez JL, Ares JE, Pereira A, Pérez JA. Modelization and structural analysis of FDM parts. InAIP Conference Proceedings 2012 Apr 30 (Vol. 1431, No. 1, pp. 842-848). AIP.

[66] Zaldivar RJ, Witkin DB, McLouth T, Patel DN, Schmitt K, Nokes JP. Influence of processing and orientation print effects on the mechanical and thermal behavior of 3D-Printed ULTEM® 9085 Material. Additive Manufacturing. 2017; 13:71-80.

[67] Türk DA, Brenni F, Zogg M, Meboldt M. Mechanical characterization of 3D printed polymers for fiber reinforced polymers processing. Materials & Design. 2017; 118:256-65.

[68] Zou R, Xia Y, Liu S, Hu P, Hou W, Hu Q, Shan C. Isotropic and anisotropic elasticity and yielding of 3D printed material. Composites Part B: Engineering. 2016; 99:506-13.

[69] Bellini A, Güçeri S. Mechanical characterization of parts fabricated using fused deposition modeling. Rapid Prototyping Journal. 2003; 9(4):252-64.

[70] Domingo-Espin M, Puigoriol-Forcada JM, Garcia-Granada AA, Llumà J, Borros S, Reyes G. Mechanical property characterization and simulation of fused deposition modeling Polycarbonate parts. Materials & Design. 2015; 83:670-7.

[71] Thrimurthulu KP, Pandey PM, Reddy NV. Optimum part deposition orientation in fused deposition modeling. International Journal of Machine Tools and Manufacture. 2004; 44(6):585-94.

[72] Delfs P, Tows M, Schmid HJ. Optimized build orientation of additive manufactured parts for improved surface quality and build time. Additive Manufacturing. 2016; 12:314-20.

[73] Kao YT, Zhang Y, Wang J, Tai BL. Bending behaviors of 3D-printed Bi-material structure: Experimental study and finite element analysis. Additive Manufacturing. 2017; 16:197-205.

[74] Garg A, Bhattacharya A. An insight to the failure of FDM parts under tensile loading: finite element analysis and experimental study. International Journal of Mechanical Sciences. 2017; 120:225-36.

[75] Ravari MK, Kadkhodaei M, Badrossamay M, Rezaei R. Numerical investigation on mechanical properties of cellular lattice structures fabricated by fused deposition modeling. International Journal of Mechanical Sciences. 2014; 88:154-61.

[76] Zhang Y, Zhang F, Yan Z, Ma Q, Li X, Huang Y, Rogers JA. Printing, folding and assembly methods for forming 3D mesostructures in advanced materials. Nature Reviews Materials. 2017; 2(4):17019.

[77] Tronvoll SA, Welo T, Elverum CW. The effects of voids on structural properties of fused deposition modelled parts: A probabilistic approach. The International Journal of Advanced Manufacturing Technology. 2018; 97(9-12):3607-18.

[78] Wang J, Xie H, Weng Z, Senthil T, Wu L. A novel approach to improve mechanical properties of parts fabricated by fused deposition modeling. Materials & Design. 2016; 105:152-9.

[79] Rodriguez JF, Thomas JP, Renaud JE. Characterization of the mesostructure of fused-deposition acrylonitrile-butadiene-styrene materials. Rapid Prototyping Journal. 2000; 6(3):175-86.

[80] Chacón JM, Caminero MÁ, García-Plaza E, Núñez PJ. Additive manufacturing of PLA structures using fused deposition modelling: Effect of process parameters on mechanical properties and their optimal selection. Materials & Design. 2017; 124:143-57.

[81] Rodríguez JF, Thomas JP, Renaud JE. Mechanical behavior of acrylonitrile butadiene styrene fused deposition materials modeling. Rapid Prototyping Journal. 2003; 9(4):219-30.

[82] Liu X, Shapiro V. Homogenization of material properties in additively manufactured structures. Computer-Aided Design. 2016; 78:71-82.

[83] Hu Z, Thiyagarajan K, Bhusal A, Letcher T, Fan QH, Liu Q, Salem D. Design of ultra-lightweight and high-strength cellular structural composites inspired by biomimetics. Composites Part B: Engineering. 2017; 121:108-21.

[84] Lee JY, An J, Chua CK. Fundamentals and applications of 3D printing for novel materials. Applied Materials Today. 2017; 7:120-33.

[85] Ligon SC, Liska R, Stampfl J, Gurr M, Mülhaupt R. Polymers for 3D printing and customized additive manufacturing. Chemical reviews. 2017; 117(15):10212-90.

[86] Bourell D, Kruth JP, Leu M, Levy G, Rosen D, Beese AM, Clare A. Materials for additive manufacturing. CIRP Annals. 2017; 66(2):659-81.

[87] Novakova-Marcincinova L, Kuric I. Basic and advanced materials for fused deposition modeling rapid prototyping technology. Manuf. and Ind. Eng. 2012;11(1):24-7.

[88] Salentijn GI, Oomen PE, Grajewski M, Verpoorte E. Fused deposition modeling 3D printing for (bio) analytical device fabrication: procedures, materials, and applications. Analytical chemistry. 2017; 89(13):7053-61.

[89] Masood SH, Song WQ. Development of new metal/polymer materials for rapid tooling using fused deposition modelling. Materials & design. 2004; 25(7):587-94.

[90] Dul S, Fambri L, Pegoretti A. Fused deposition modelling with ABS–graphene nanocomposites. Composites Part A: Applied Science and Manufacturing. 2016; 85:181-91.

[91] Ryder MA, Lados DA, Iannacchione GS, Peterson AM. Fabrication and properties of novel polymer-metal composites using fused deposition modeling. Composites Science and Technology. 2018; 158:43-50.

[92] Weng Z, Wang J, Senthil T, Wu L. Mechanical and thermal properties of ABS/montmorillonite nanocomposites for fused deposition modeling 3D printing. Materials & Design. 2016; 102:276-83.

[93] Singh R, Singh S, Fraternali F. Development of in-house composite wire based feed stock filaments of fused deposition modelling for wear-resistant materials and structures. Composites Part B: Engineering. 2016; 98:244-9.

[94] Wei X, Li D, Jiang W, Gu Z, Wang X, Zhang Z, Sun Z. 3D printable graphene composite. Scientific reports. 2015; 5:11181.

[95] Luo J, Wang H, Zuo D, Ji A, Liu Y. Research on the Application of MWCNTs/PLA Composite Material in the Manufacturing of Conductive Composite Products in 3D Printing. Micromachines. 2018; 9(12):635.

[96] Nikzad M, Masood SH, Sbarski I. Thermo-mechanical properties of a highly filled polymeric composites for fused deposition modeling. Materials & Design. 2011; 32(6):3448-56.

[97] Lewicki JP, Rodriguez JN, Zhu C, Worsley MA, Wu AS, Kanarska Y, Horn JD, Duoss EB, Ortega JM, Elmer W, Hensleigh R. 3D-printing of meso-structurally ordered carbon fiber/polymer composites with unprecedented orthotropic physical properties. Scientific reports. 2017; 7:43401.

[98] Kwok SW, Goh KH, Tan ZD, Tan ST, Tjiu WW, Soh JY, Ng ZJ, Chan YZ, Hui HK, Goh KE. Electrically conductive filament for 3D-printed circuits and sensors. Applied Materials Today. 2017; 9:167-75.

[99] Spackman CC, Frank CR, Picha KC, Samuel J. 3D printing of fiber-reinforced soft composites: Process study and material characterization. Journal of Manufacturing Processes. 2016; 23:296-305.

[100] Gnanasekaran K, Heijmans T, Van Bennekom S, Woldhuis H, Wijnia S, de With G, Friedrich H. 3D printing of CNT-and graphene-based conductive polymer nanocomposites by fused deposition modeling. Applied materials today. 2017; 9:21-8.

[101] Hwang S, Reyes EI, Moon KS, Rumpf RC, Kim NS. Thermo-mechanical characterization of metal/polymer composite filaments and printing parameter study for fused deposition modeling in the 3D printing process. Journal of Electronic Materials. 2015; 44(3):771-7.

[102] Melenka GW, Cheung BK, Schofield JS, Dawson MR, Carey JP. Evaluation and prediction of the tensile properties of continuous fiber-reinforced 3D printed structures. Composite Structures. 2016; 153:866-75.

[103] Matsuzaki R, Ueda M, Namiki M, Jeong TK, Asahara H, Horiguchi K, Nakamura T, Todoroki A, Hirano Y. Three-dimensional printing of continuous-fiber composites by in-nozzle impregnation. Scientific reports. 2016; 6:23058.

[104] Yang C, Tian X, Liu T, Cao Y, Li D. 3D printing for continuous fiber reinforced thermoplastic composites: mechanism and performance. Rapid Prototyping Journal. 2017; 23(1):209-15.

[105] Justo J, Távara L, García-Guzmán L, París F. Characterization of 3D printed long fibre reinforced composites. Composite Structures. 2018; 185:537-48.

[106] Dickson AN, Barry JN, McDonnell KA, Dowling DP. Fabrication of continuous carbon, glass and Kevlar fibre reinforced polymer composites using additive manufacturing. Additive Manufacturing. 2017; 16:146-52.

[107] Love LJ, Kunc V, Rios O, Duty CE, Elliott AM, Post BK, Smith RJ, Blue CA. The importance of carbon fiber to polymer additive manufacturing. Journal of Materials Research. 2014; 29(17):1893-8.

[108] Quan Z, Larimore Z, Wu A, Yu J, Qin X, Mirotznik M, Suhr J, Byun JH, Oh Y, Chou TW. Microstructural design and additive manufacturing and characterization of 3D orthogonal short carbon fiber/acrylonitrile-butadiene-styrene preform and composite. Composites Science and Technology. 2016; 126:139-48.

[109] Compton BG, Lewis JA. 3D-printing of lightweight cellular composites. Advanced materials. 2014; 26(34):5930-5.

[110] Bickel B, Bächer M, Otaduy MA, Lee HR, Pfister H, Gross M, Matusik W. Design and fabrication of materials with desired deformation behavior. ACM Transactions on Graphics (TOG). 2010; 29(4):63.

[111] Zhang H, Yang D, Sheng Y. Performance-driven 3D printing of continuous curved carbon fibre reinforced polymer composites: A preliminary numerical study. Composites Part B: Engineering. 2018; 151:256-64.

[112] Steuben JC, Iliopoulos AP, Michopoulos JG. Implicit slicing for functionally tailored additive manufacturing. Computer-Aided Design. 2016; 77:107-19.

[113] Ning F, Cong W, Hu Z, Huang K. Additive manufacturing of thermoplastic matrix composites using fused deposition modeling: A comparison of two reinforcements. Journal of Composite Materials. 2017; 51(27):3733-42.

[114] Prüß H, Vietor T. Design for fiber-reinforced additive manufacturing. Journal of Mechanical Design. 2015; 137(11):111409.

[115] Tian X, Liu T, Yang C, Wang Q, Li D. Interface and performance of 3D printed continuous carbon fiber reinforced PLA composites. Composites Part A: Applied Science and Manufacturing. 2016; 88:198-205.

[116] Zhang W, Wu AS, Sun J, Quan Z, Gu B, Sun B, Cotton C, Heider D, Chou TW. Characterization of residual stress and deformation in additively manufactured ABS polymer and composite specimens. Composites Science and Technology. 2017; 150:102-10.

[117] Liao G, Li Z, Cheng Y, Xu D, Zhu D, Jiang S, Guo J, Chen X, Xu G, Zhu Y. Properties of oriented carbon fiber/polyamide 12 composite parts fabricated by fused deposition modeling. Materials & Design. 2018; 139:283-92.

[118] Anwer A, Naguib HE. Multi-functional flexible carbon fiber composites with controlled fiber alignment using additive manufacturing. Additive Manufacturing. 2018; 22:360-7.

[119] Ning F, Cong W, Qiu J, Wei J, Wang S. Additive manufacturing of carbon fiber reinforced thermoplastic composites using fused deposition modeling. Composites Part B: Engineering. 2015; 80:369-78.

[120] Ivey M, Melenka GW, Carey JP, Ayranci C. Characterizing short-fiber-reinforced composites produced using additive manufacturing. Advanced Manufacturing: Polymer & Composites Science. 2017; 3(3):81-91.

[121] Nakagawa Y, Mori KI, Maeno T. 3D printing of carbon fibre-reinforced plastic parts. The International Journal of Advanced Manufacturing Technology. 2017; 91(5-8):2811-7.

[122] Sweeney CB, Lackey BA, Pospisil MJ, Achee TC, Hicks VK, Moran AG, Teipel BR, Saed MA, Green MJ. Welding of 3D-printed carbon nanotube–polymer composites by locally induced microwave heating. Science advances. 2017; 3(6):e1700262.

[123] Spoerk M, Savandaiah C, Arbeiter F, Traxler G, Cardon L, Holzer C, Sapkota J. Anisotropic properties of oriented short carbon fibre filled polypropylene parts fabricated by extrusion-based additive manufacturing. Composites Part A: Applied Science and Manufacturing. 2018; 113:95-104.

[124] Jiang D, Smith DE. Anisotropic mechanical properties of oriented carbon fiber filled polymer composites produced with fused filament fabrication. Additive Manufacturing. 2017; 18:84-94.

[125] Stepashkin AA, Chukov DI, Senatov FS, Salimon AI, Korsunsky AM, Kaloshkin SD. 3D-printed PEEK-carbon fiber (CF) composites: Structure and thermal properties. Composites Science and Technology. 2018; 164:319-26.

[126] Chen Q, Mangadlao JD, Wallat J, De Leon A, Pokorski JK, Advincula RC. 3D printing biocompatible polyurethane/poly (lactic acid)/graphene oxide nanocomposites: anisotropic properties. ACS applied materials & interfaces. 2017; 9(4):4015-23.

[127] Song Y, Li Y, Song W, Yee K, Lee KY, Tagarielli VL. Measurements of the mechanical response of unidirectional 3D-printed PLA. Materials & Design. 2017; 123:154-64.

[128] Kulkarni P, Dutta D. Deposition strategies and resulting part stiffnesses in fused deposition modeling. Journal of manufacturing science and engineering. 1999; 121(1):93-103.

[129] Li L, Sun Q, Bellehumeur C, Gu P. Composite modeling and analysis for fabrication of FDM prototypes with locally controlled properties. Journal of manufacturing processes. 2002; 4(2):129-41.

[130] Casavola C, Cazzato A, Moramarco V, Pappalettere C. Orthotropic mechanical properties of fused deposition modelling parts described by classical laminate theory. Materials & design. 2016; 90:453-8.

[131] Ahn SH, Baek C, Lee S, Ahn IS. Anisotropic tensile failure model of rapid prototyping parts-fused deposition modeling (FDM). International Journal of Modern Physics B. 2003; 17:1510-6.

[132] Yao T, Deng Z, Zhang K, Li S. A method to predict the ultimate tensile strength of 3D printing polylactic acid (PLA) materials with different printing orientations. Composites Part B: Engineering. 2019; 163:393-402.

[133] Bhandari S, Lopez-Anido R. Finite element analysis of thermoplastic polymer extrusion 3D printed material for mechanical property prediction. Additive Manufacturing. 2018; 22:187-96.

[134] Alaimo G, Marconi S, Costato L, Auricchio F. Influence of meso-structure and chemical composition on FDM 3D-printed parts. Composites Part B: Engineering. 2017; 113:371-80.

[135] Al Abadi H, Thai HT, Paton-Cole V, Patel VI. Elastic properties of 3D printed fibre-reinforced structures. Composite Structures. 2018; 193:8-18.

[136] Brooks H, Molony S. Design and evaluation of additively manufactured parts with three dimensional continuous fibre reinforcement. Materials & Design. 2016; 90:276-83.

[137] Ferreira RT, Amatte IC, Dutra TA, Bürger D. Experimental characterization and micrography of 3D printed PLA and PLA reinforced with short carbon fibers. Composites Part B: Engineering. 2017; 124:88-100.

[138] Ziemian CW, Ziemian RD, Haile KV. Characterization of stiffness degradation caused by fatigue damage of additive manufactured parts. Materials & Design. 2016; 109:209-18.

[139] Guessasma S, Belhabib S, Nouri H, Hassana OB. Anisotropic damage inferred to 3D printed polymers using fused deposition modelling and subject to severe compression. European Polymer Journal. 2016; 85:324-40.

[140] Perez ART, Roberson DA, Wicker RB. Fracture surface analysis of 3D-printed tensile specimens of novel ABS-based materials. Journal of Failure Analysis and Prevention. 2014; 14(3):343-53.

[141] Gomez-Gras G, Jerez-Mesa R, Travieso-Rodriguez JA, Lluma-Fuentes J. Fatigue performance of fused filament fabrication PLA specimens. Materials & Design. 2018; 140:278-85.

[142] Patterson AE, Pereira TR, Allison JT, Messimer SL. IZOD impact properties of full-density fused deposition modeling polymer materials with respect to raster angle and print orientation. Proceedings of the Institution of Mechanical Engineers, Part C: Journal of Mechanical Engineering Science. 2019:0954406219840385.

[143] Rankouhi B, Javadpour S, Delfanian F, Letcher T. Failure analysis and mechanical characterization of 3D printed ABS with respect to layer thickness and orientation. Journal of Failure Analysis and Prevention. 2016; 16(3):467-81.

[144] Torrado AR, Roberson DA. Failure analysis and anisotropy evaluation of 3D-printed tensile test specimens of different geometries and print raster patterns. Journal of Failure Analysis and Prevention. 2016; 16(1):154-64.

[145] Roberson DA, Perez AR, Shemelya CM, Rivera A, MacDonald E, Wicker RB. Comparison of stress concentrator fabrication for 3D printed polymeric izod impact test specimens. Additive Manufacturing. 2015; 7:1-1.

[146] Goh GD, Dikshit V, Nagalingam AP, Goh GL, Agarwala S, Sing SL, Wei J, Yeong WY. Characterization of mechanical properties and fracture mode of additively manufactured carbon fiber and glass fiber reinforced thermoplastics. Materials & Design. 2018; 137:79-89.

[147] Zhang W, Cotton C, Sun J, Heider D, Gu B, Sun B, Chou TW. Interfacial bonding strength of short carbon fiber/acrylonitrile-butadiene-styrene composites fabricated by fused deposition modeling. Composites Part B: Engineering. 2018; 137:51-9.

[148] Quan Z, Larimore Z, Qin X, Yu J, Mirotznik M, Byun JH, Oh Y, Chou TW. Microstructural characterization of additively manufactured multi-directional preforms and composites via X-ray micro-computed tomography. Composites Science and Technology. 2016; 131:48-60.

[149] Arbeiter F, Spoerk M, Wiener J, Gosch A, Pinter G. Fracture mechanical characterization and lifetime estimation of near-homogeneous components produced by fused filament fabrication. Polymer Testing. 2018; 66:105-13.

[150] Somireddy M, Czekanski A, Singh CV. Development of constitutive material model of 3D printed structure via FDM. Materials Today Communications. 2018; 15:143-52.

[151] Abbott AC, Tandon GP, Bradford RL, Koerner H, Baur JW. Process-structure-property effects on ABS bond strength in fused filament fabrication. Additive Manufacturing. 2018; 19:29-38.

[152] Jones, R.M.. Mechanics of composite materials. CRC press. 2014.

[153] Altair Hyperwork Manual 2017,
https://connect.altair.com/CP/downloads.html?suite=HyperWorks&tab=2.

[154] Bruker, Kontich, Belgium. Skyscan 1272 micro-CT manuals.

[155] Hassani B, Hinton E. A review of homogenization and topology optimization I—homogenization theory for media with periodic structure. Computers & Structures. 1998; 69(6):707-17.

[156] Mseis G. Multiscale Modeling and Homogenization of Composite Materials (Doctoral dissertation, UC Berkeley).

[157] Hassani B, Hinton E. A review of homogenization and topology opimization II—analytical and numerical solution of homogenization equations. Computers & structures. 1998; 69(6):719-38.

[158] Yuan Z, Fish J. Toward realization of computational homogenization in practice. International Journal for Numerical Methods in Engineering. 2008; 73(3):361-80.

[159] Xia Z, Zhang Y, Ellyin F. A unified periodical boundary conditions for representative volume elements of composites and applications. International Journal of Solids and Structures. 2003; 40(8):1907-21.

[160] Babu KP, Mohite PM, Upadhyay CS. Development of an RVE and its stiffness predictions based on mathematical homogenization theory for short fibre composites. International Journal of Solids and Structures. 2018; 130:80-104.

[161] Soden PD, Hinton MJ, Kaddour AS. Lamina properties, lay-up configurations and loading conditions for a range of fibre reinforced composite laminates. InFailure Criteria in Fibre-Reinforced-Polymer Composites 2004 Jan 1 (pp. 30-51). Elsevier.

[162] Maimí P, Camanho PP, Mayugo JA, Dávila CG. A continuum damage model for composite laminates: Part I–Constitutive model. Mechanics of Materials. 2007; 39(10):897-908.

[163] Maimí P, Camanho PP, Mayugo JA, Dávila CG. A continuum damage model for composite laminates: Part II–Computational implementation and validation. Mechanics of Materials. 2007; 39(10):909-19.

[164] Talreja R, Singh CV. Damage and failure of composite materials. Cambridge University Press; 2012.

[165] Van der Meer FP. Computational modeling of failure in composite laminates, PhD Thesis. 2010.

[166] Fish J, Yu Q, Shek K. Computational damage mechanics for composite materials based on mathematical homogenization. International journal for numerical methods in engineering. 1999; 45(11):1657-79.

[167] Kanouté P, Boso DP, Chaboche JL, Schrefler BA. Multiscale methods for composites: a review. Archives of Computational Methods in Engineering. 2009; 16(1):31-75.

[168] Daniel IM. Failure of Composite Materials. Strain, 2007; 43(1): 4-12.

[169] T Tay TE, Liu G, Tan VB, Sun XS, Pham DC. Progressive failure analysis of composites. Journal of Composite Materials. 2008; 42(18):1921-66.

[170] Mohite PM. First-ply Failure Theories And Damage Mechanisms In Unidirectional Laminated Composites A School on Mechanics of Fibre Reinforced Polymer Composites Knowledge Incubation for TEQIP Indian Institute of Technology Kanpur. n.d.

[171] Chaboche JL. Continuum damage mechanics: Part I—General concepts. Journal of applied mechanics. 1988; 55(1):59-64.

Appendix A Homogenization of a 3D-Printed L-Bracket: Application

Summary: This work investigates the influence of build orientation of a model on the final material properties. An L-bracket structure is considered for investigation. The variation in build orientation of a model also results in anisotropy in the final printed part. To accurately capture the mechanical behaviour of the material of the final printed part, the final constitutive matrix of the material should be employed in the stress analysis of the parts. The constitutive matrix of the material needs to be estimated to accurately capture the mechanical behaviour of the parts. This work focuses on the linear constitutive material modeling of models with different orientations. The constitutive material modeling of the printed parts is done using the numerical homogenization procedure presented in chapter 6. This section investigates the influence of layer deposition on the material behaviour of parts fabricated with different structural orientations.

A.1 Introduction

A structural part can be 3D printed in any orientation, with the build orientation of a part being chosen by the user while generating the G-code for printing. The material deposition strategy is generated by the slicer tool based on the orientation of the part on the substrate of the printer; furthermore, material deposition also influences the properties of the part [128]. Orthotropic material behaviour has been assessed by conducting experiments on parts built in different orientations [69,70]. The build time for printing and also surface quality depend on the build orientation of the part [71,72]. Experimental work [42,46,64–66,69–72,138] reveals the significance of build orientation and raster angle on the properties of printed parts.

Computational work [73–75] on the material behaviour of printed parts has been limited, and further exploration is required using multiscale models. Also not yet accounted for is the effect of build orientation in the calculation of the constitutive matrix and in the use of laminate theory to characterize the mechanical behaviour of printed parts [39,129,130]. From these previous works it is evident that build orientation influences the material properties of printed parts. Therefore, variation in the material behaviour due to build orientation should be considered in the characterization of the mechanical behaviour of parts using laminate theory. Another unexplored research area is the computation of the stiffness matrix for the material of printed parts to account for build orientations using numerical multiscale models. The present chapter addresses the computation of the constitutive matrix by considering the build orientation of parts using numerical homogenization.

The first step in this analysis is an examination of the effect of build orientation of a part on its mechanical properties. This is followed by an explanation of how the deposition strategy in different parts of the L-bracket introduces anisotropy in the material properties of the structure. Laminate theory is used to characterize the material behaviour of the layers deposited along the thickness of the geometry of the part. Then, the orthotropic material behaviour of layers deposited across the thickness of the geometry of a part is characterized because the build orientation of the part does not allow the use of laminate modeling. The computation of the mechanical properties of the material of the final printed part using the numerical homogenization method is then explained. Finally, the influence of build orientation on the constitutive material behaviour of differently oriented parts of the L-bracket is investigated.

A.2 Effect of build orientation on the material behaviour of printed parts

The material deposition strategy employed in fused filament fabrication (FFF) (Figure A.1) can be defined by the user during generation of the G-code in slicer software. Printed parts resemble laminate structures, and thus the material behaviour of the laminate depends on the constituents' properties and stacking sequence of the laminae. Similarly, the material behaviour of a printed part depends on fiber orientation in the layers, the stacking sequence of layers, and build orientation [124,138]. Laminate modeling can account for the effects of fiber orientation and stacking sequence of the layers in a 3D printed part. However, the effect of build orientation of the part on its material behaviour cannot be accounted for using laminate theory. The influence of build orientation on the material properties of 3D printed parts is therefore extensively discussed here.

A three-dimensional part can be oriented on different surfaces of the part on the substrate of the printer. For example, a rectangular plate of having thickness (*t*) can be oriented in three different ways as shown in Figure A.1. In the first case (Figure A.1a), surface A–B–C–D of the plate is lying on the substrate, which is commonly known as orienting the part on the flat surface. The other two options are the edge and upright orientations, where the plate is oriented on surface C–D–E–F and surface B–C–F–G, respectively (Figures A.1b and A.1c).

Experimental work has been done on the influence of build orientation on the mechanical properties of printed parts [69,70]. Although the number of layers deposited in each of the three orientations of the rectangular plate is different, the material deposition strategy is the same (Figure A.1). The layers of a 3D printed part exhibit lamina material behaviour owing to fiber orientation and layer-by-layer deposition. Previous experimental works have confirmed that the material behaviour of a printed part is also influenced by its build orientation.

Consequently, the behaviour of parts built in each of the three different orientations would also be different, since the deposition of layers is not the same. In the flat orientation case, the layers are deposited along the thickness of the plate, whereas in the edge and upright orientations, the layers are deposited along the width (*W*) and length (*L*), respectively, of the plate (Figure A.1). The mid-surface of the plate in the thickness direction is used in the laminate modeling of parts to characterize their behaviour using laminate plate theories. Laminate plate theory can be used to characterize the mechanical behaviour of a printed part when the layers are deposited only in the thickness direction. That means laminate theory can only capture the actual mechanical behaviour of the first case (flat orientation), since the layers are deposited in the thickness direction. The layers are not deposited in the direction of the mid-surface in the other two cases (edge and upright orientations) (Figures A.1b and A.1c). Therefore, the mechanical behaviour of these cases cannot be captured using laminate modeling.

Since the constitutive material behaviour of printed parts depends on build orientation, the actual constitutive material behaviour of parts built in different orientations must be determined to account for the final material behaviour in stress analysis. The material behaviour of parts built in the edge or upright position would be similar, since the layers are deposited across the thickness of the part in both cases. A detailed discussion on the effect of build orientation on the mechanical properties of printed parts is presented in the following sections. In particular, this work addresses the constitutive material modeling of printed parts with different build orientations and also characterization of the material behaviour of the printed parts during the stress analysis.

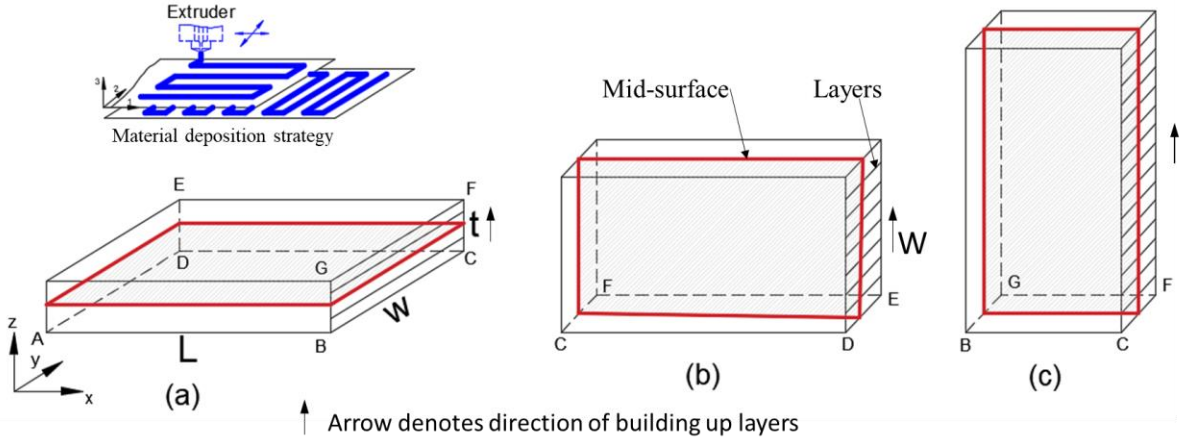

Figure A.1. Build orientation of a rectangular plate in three different directions: (a) flat, (b) edge, and (c) upright.

The 3D printed structures used in real applications will have more than one simple geometric shape. For that reason, let us consider an L-bracket structure for 3D printing via FFF, as shown in Figure A.2. The L-bracket consists of two different parts: a horizontal plate and a vertical plate. The horizontal plate lies in the *x*–*y* plane, and the vertical plate in the *y*–*z* plane. Let us consider the case where the L-bracket is printed on the substrate of the printer, as shown in Figure A.2a. As a result, the build orientation of the two different parts — the horizontal plate and the vertical plate — of the L-bracket is different, and therefore their material behaviour will be different.

To understand the reason for the difference in the material behaviour of the two parts, consider that the horizontal plate is built in a flat orientation and the vertical plate is built upright. However, it is the mid-surface of the bracket in the thickness direction of the plates that is used for laminate modeling in the finite element (FE) stress analysis of the structure. Laminate modeling can capture the constitutive material behaviour of the horizontal plate but not the vertical plate. As mentioned earlier, the behaviour of the vertical plate cannot be characterized using laminate modeling because the layers in the vertical plate are not deposited along the thickness of the final part. Instead, the layers are deposited across the thickness of the vertical plate. As a result, the layers in the vertical plate are not aligned with its mid-surface (Figure A.2b), and thus laminate modeling cannot capture the actual material behaviour of the vertical plate.

Since laminate modeling is not applicable in this case, another approach must be adopted to accurately model the material behaviour of the 3D-printed L-bracket. Experimental work [65,69,70,138] shows that printed parts built in the upright orientation exhibit orthotropic material behaviour. Therefore, the constitutive material behaviour of an orthotropic material can be used to characterize the mechanical behaviour of such cases. The constitutive matrix defines the constitutive material behaviour of printed parts, and therefore the constitutive matrix of printed parts built in different orientations can be computed based on their mesostructure using the homogenization technique described in chapter 6. The mesostructure of the horizontal and vertical plates of the L-bracket, as shown in Figure A.2b, is now considered for numerical homogenization of the material.

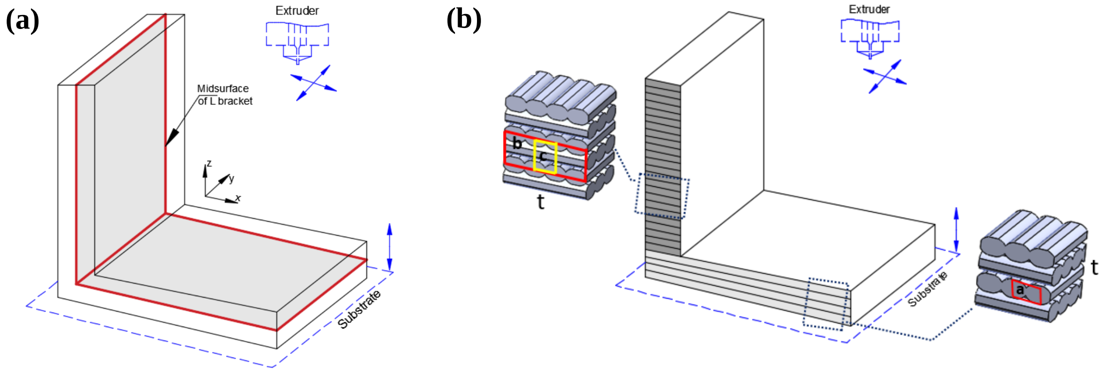

Figure A.2. L-bracket on the substrate of a 3D printer: (a) mid-surface; (b) layers and mesostructure of vertical and horizontal plates.

A.3 Constitutive material behaviour of printed parts

Let us consider the constitutive behaviour of the two plates of the 3D-printed L-bracket to account for their material behaviour in the FE stress analysis. The layers in the horizontal plate are thin and behave like an orthotropic material. Therefore, an orthotropic constitutive relation for the plane stress case is considered. In turn, the horizontal plate can be treated as a laminated plate, and therefore classical laminate theory can be employed to account for its material behaviour in the analysis of the plate, as explained in chapter 4.

The constitutive relation for an orthotropic material is given as

$$\begin{Bmatrix} \sigma_{11} \\ \sigma_{22} \\ \sigma_{33} \\ \tau_{23} \\ \tau_{13} \\ \tau_{12} \end{Bmatrix} = \begin{bmatrix} C_{11} & C_{12} & C_{13} & 0 & 0 & 0 \\ C_{12} & C_{22} & C_{23} & 0 & 0 & 0 \\ C_{13} & C_{23} & C_{33} & 0 & 0 & 0 \\ 0 & 0 & 0 & C_{44} & 0 & 0 \\ 0 & 0 & 0 & 0 & C_{55} & 0 \\ 0 & 0 & 0 & 0 & 0 & C_{66} \end{bmatrix} \begin{Bmatrix} \varepsilon_{11} \\ \varepsilon_{22} \\ \varepsilon_{33} \\ \gamma_{23} \\ \gamma_{13} \\ \gamma_{12} \end{Bmatrix}, \text{ in matrix form } \{\sigma\} = [\boldsymbol{C}]\{\varepsilon\} \qquad \text{(A.1)}$$

where C_{ij} are the elements of the constitutive matrix ***C*** with Voigt notation. The strain–stress relation for an orthotropic material is obtained by inverting eq. A.1 as follows:

$$\{\varepsilon\} = [\boldsymbol{S}]\{\sigma\} \qquad \text{(A.2)}$$

where ***S*** is the compliance matrix and the coefficients of the matrix are

$$S_{11} = \frac{1}{E_1}, S_{12} = -\frac{\nu_{12}}{E_2}, S_{13} = -\frac{\nu_{13}}{E_1}, S_{22} = \frac{1}{E_2}, S_{23} = -\frac{\nu_{23}}{E_2}, S_{33} = \frac{1}{E_3}, S_{44} = \frac{1}{G_{23}}, S_{55} = \frac{1}{G_{13}}, S_{66} = \frac{1}{G_{12}} \text{ (A.3)}$$

The coordinate system *1*, *2*, and *3* is a lamina (local) coordinate system; axis *1* is along the fiber, axis *2* is transverse to the fiber, and axis *3* is normal to the *1–2* plane, i.e. the axis goes along the thickness of the layer. The coefficients C_{ij} of the ***C*** matrix for an orthotropic material are obtained by inverting the ***S*** matrix. The elastic constants required to describe an orthotropic material are as follows: Young's moduli, E_1, E_2, E_3, for a layer along axes *1*, *2*, and *3*, respectively; shear moduli G_{12}, G_{13}, G_{23}; and Poisson's ratios $\nu_{12}, \nu_{13}, \nu_{23}$. Also, the relation $E_i \nu_{ji} = E_j \nu_{ij}$ (no sum on *i* and *j*) for *i*,*j*=1,2,3 and $i \neq j$ holds for orthotropic materials. For a transversely isotropic material, the elastic moduli in the lateral and transverse directions are the same.

Each layer is a thin plate, and therefore the layer is considered as a plane stress problem in the analysis. The strain–stress relation for a lamina under a plane stress case is obtained from eq. A.2 by setting $\sigma_{33} = 0,\ \tau_{23} = 0, \tau_{13} = 0$, which is written as

$$\begin{Bmatrix} \varepsilon_{11} \\ \varepsilon_{22} \\ \gamma_{12} \end{Bmatrix} = \begin{bmatrix} S_{11} & S_{12} & 0 \\ S_{12} & S_{22} & 0 \\ 0 & 0 & S_{66} \end{bmatrix} \begin{Bmatrix} \sigma_{11} \\ \sigma_{22} \\ \tau_{12} \end{Bmatrix} \tag{A.4}$$

The coefficients of compliance matrix ***S*** are available in eq. A.3. The plane stress reduced constitutive relation for an orthotropic material is obtained by inverting eq. A.4. The constitutive relation of a thin orthotropic layer is given as

$$\begin{Bmatrix} \sigma_{11} \\ \sigma_{22} \\ \tau_{12} \end{Bmatrix} = \begin{bmatrix} Q_{11} & Q_{12} & 0 \\ Q_{12} & Q_{22} & 0 \\ 0 & 0 & Q_{66} \end{bmatrix} \begin{Bmatrix} \varepsilon_{11} \\ \varepsilon_{22} \\ \gamma_{12} \end{Bmatrix} \tag{A.5}$$

where Q_{ij} are the coefficients of the plane stress reduced stiffness matrix ***Q*** , given by

$$\begin{aligned} Q_{11} &= \frac{S_{22}}{S_{11}S_{22} - S_{12}^2} = \frac{E_1}{1-\nu_{12}\nu_{21}},\ Q_{12} = \frac{S_{12}}{S_{11}S_{22} - S_{12}^2} = \frac{\nu_{12}E_1}{1-\nu_{12}\nu_{21}} \\ Q_{22} &= \frac{S_{11}}{S_{11}S_{22} - S_{12}^2} = \frac{E_2}{1-\nu_{12}\nu_{21}},\ Q_{66} = \frac{1}{S_{66}} = G_{12} \end{aligned} \tag{A.6}$$

Note that the reduced stiffness matrix's components involve only four independent material constants, E_1, E_2, ν_{12}, and G_{12}. The global coordinate system (*x*, *y*, *z*) for a laminate plate and local coordinate system (*1*, *2*, *3*) for a lamina are now considered.

The strain in the laminate from classical laminate theory is written as

$$\begin{Bmatrix} \varepsilon_{xx} \\ \varepsilon_{yy} \\ \gamma_{xy} \end{Bmatrix} = \begin{Bmatrix} \varepsilon_{xx}^0 \\ \varepsilon_{yy}^0 \\ \gamma_{xy}^0 \end{Bmatrix} + z \begin{Bmatrix} k_{xx} \\ k_{yy} \\ k_{xy} \end{Bmatrix}, \qquad \{\varepsilon\} = \{\varepsilon^0\} + z\{k\} \tag{A.7}$$

where ε_{xx}^0 and ε_{yy}^0 are mid-plane strains in the laminate; γ_{xy}^0 is the mid-plane shear strain in the laminate; k_{xx} and k_{yy} are bending curvatures in the laminate; k_{xy} is the twisting curvature in the laminate; and *z* is the distance from the mid-plane in the thickness direction.

The constitutive relation for a laminate is written as

$$\{\sigma\} = \left[\overline{\boldsymbol{Q}}\right]\{\varepsilon\} \tag{A.8}$$

where $\overline{Q}_{ij}$ are the transformed material constants. The elements of $\overline{Q}_{ij}$ are then given as

$$\left[\overline{\boldsymbol{Q}}\right] = [T]^{-1}[\boldsymbol{Q}][T]^{-T} \tag{A.9}$$

where $[\boldsymbol{T}]$ is a transformation matrix [130]. Equation A.8 is the constitutive relation for the horizontal plate based on laminate modeling and is useful to account for constitutive material behaviour in the stress analysis.

Now consider the constitutive material behaviour of the vertical plate of the L-bracket, which is printed in the upright orientation. The build orientation of this plate is different from that of the horizontal plate, and therefore the material behaviour is not same as that of a horizontal plate. As discussed earlier, the layer deposition is not in the direction of the thickness. Therefore, the constitutive relation of the laminate (eq. A.8) cannot be applied to the vertical plate. Also, the plane-stress assumption for the constitutive relation doe not hold true for the vertical plate, as the thin layers are not aligned with the mid-surface of the plate. However, the printed plate in the upright orientation displays orthotropic material behaviour, and therefore an orthotropic constitutive relation (eq. A.1) can be used in the stress analysis. The stiffness values in the constitutive matrix of the orthotropic material are unknown and are therefore computed to account for the material behaviour in the stress analysis of the part. The numerical homogenization procedure can be used to compute the stiffness values of the constitutive matrix of the printed part. The following section covers the constitutive material modeling of the horizontal and vertical plates of the L-bracket using the homogenization technique.

A.3.1 Homogenization for printed parts

The representative volume elements (RVEs) of the horizontal and vertical plates (Figures A.3a and A.3b) are taken from the mesostructure of the plates (Figure A.2b). The RVE of the horizontal plate is taken from only a single layer of the plate (marked region “a” in Figure A.2b), and then the constitutive matrix of the layer can be computed using homogenization. The homogenization procedure presented in chapter 6 is adopted here to calculate the constitutive matrix. Then, the matrix is used in the constitutive relation of the laminate to characterize the material behaviour of the horizontal plate. As we know, laminate theory cannot be applied for the vertical plate, and therefore the RVE of the vertical plate cannot be taken from a single layer. The RVE of the vertical plate, marked region “b” in the mesostructure of the plate (Figure A.2b), represents the fibers of the three adjacent layers. Then, homogenization is employed to calculate the effective constitutive matrix of the printed vertical plate.

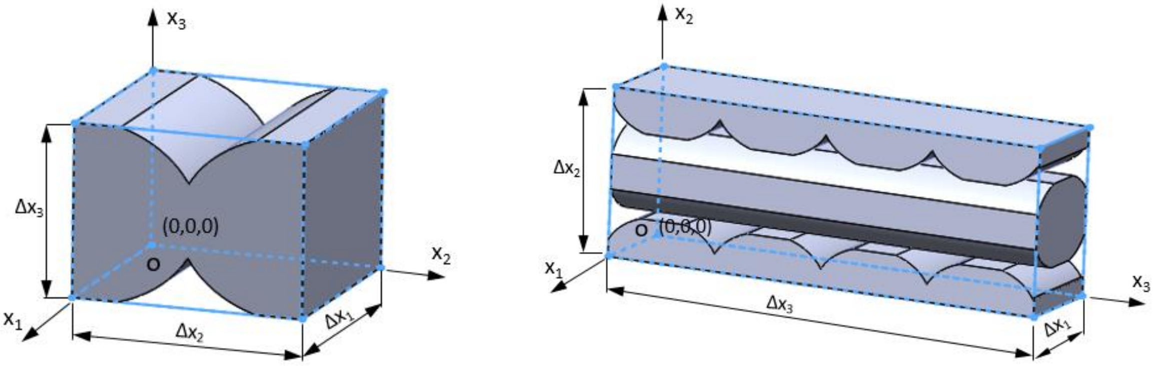

(a) **(b)**

Figure A.3. RVE of the printed plates in the L-bracket: (a) horizontal plate; (b) vertical plate.

A.4 Results and Discussion

This section presents the constitutive material modeling of the plates of the 3D-printed L-bracket. Let us take the L-bracket fabricated via FFF with the following process parameters: lines infill pattern; 100% infill density; raster angle 0° and 90° to the *x*-axis; layer thickness 0.317 mm; and 10% overlap between adjacent fibers. The raster angle represents the printing direction of fibers in the layers; in the present case, the fibers in subsequent layers are perpendicular to each other. These process parameters define the size and orientation of the fibers in the mesostructure of the printed part. Consider that the thickness of the plates of the L-bracket is 3.85 mm. The cross-sectional shape of the fiber after deposition of the material is elliptical [15,57]. The length of its major axis is approximately double the length of the minor axis, and the length of the minor axis is equal to the layer thickness. It is assumed in this analysis that bonding between the fibers and layers is perfect.

The filament material considered in the analysis is ABS. The isotropic material properties of ABS [129] are E = 2230 MPa and $\nu = 0.34$. The RVE is taken from the mesostructure of the plates, with its size and shape depending on the process parameters and build orientation of the plates. The RVE is defined in the local coordinate system x_1, x_2, and x_3, whose axes are aligned in the direction of the length, width, and thickness of the plates, respectively. The three-dimensional continuum eight-node hexahedron FEs, C3D8, are used in the FE modeling of the RVEs. FE modeling is done in Altair HyperMesh, and homogenization is then done using Abaqus (Dassault Systemes). The RVE is subjected to six different strains, applied individually using periodic boundary conditions. That means six different load cases are prepared for six unique strains to determine the unknown elements in the constitutive matrix ***C***. The strains applied to the RVE in the present analysis are $\bar{\varepsilon}_{11}, \bar{\varepsilon}_{22}, \bar{\varepsilon}_{33} = 0.01$ and $\bar{\varepsilon}_{12}, \bar{\varepsilon}_{13}, \bar{\varepsilon}_{23} = 0.005$.

Now, consider homogenization of the horizontal plate of the 3D printed structure. The dimensions of the RVE are Δx_1= 0.20 mm, Δx_2= 0.48 mm, and Δx_3= 0.31 mm. The FE model is shown in Figure A.4. The FE simulation for homogenization of the material was then carried out, and the unknown elements of the orthotropic constitutive matrix were calculated. The elements of the constitutive matrix are presented in Table A.1.

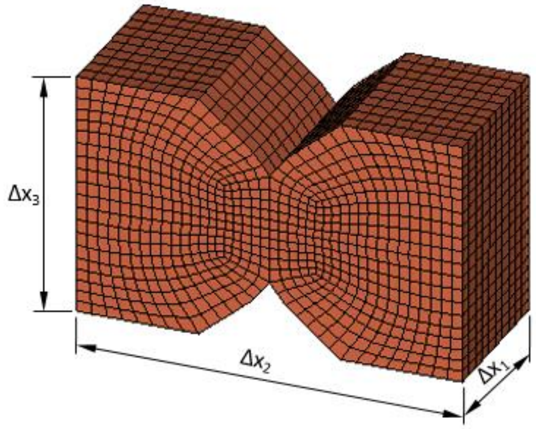

Figure A.4. FE model of an RVE from the horizontal plate of an L-bracket.

Table A.1. Constitutive matrix (C_{ijkl}, in MPa) for the material of the 3D-printed horizontal plate of an L-bracket.

C	11	22	33	23	13	12
11	2802.7	1136.6	1150.2	0.0	0.0	0.0
22	1136.6	2299.4	1043.5	0.0	0.0	0.0
33	1150.2	1043.5	2339.6	0.0	0.0	0.0
23	0.0	0.0	0.0	637.8	0.0	0.0
13	0.0	0.0	0.0	0.0	678.0	0.0
12	0.0	0.0	0.0	0.0	0.0	674.3

The elastic moduli of an orthotropic material can be calculated from the constitutive matrix using eq. A.3. The elastic moduli for the 3D-printed horizontal plate are provided in Table A.2. The stress contours in the RVE for six different deformation modes are similar to the earlier case outlined in the previous chapter. The interface between the adjacent fibers of a layer is the weakest region and is subjected to maximum stress. The interface is therefore more prone to the initiation of cracks in all six deformation modes.

Table A.2. Elastic moduli (E_i and G_{ij} in MPa) for the material of the 3D-printed horizontal plate of an L-bracket.

Material property	Value
E_1	2025.1
E_2	1660.2
E_3	1686.4
G_{12}	674.3
G_{13}	678.0
G_{23}	637.8
ν_{12}	0.34
ν_{13}	0.34
ν_{23}	0.30

The material behaviour of the horizontal plate is characterized using the constitutive relation of the laminate, eq. A.8. It accounts for the effect of printing direction and layer thickness for the constitutive material behaviour of a printed part. The thickness of the horizontal plate is 3.85 mm, and the layers in that plate are 0.317 mm thick. Therefore, the plate would consist of 12 layers of equal thickness. The stacking sequence of the layers with a defined raster angle in the horizontal plate is therefore $[0°/90°]_6$. The horizontal plate behaves like a laminate, and therefore the constitutive relation for a laminate can be used to characterize the mechanical behaviour of the plate using classical laminate theory, as described in chapter 4.

Next, let us consider numerical homogenization for the constitutive material modeling of the 3D-printed vertical plate of the L-bracket. The build orientation of this plate is upright, while the horizontal plate is flat. As explained earlier, build orientation influences the mechanical properties of printed parts. Consider that the thickness of this plate is the same as that of horizontal plate, 3.85 mm. The RVE of the plate is taken from the mesostructure of the vertical plate (Figure A.5). This figure shows different lengths of dimension Δx_3 of the RVE from the mesostructure of the vertical plate.

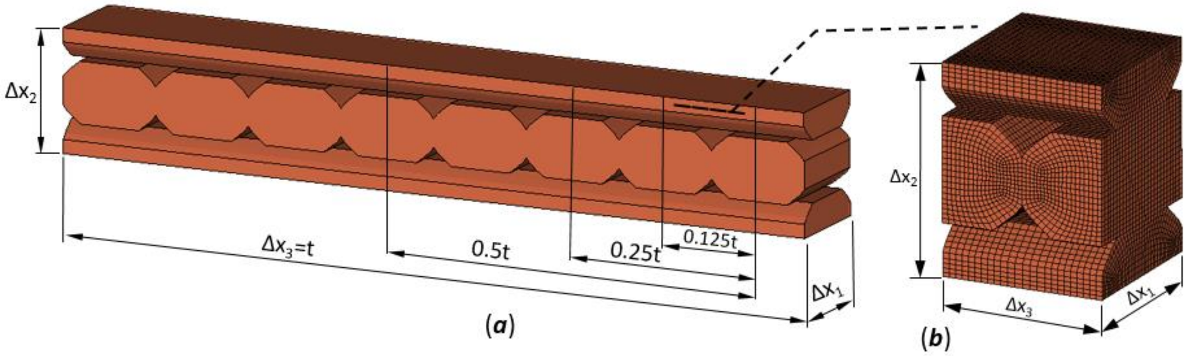

Figure A.5. RVE of the vertical plate of an L-bracket: (a) Δx_3 equals the thickness, *t*, of the plate; (b) Δx_3 equals 0.125*t*.

Let us consider the RVE shown in Figure A.5b. This RVE consists of the fibers of three adjacent layers, which are oriented perpendicular to each other. Its architecture is different from the RVE of the horizontal plate, which represents only a single layer. Since the layers of the plate do not act as laminae, laminate theory could not be employed for this plate, as explained earlier. The RVE represents the direction of the fibers in the subsequent layers and their thickness. Further, it accounts for the effect of build orientation of the layers of the plate. The dimensions of the RVE are $\Delta x_1 = 0.48$ mm, $\Delta x_2 = 0.62$ mm, and $\Delta x_3 = 0.48$ mm. The FE model of the RVE (Figure A.5b) was simulated for six different load cases. Then the unknown elements of the orthotropic constitutive matrix were calculated, with the results presented in Table A.3.

Table A.3. Constitutive matrix (C_{ijkl}, in MPa) of the 3D-printed vertical plate of an L-bracket (for an RVE with dimension $\Delta x_3 = 0.125t$).

C	11	22	33	23	13	12
11	2290.3	684.6	627.8	0.0	0.0	0.0
22	684.6	1589.7	508.1	0.0	0.0	0.0
33	627.8	508.1	1456.1	0.0	0.0	0.0
23	0.0	0.0	0.0	491.1	0.0	0.0
13	0.0	0.0	0.0	0.0	538.0	0.0
12	0.0	0.0	0.0	0.0	0.0	561.6

The stress contours and the deformation modes of the RVE subjected to six unique strains are shown in Figure A.6. In all deformation modes, the maximum stress is at the interface of the fibers. The deformation mode of the case where $\bar{\varepsilon}_{22} \neq 0$ is more prone to a crack initiating at the interface of the fibers, because this is the case with the highest stress. The RVE of the horizontal plate is taken from a single layer, and therefore the dimension Δx_3 of the RVE is equal to the thickness of the layer. However, for the RVE of the vertical plate, the dimension Δx_3 in the thickness direction affects the constitutive matrix of the plate, and its influence is investigated in the following work. Different sizes of RVE, such as $\Delta x_3 = 0.25t$, $0.50t$, and t, as seen in Figure A.6a, were taken from the vertical plate for the investigation. Then, FE models of the RVE were simulated for different load cases. The computed constitutive matrix for these different load cases is presented in Tables A.4, A.5, and A.6. Furthermore, to study its influence on thicker plates, simulations were also performed for the case where $\Delta x_3 = 2t$, which yielded the same results as the previous case ($\Delta x_3 = t$).

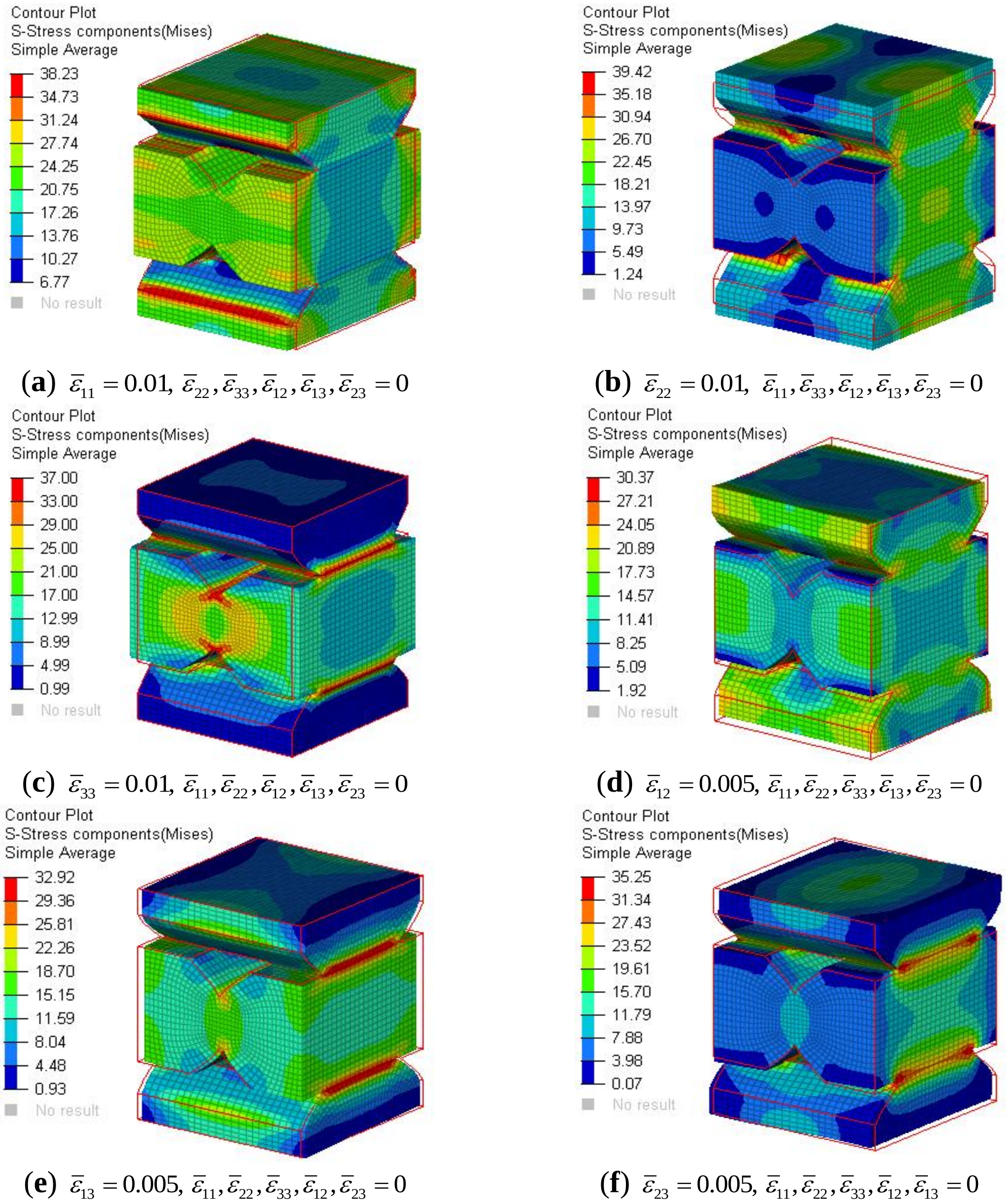

(a) $\bar{\varepsilon}_{11} = 0.01,\ \bar{\varepsilon}_{22}, \bar{\varepsilon}_{33}, \bar{\varepsilon}_{12}, \bar{\varepsilon}_{13}, \bar{\varepsilon}_{23} = 0$

(b) $\bar{\varepsilon}_{22} = 0.01,\ \bar{\varepsilon}_{11}, \bar{\varepsilon}_{33}, \bar{\varepsilon}_{12}, \bar{\varepsilon}_{13}, \bar{\varepsilon}_{23} = 0$

(c) $\bar{\varepsilon}_{33} = 0.01,\ \bar{\varepsilon}_{11}, \bar{\varepsilon}_{22}, \bar{\varepsilon}_{12}, \bar{\varepsilon}_{13}, \bar{\varepsilon}_{23} = 0$

(d) $\bar{\varepsilon}_{12} = 0.005,\ \bar{\varepsilon}_{11}, \bar{\varepsilon}_{22}, \bar{\varepsilon}_{33}, \bar{\varepsilon}_{13}, \bar{\varepsilon}_{23} = 0$

(e) $\bar{\varepsilon}_{13} = 0.005,\ \bar{\varepsilon}_{11}, \bar{\varepsilon}_{22}, \bar{\varepsilon}_{33}, \bar{\varepsilon}_{12}, \bar{\varepsilon}_{23} = 0$

(f) $\bar{\varepsilon}_{23} = 0.005,\ \bar{\varepsilon}_{11}, \bar{\varepsilon}_{22}, \bar{\varepsilon}_{33}, \bar{\varepsilon}_{12}, \bar{\varepsilon}_{13} = 0$

Figure A.6. Stress contours in the RVE with dimension $\Delta x_3 = 0.125t$ of the vertical plate of an L-bracket subjected to different strains.

Table A.4. Constitutive matrix (C_{ijkl}, in MPa) of the vertical plate of an L-bracket (for an RVE with dimension $\Delta x_3 = 0.25t$).

C	11	22	33	23	13	12
11	2337.2	717.9	742.6	0.0	0.0	0.0
22	717.9	1617.9	593.5	0.0	0.0	0.0
33	742.6	593.5	1745.2	0.0	0.0	0.0
23	0.0	0.0	0.0	526.0	0.0	0.0
13	0.0	0.0	0.0	0.0	600.8	0.0
12	0.0	0.0	0.0	0.0	0.0	562.7

Table A.5. Constitutive matrix (C_{ijkl}, in MPa) of the vertical plate of an L-bracket (for an RVE with dimension $\Delta x_3 = 0.5t$).

C	11	22	33	23	13	12
11	2383.5	751.0	857.4	0.0	0.0	0.0
22	751.0	1643.8	677.5	0.0	0.0	0.0
33	857.4	677.5	2033.3	0.0	0.0	0.0
23	0.0	0.0	0.0	544.2	0.0	0.0
13	0.0	0.0	0.0	0.0	640.8	0.0
12	0.0	0.0	0.0	0.0	0.0	563.3

Table A.6. Constitutive matrix (C_{ijkl}, in MPa) of the vertical plate of an L-bracket (for an RVE with dimension $\Delta x_3 = 1.0t$ and $2t$).

C	11	22	33	23	13	12
11	2450.3	799.0	1023.5	0.0	0.0	0.0
22	799.0	1680.6	798.9	0.0	0.0	0.0
33	1023.5	798.9	2450.3	0.0	0.0	0.0
23	0.0	0.0	0.0	563.7	0.0	0.0
13	0.0	0.0	0.0	0.0	686.7	0.0
12	0.0	0.0	0.0	0.0	0.0	563.8

The results presented in Tables A.4 through A.6 demonstrate that the values of C_{1133}, C_{2233}, C_{3333}, C_{1313}, C_{2323} in matrix ***C*** increase as dimension Δx_3 increases. It is clear that the stiffness values in direction 3 of the coordinate system for the RVE of the vertical plate are influenced by variation in Δx_3, until its value is equal to the thickness, t, of the plate. Further increase of Δx_3 above the thickness of the plate does not affect the constitutive matrix, as seen from the elements of matrix ***C*** in Table 6 that are the same for $\Delta x_3 = t$ and $2t$. The stress contours of the RVE with dimension $\Delta x_3 = t$ subjected to different strains are shown in Figure A.7.

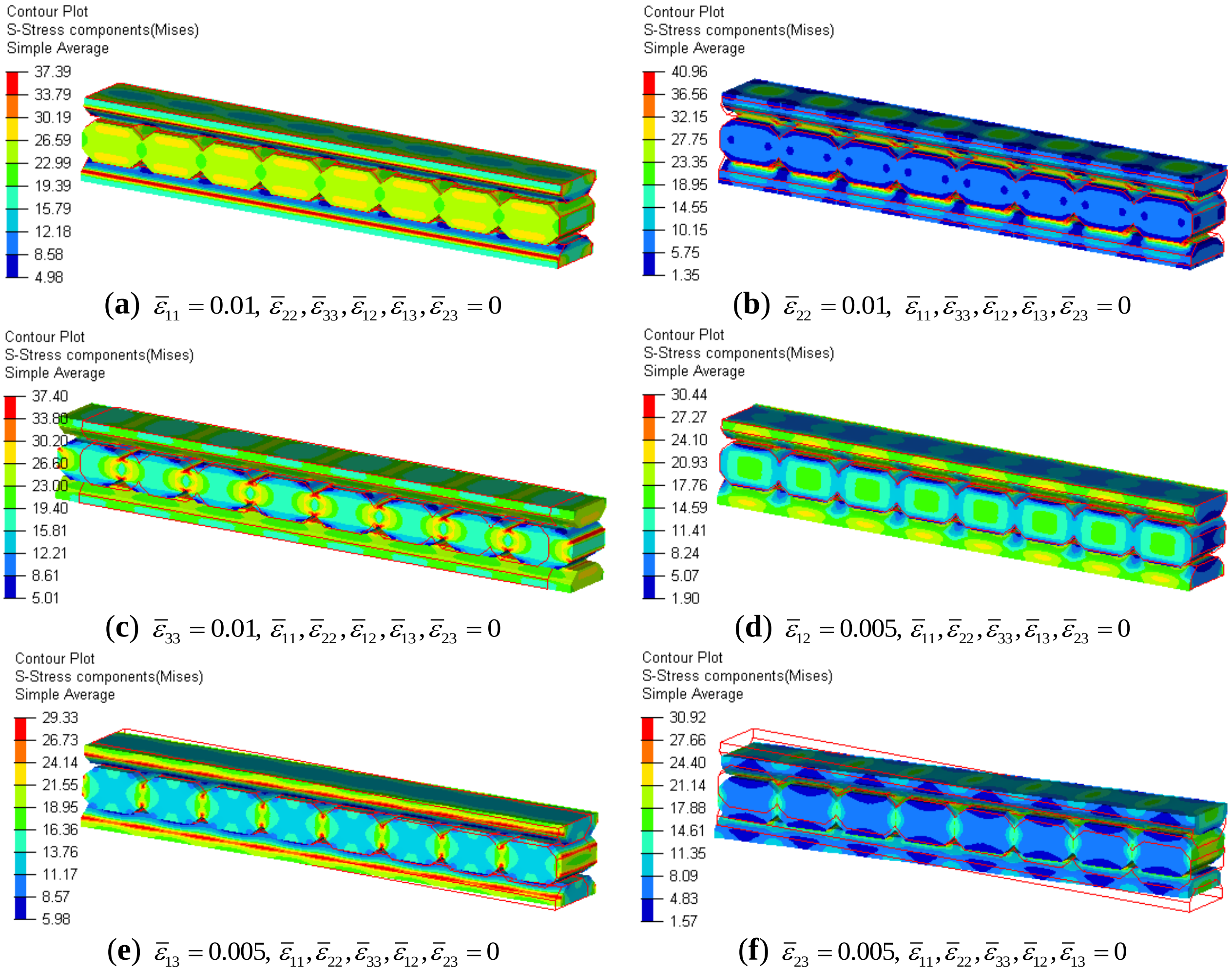

(a) $\bar{\varepsilon}_{11} = 0.01,\ \bar{\varepsilon}_{22}, \bar{\varepsilon}_{33}, \bar{\varepsilon}_{12}, \bar{\varepsilon}_{13}, \bar{\varepsilon}_{23} = 0$

(b) $\bar{\varepsilon}_{22} = 0.01,\ \bar{\varepsilon}_{11}, \bar{\varepsilon}_{33}, \bar{\varepsilon}_{12}, \bar{\varepsilon}_{13}, \bar{\varepsilon}_{23} = 0$

(c) $\bar{\varepsilon}_{33} = 0.01,\ \bar{\varepsilon}_{11}, \bar{\varepsilon}_{22}, \bar{\varepsilon}_{12}, \bar{\varepsilon}_{13}, \bar{\varepsilon}_{23} = 0$

(d) $\bar{\varepsilon}_{12} = 0.005,\ \bar{\varepsilon}_{11}, \bar{\varepsilon}_{22}, \bar{\varepsilon}_{33}, \bar{\varepsilon}_{13}, \bar{\varepsilon}_{23} = 0$

(e) $\bar{\varepsilon}_{13} = 0.005,\ \bar{\varepsilon}_{11}, \bar{\varepsilon}_{22}, \bar{\varepsilon}_{33}, \bar{\varepsilon}_{12}, \bar{\varepsilon}_{23} = 0$

(f) $\bar{\varepsilon}_{23} = 0.005,\ \bar{\varepsilon}_{11}, \bar{\varepsilon}_{22}, \bar{\varepsilon}_{33}, \bar{\varepsilon}_{12}, \bar{\varepsilon}_{13} = 0$

Figure A.7. Stress contours in the RVE with $\Delta x_3 = t$ of the vertical plate subjected to different strains.

The elastic moduli can be calculated using eq. A.3 for the orthotropic constitutive matrices presented in Tables A.4 through A.6. Figure A.8 shows variation in the elastic moduli of the material of the 3D printed vertical plate for an RVE with different dimensions of Δx_3. The values of the elastic moduli, namely E_3, G_{13}, G_{23}, ν_{13}, and ν_{23}, improved with an increase in Δx_3 until it equals the thickness of the plate. It is therefore clear that selecting the correct value for the dimension Δx_3 of an RVE for the homogenization of the material of a plate printed in an upright orientation is important for defining the constitutive matrix of the plate. Furthermore, the constitutive matrices of the horizontal and vertical plates, presented in Table A.1 and Table A.6, are not the same owing to their build orientation in the structure. The constitutive matrix computed for an RVE with dimension $\Delta x_3 = t$ and $2t$ is a transversely isotropic constitutive matrix, where two of E, G, and ν are the same. In all other cases, the constitutive matrix is orthotropic. That means the thickness of the plate printed in an upright orientation can change the constitutive behaviour of the plate, i.e. from orthotropic to transversely isotropic. The constitutive material behaviour of parts fabricated with an edge build orientation would be similar to that of parts fabricated with an upright build orientation, since the deposition of layers is across the thickness of the part in both cases.

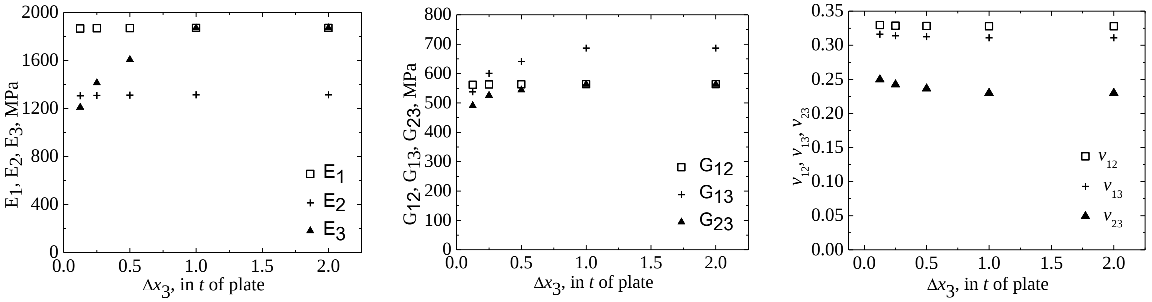

(a) **(b)** **(c)**

Figure A.8. Variation in the elastic moduli of the material of the vertical plate of an L-bracket for different values of Δx_3 for an RVE: (*a*) $E - \Delta x_3$, (*b*) $G - \Delta x_3$, and (*c*) $\nu - \Delta x_3$.

Now consider the FE modeling of the 3D-printed L-bracket for stress analysis. A two-dimensional FE mesh on the mid-surfaces of the plates of the L-bracket, as shown in Figure A.9, is useful for stress analysis. The constitutive matrix of the plates need to be considered to account for their material behaviour during the analysis. Then the selection of effective constitutive matrix of the plates necessitates based on their build orientation and thickness. Table A.7 presents the constitutive matrix of the plates of the L-bracket based on their build orientation and thickness.

Table A.7. Constitutive matrices for the plates of an L-bracket structure (laminate (L), orthotropic (O), or transversely isotropic (T) behaviour).

	Plate orientation					
	Horizontal	Vertical				
Build orientation	Flat	Upright	Upright	Upright	Upright	Upright
t (thickness, in mm)	4	0.5	1.0	2.0	4.0	8.0
Matrix ***C***	Table A1	Table A3	Table A4	Table A5	Table A6	Table A6
Behaviour	L	O	O	O	T	T

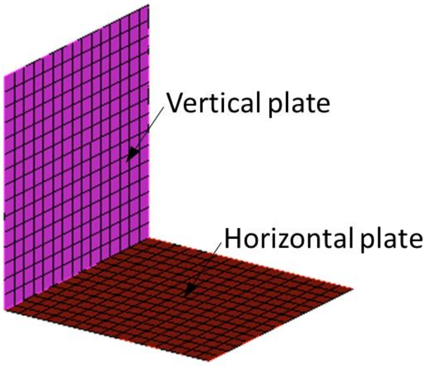

Figure A.9. FE model of an L-bracket structure for stress analysis.

Now let us see another possible build orientation of L-bracket on the substrate of the printer. For instance, the L-bracket is oriented on the substrate of the printer as shown in Figure A.10a. In this build orientation of the L-bracket, both plates of the bracket are positioned vertically, meaning that they are in an upright position for 3D printing. In this orientation, the plates of the bracket are built by depositing the layers in an upright position, as shown in Figure A.10. Then, the material behaviour of the plates would be similar to that of the vertical in the orientation of the L-bracket shown earlier. The FE model of this L-bracket for stress analysis, shown in Figure A.10b, uses the constitutive matrix provided in Table A.7 for an upright orientation. Therefore, the build orientation of a model on the substrate for 3D printing governs the constitutive behaviour of its parts.

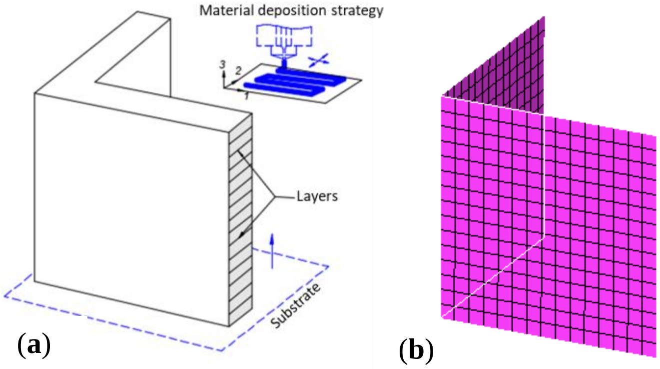

Figure A.10. L-bracket: (a) upright orientation of the bracket; (b) FE model of the bracket.

A.5 Conclusions

The constitutive material behaviour of the different parts of a 3D printed structure is not the same, as this behaviour depends on the build orientation of the parts. The material behaviour of the parts of a structure printed in the flat build orientation can be characterized using a laminate constitutive relation during the stress analysis of the structure. However, parts printed in an upright or edge build orientation cannot be characterized using laminate theory. The material behaviour of parts with an upright or edge build orientation is orthotropic, and therefore the constitutive relation for orthotropic material is employed to characterize their behaviour during the analysis of the structure.

Although an isotropic filament material is used to fabricate the structure, the final constitutive behaviour of the part is not the same as that of the original filament material. To address this problem, a computational procedure for calculating the constitutive matrix of the printed parts using numerical homogenization was presented. The constitutive matrix of differently oriented parts was computed.

Furthermore, the influence of build orientation of the parts on their constitutive material behaviour was investigated. The computed stiffness values of the constitutive matrix were different for the upright and flat build orientations of parts with the same thickness. The thickness of a part fabricated in either the upright or edge build orientation was also shown to influence its constitutive material behaviour. An increase in the thickness of a part printed in either the upright or edge build orientation was found to change their material behaviour from orthotropic to transversely isotropic. Therefore, to ensure effective design and analysis of a 3D printed structure, it is very important to consider the final constitutive material behaviour of the parts making up the structure when they are fabricated with different build orientations.